UCLouvain

epl

École polytechnique de Louvain

Dynamic Ray Tracing techniques for Mobile Radio Communications

Author: **Florian QUATRESOOZ**
Supervisor: **Prof. Claude OESTGES**
Readers: **Simon DEMEY, Prof. Jérôme LOUVEAUX**
Academic year 2019–2020
Master [120] in Electrical Engineering

Acknowledgements

The completion of this master thesis would not have been possible without the support and advice of several people.

First of all, I would like to express my sincere gratitude to my advisor, Prof. Claude Oestges, for his valuable recommendations, guidance and availability all along the academic year. I also thank him for giving me the opportunity to present and discuss some of my master thesis results at the 12th meeting of the COST action CA15104 (IRACON), held in Louvain-la-Neuve in January 2020.

Furthermore, I wish to acknowledge the help and assistance given by Mr. Simon Demey. His infinite support regarding the UCLouvain Ray Tracing software has been extremely valuable.

I am also particularly grateful to Mr. Chen Huang for giving me access to propagation measurements in a real environment as well as for helping me with the data processing.

In addition, I would like to thank Prof. Jérôme Louveaux for devoting time to read this document and to assess my work.

Last but not least, I would like to thank my family and my friends for their unceasing support and encouragements. I also wish to thank Guillaume Thiran and all the people that contributed to proofread this master thesis, that will recognize themselves in these lines.

Abstract

Ray tracing is a powerful tool to obtain deterministic characterizations of communication channels and can be applied to predict the evolution of channels with high level of mobility. However, performing ray tracing simulations at each discrete time instant is computationally expensive. In this master thesis, a new approach to extrapolate results obtained from a single ray tracing simulation is presented, performing a so-called “dynamic ray tracing”. It relies on the geometric tracking of interaction points (i.e. reflection or diffraction points), enabling analytical or numerical predictions of the evolution of any ray identified during an initial ray tracing simulation. The performance of this new approach is studied on several canonical vehicle-to-vehicle configurations, thanks to comparisons with classical ray tracing simulations as well as with measurements in a real environment. Focus is also given to the time horizon during which dynamic ray tracing is possible, related to the lifetime of the main rays. This time horizon can be directly estimated based on the knowledge of the geometry and its evolution. It is found to be the main parameter influencing the accuracy and the computational gain of the presented approach.

Le tracé de rayon est un outil efficace pour caractériser les canaux de communication de façon déterministe, pouvant être appliqué pour prédire l’évolution de scénarios souffrant d’une importante mobilité. Cependant, réaliser des simulations de tracé de rayon à chaque instant est coûteux en termes de temps de calcul. C’est pourquoi, dans ce mémoire, une nouvelle approche permettant d’extrapoler les résultats obtenus sur base d’une unique simulation de tracé de rayon est présentée, réalisant alors du “tracé de rayon dynamique”. Celle-ci est basée sur le suivi géométrique des points d’interaction (points de réflexion ou de diffraction), et permet de prédire, analytiquement ou numériquement, l’évolution des rayons identifiés lors d’une simulation de tracé de rayon initiale. Les performances de cette nouvelle approche sont étudiées sur plusieurs configurations faisant intervenir des communications véhiculaires, grâce à une comparaison non seulement avec du tracé de rayon classique mais aussi avec des mesures tirées d’un environnement réel. En outre, l’horizon de temps durant lequel le tracé de rayon dynamique est possible est étudié, et est lié au temps de vie des rayons principaux. Il peut être directement estimé sur base de la connaissance de la géométrie et de son évolution. Enfin, il est le paramètre principal influençant la précision et le gain en calcul de la présente approche.

Contents

List of abbreviations

BS	Base station
BSP	Binary space partitioning
CIR	Channel impulse response
DRT	Dynamic ray tracing
ER	Effective roughness
GO	Geometrical optics
GSCM	Geometry-based stochastic model
GTD	Geometrical theory of diffraction
ISB	Incident shadow boundary
ISI	Intersymbol interference
LOS	Line-of-sight
MPC	Multipath component
NLOS	Non-line-of-sight
RMS	Root mean square
RSB	Reflection shadow boundary
RT	Ray tracing
RX	Receiver
SINR	Signal-to-interference-plus-noise-ratio
STD	Standard deviation
TX	Transmitter
UTD	Uniform theory of diffraction
V2V	Vehicle-to-vehicle

Chapter 1

Introduction

The modeling of mobile radio communication channels has been an important research topic for decades. Several types of channel models have been developed, such as empirical, stochastic or deterministic models, in order to tackle the ever increasing challenges faced by new generations of wireless communication systems.

Currently, deterministic models of communication channels, such as Ray Tracing (RT), are gaining interest and are expected to assist the design of future millimeter wave wireless systems. Indeed, working at higher frequencies makes the ray optics assumption (which is at the hearth of any RT model) more valid, improving the accuracy of the obtained results. Moreover, the computation time is also reduced since high frequency waves suffer from a larger attenuation with the distance. Therefore, less multipath contributions are observed and fewer rays need to be computed (by limiting the maximum number of interactions[1] allowed in the RT software for example) [1]. Current trends in RT research focus on these two main topics [2]: the level of details required to accurately model an environment is being studied (such as modeling trees, scattering [3], etc.), and new software approaches to reduce the computation time are being developed [4].

However, future communication channels will also become more dynamic, with fast motion (e.g. for Vehicle-to-Vehicle (V2V) communications [5]). Real-time beamforming or channel estimation may then be more challenging, advocating for new solutions. For example, one possible approach would be to directly embed RT simulations inside wireless communication systems [1,2]. This requires RT models to be more dynamic, i.e. to provide simulation outputs during a given time interval and not only at a given instant, with stronger timing constraints. Therefore, in the present work, a possible approach to perform Dynamic Ray Tracing (DRT) is investigated.

Chapter 2 explores deeper the available channel modeling tools, highlighting the motivations for RT models as well as the main research trends in the field. It also presents the current state of the art of DRT and a detailed definition of this approach.

Then, Chapter 3 details the physical and mathematical background behind any RT models. Based on the geometry of a given environment, a RT software outputs the geometric rays linking a transmitter (TX) and a receiver (RX). From these rays, using the equations gathered

---

[1] In this work, reflection or diffraction are the considered interactions.

in Chapter 3, the values of the received electric fields can be determined.

The newly-developed DRT approach is presented in Chapter 4. The goal of this approach is to avoid performing new RT simulations at each discrete time instant, while still being able to estimate the communication channel (i.e. the rays) at these instants. This approach relies on the tracking of interaction points that have been identified during a first and single RT simulation, as well as on a perfect knowledge of the environment and its time evolution. Chapter 4 ends with a geometric validation of the new DRT approach.

Since the purpose of this work is also to assess the performance of the developed DRT method, some channel metrics are presented in Chapter 5, before being applied to several canonical configurations in Chapter 6. They enable to compare the DRT results at the channel level and to discuss some limitations of the approach, namely the chosen extrapolation time. This latter corresponds to the time during which DRT conclusions are "sufficiently close" to the ones obtained by RT.

Finally, a statistical study conducted on typical urban configurations is presented in Chapter 7. According to several practical rules, this study helps to tune the extrapolation time. It involves the comparison of RT and DRT results using the previously defined channel metrics. In this last chapter, a comparison with measurements in a real environment is also explored.

All in all, the overall structure of this work is given in Figure 1.1. Based on the knowledge of the geometry and an initial RT simulation, the DRT approach is used to obtain channel characteristics at several instants in a given time interval. Then, in order to be validated, the results are compared with RT simulations performed at those same instants but at the price of a greater computational cost.

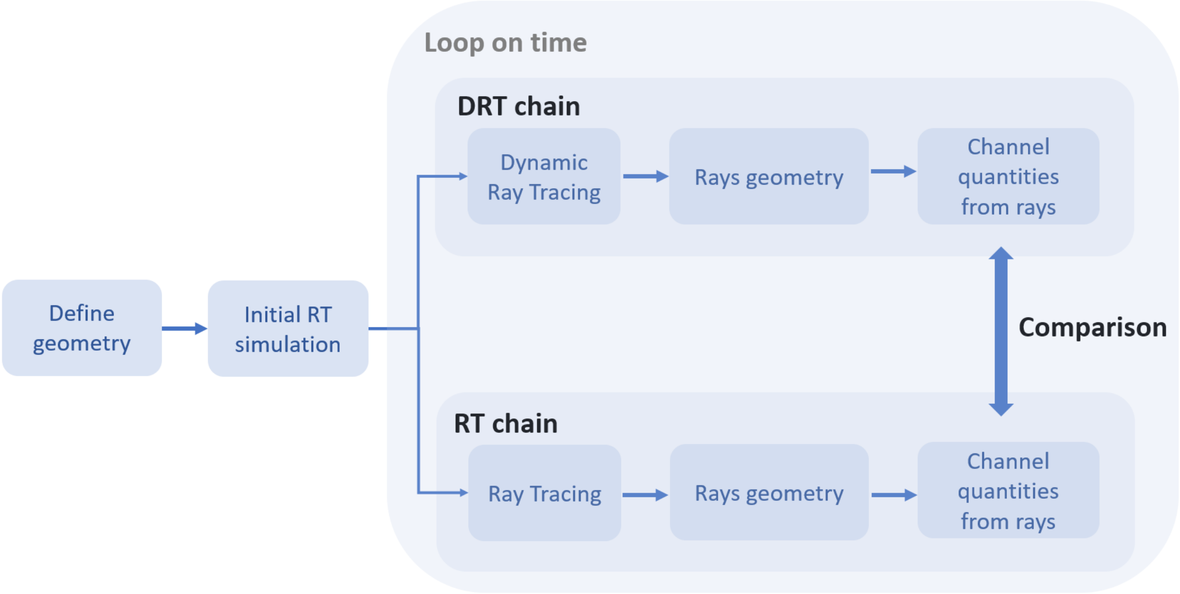

Figure 1.1: Structure of RT and DRT comparison

Chapter 2

Background and state of the art

In order to understand the framework of this master thesis, knowledge about the background of ray tracing and the state of the art of dynamic ray tracing is gathered in this chapter.

First of all, RT is briefly described and compared to other tools used for channel modeling. After that, the main research trends in RT are explored, before taking a look at DRT and what has been previously done in this field. Further works extrapolating results from a single RT simulation are then considered. Finally, some conclusions about the RT approach and its limitations are drawn.

2.1 Ray tracing as a tool for channel modeling

2.1.1 Brief description of ray tracing

Historically, RT has first been studied and developed for computer graphics applications [6]. At that time, RT was only used to model the propagation of optical rays in order to generate more realistic synthetic images. This initial focus on optics has been built based on the ray optics approximation, in the framework of geometrical optics (GO). In this framework, the frequency of electromagnetic waves is assumed to tend to infinity. This leads to the derivation of the concept of light ray (see Section 3.1 for the mathematical derivation of the ray concept in GO). In short, a *ray* is nothing but a line showing the direction of wave propagation, that is perpendicular to the wavefronts. It can be reflected, transmitted, and, with some extensions to GO, diffracted. Then, in the 1990s, RT has started to be applied to radio frequencies to predict radio wave propagation in a given environment [7,8]. Thirty years later, it has become an essential tool for the modeling and the design of wireless communication systems.

Ray tracing, in the sense of radio wave propagation, could be defined as follows: it is a computer approach enabling to obtain deterministic models of wave propagation in a given environment, based on solving Maxwell's equations using the GO assumption (often extended with the uniform theory of diffraction (UTD), see Section 3.3) and its associated concept of rays. In other words, provided a geometrical description of the environment, a RT software is able to identify all rays linking a transmitter and a receiver and to compute the received electric fields. It can therefore provide a complete multidimensional characterization of a radio channel (in the time, space or polarization domains), giving accurate path loss estimation, angles of departure/arrival, delay profiles,... [1,2]. An example of geometrical output of a RT

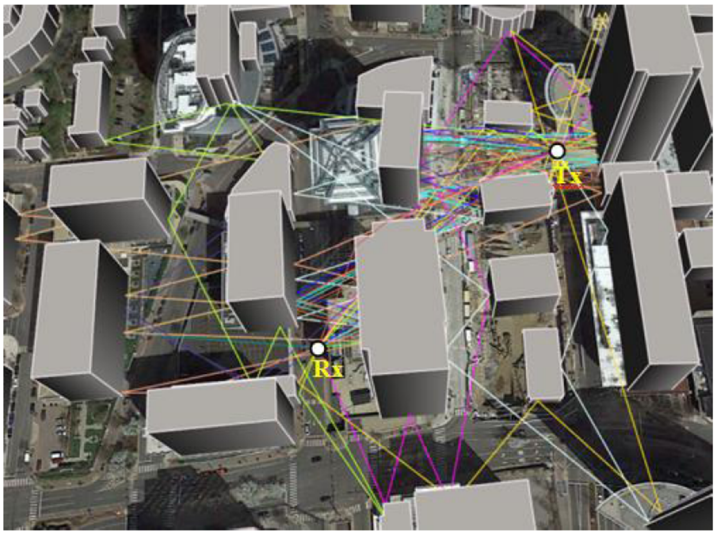

Figure 2.1: Example of ray tracing in an urban environment (Source: [2])

software is given in Figure 2.1, where the environment geometry and some rays linking the transmitter and the receiver are highlighted.

2.1.2 Comparison with other tools

Since RT is a tool that can be used for channel modeling, a comparison with other tools achieving the same goal is relevant to emphasize its characteristics, advantages and limitations.

Empirical models The first identified category of channel models gathers all models based on empirical data, i.e. measurements. A well-known example of such models is the Okumura-Hata empirical model [9, 10]. This model gives empirical expressions for the path loss, such as

$$L_{dB} = A + B\log\left(d_{km}\right) - C, \tag{2.1}$$

where L_{dB} is the path loss (in dB) and d_{km} is the distance between the base station (BS) and the receiver, in kilometers. The coefficients A, B and C have been obtained thanks to measurements. They depend on the carrier frequency, the antenna heights and the considered environment (either urban, suburban or open area).

These models are very simple to use but they do not provide any insight about the physical mechanisms behind the propagation. Moreover, the classification of the environments is quite subjective and the models can only be used in environments similar to the ones where the measurements were made, and over the same range of parameters [2].

Stochastic models Stochastic models (or statistical models) are very useful to handle time dependency of channels and to obtain important statistics. Such models include, for example:

- The Rayleigh fading model, describing the fading occurring due to multipath propagation and varying coherent or non-coherent additions of signals from different paths. This fading is usually added to the shadowing (attenuation due to large scale obstacles, assumed to follow a log-normal distribution) and the path loss to obtain the total attenuation of the channel.

- Geometry-based stochastic models (GSCM), such as WINNER II [11] or COST 2100 [12], that rely on the geometric distribution of scatterers in the environment to model the stochastic properties of the channels.

Naturally, stochastic models also rely on measurement campaigns to obtain the statistics that need to be modeled. Therefore, they can be seen as empirical models integrating stochastic principles [13].

Deterministic models Compared to the previous models, deterministic models take into account all the elements of the environment (at least all the elements that have been modeled) and they study the wireless propagation in this particular environment. Methods solving Maxwell's equations in this geometry, such as ray tracing, belongs to this category [5]. They can generally achieve a high accuracy but have a high computational complexity.

The comparison of those different channel modeling approaches is given in Table 2.1. It emphasizes the low complexity but inaccurate results of empirical approaches as well as the trade-off among all criteria achieved by stochastic models. The main drawback of the RT approach is its computational complexity. Moreover, one can already notice that RT in itself is not perfectly suited for characterizing dynamic environments (i.e. to obtain time-dependent characteristics), which motivates the dynamic approach developed in this work.

Type of models	Empirical	Stochastic	Deterministic
Accuracy	Poor, except in the environment where the measurements have been made	Fair	Good, depends on the modeled phenomena and the accuracy of the environment models
Complexity	Low, provide fast and simple results	Low (e.g. Rayleigh fading) to medium (e.g. GSCM)	High, computationally expensive, need new computations for new environments
Physical insight	None	Few insights (e.g. multipaths)	A lot, can identify the main rays and impacts of the environment
Time dependency	None	Give statistical distributions	Indirect, can be achieved by performing several simulations at different times
Environment dependency	Subjective categories (e.g. urban, suburban, open area)	Some in GSCM, by modeling scatterers	High, solve Maxwell's equations in a given environment
Support for MIMO	No [2]	Yes (e.g. COST 2100)	Yes [1]

Table 2.1: Comparison of channel modeling tools

2.1.3 Some application cases

Ray tracing can be applied to model any communication channel, provided that the environment geometry has been reproduced digitally. Examples of applications span from the design and planning of wireless systems (e.g. by computing the power received in a given location to determine where to put the BS's) to multidimensional channel characterization. RT can be used to model indoor or outdoor propagation, to assist indoor localization techniques, to provide real-time channel estimations by embedding RT tools in wireless communication systems, etc. [1, 2]

Even though RT is designed as a channel modeling tool, it can be applied to obtain results at the network level such as the cumulative distribution of the signal-to-interference-plus-noise-ratio (SINR) perceived by the users [14, 15]. It can then be relevant to compare results obtained by RT with the ones coming from other tools giving network descriptions, such as stochastic geometry [16].

Finally, RT is also particularly suited for millimeter wave propagation since the targeted frequencies are higher than the ones of radio waves. Hence, the ray assumption is more valid and results are more accurate. However, the impact of small scatterers in the environment may become more important and therefore a higher level of details for the environment model may be needed. Nevertheless, many recent works use RT to characterize and get some insights about millimeter wave propagation [17–20].

2.2 Main research trends in ray tracing

As already hinted in the previous section, RT is actually a trade-off between the level of detail required to accurately model an environment and the computation time. Indeed, adding more details to improve the accuracy of the models also makes them more complex and more computationally intensive. Current research trends in the field of RT focus on those two goals and are briefly explored in this section. However, the information given here is far from being exhaustive.

2.2.1 Accuracy and level of detail

Urban cluttering A typical urban area is not made of rectangular buildings but contains street cluttering such as vehicles, groups of humans, trees, street signs, lamp posts, etc. [21] They impact the propagation of waves and are therefore the focus of current researches.

One possible approach is to directly model these obstacles and add them in the environment, increasing the complexity of the model. For example, trees have been modeled [14, 22, 23], attenuation due to human bodies has been studied [15, 24, 25], traffic signs have been added in the geometry [26], etc.

Another approach is to model structures irregularities (such as balconies or windows) using diffuse scattering.

Diffuse scattering Diffuse scattering, related to dense multipath components (dense MPCs), corresponds to the part of the channel that cannot be modeled by coherent components (such as the line-of-sight (LOS) or specular reflections) [27]. It is related to walls' roughness and surface irregularities and can be modeled using an effective roughness (ER) approach. This approach uses scattering coefficients added to the RT model that allow to describe the scattering pattern centered on the direction of specular reflection [1, 28].

Sensitivity to environment modeling The geometric accuracy of propagation environment models can have an important impact on the prediction accuracy. Several tools are available to automatically build digital databases of an environment [2], but they have a limited accuracy. An example is OpenStreetMap [29], where one can expect an accuracy in the meter range [30].

Old studies found that an error of one meter on building positions does not drastically impact the predicted path loss [31, 32], whereas recent studies emphasize that the accuracy required for the positioning of the BS's must be below the meter or tens of centimeters [21]. Therefore, further works in this direction are needed.

2.2.2 Computational complexity

Efficient RT techniques can have many flavours and the purpose of this work is not to enter into these details. A review of such techniques can be found in [4]. Nevertheless, since UCLouvain ray tracing software [27, 33] uses a *visibility tree* to improve the computational speed, a few words about this approach are given here as an example of how efficient algorithms are used to speed up RT.

Visibility tree As stated in [1], a *visibility tree* arranges all the objects in a database using their visibility relationships. Such a tree is built recursively: the first layer contains all the objects that can be seen directly from the transmitter, while the n-th layer contains the objects that can be seen from the ones belonging to the $(n-1)$-th layer. Usually, it is represented by a Binary Space Partitioning (BSP) tree, see [33], where all technical details about UCLouvain RT software are given.

2.3 Study of dynamic environments

Table 2.1 shows that time dependency can be studied with RT provided that simulations are performed at every instant (suggesting implicitly that the dynamic evolution of the environment is known). However, such an approach is computationally expensive. Instead, hybrid, or semi-deterministic, models have been developed: RT is used to obtain specular components and then the results are extended with other models (e.g. stochastic models) to represent the time variation of the channel or the dense MPCs [24, 34–36].

Nevertheless, this is not the only option. Fully deterministic and dynamic RT models are starting to gain interest and are considered in this work. Motivations behind deterministic approaches are multiple. On the one hand, developing fast RT methods enables to obtain more easily channel quantities in the Doppler domain (which is relevant for dynamic channels);

since they require to perform several static simulations in a time series and then to take the Fourier transform [37]. On the other hand, deterministic DRT allows to get more physical insight of high dynamic channels, enabling for example to obtain statistical quantities thanks to simulations [26]. Based on these, stochastic models could be derived.

This section gathers the basis of deterministic DRT that can be found in the literature.

2.3.1 Shadowing due to vehicles

Several studies have emphasized the shadowing effect due to (moving) vehicles in V2V and millimeter wave communications, highlighting the need for adding these obstacles in the environment description.

Indeed, measurements have shown that, on average, the shadowing due to a single vehicle can go from 10 to 20 dB, especially if the vehicle is disrupting the LOS [38, 39]. This has also been observed in RT simulations [26]. Moreover, RT simulations, with fixed obstacles and conducted at the network level, showed that the effect of vehicular obstruction can be mitigated thanks to dynamic switching of BS [14, 15, 24]. Indeed, even if a vehicle is blocking the LOS to the closest BS, it can also create new reflection and diffraction paths enabling to reach another BS. Furthermore, interference can be reduced by blocking interfering links to other BS's, improving the received SINR.

Again, this important dynamic variability of the environment and its impacts are motivations for dynamic ray tracing.

2.3.2 Doppler shift of frequency

It is well-known that the motion of a transmitter or a receiver induces a shift of frequency, i.e. a Doppler shift, whose expression[2] is, following [40, 41],

$$f_{RX} \approx f_{TX} \left(\frac{c - \boldsymbol{v}_{RX} \cdot \hat{\boldsymbol{k}}}{c - \boldsymbol{v}_{TX} \cdot \hat{\boldsymbol{k}}} \right), \tag{2.2}$$

with f_{TX} the frequency of the source, f_{RX} the one received (i.e. observed) and c the velocity of light in vacuum. The velocity vectors of the transmitter and the receiver are denoted $\boldsymbol{v}_{TX}$ and $\boldsymbol{v}_{RX}$, while $\hat{\boldsymbol{k}}$ is a unit vector along the direction of propagation between TX and RX.

First DRT software artificially added this frequency shift in the results of the RT simulations [5]. For example, the change of frequency on a LOS ray for a moving receiver (with velocity $\boldsymbol{v}$), as depicted in Figure 2.2, is given by

$$f_{RX} = f_{TX} \left(\frac{c - \boldsymbol{v} \cdot \hat{\boldsymbol{k}}}{c} \right) = f_{TX} + \frac{f_{TX}}{c} v \cos(\Psi) = f_{TX} + f_d, \tag{2.3}$$

---

[2] The expression given in equation (2.2) comes from the Doppler effect in classical mechanics, used here as an approximation for the relativistic Doppler effect applying to electromagnetic waves. This latter is given by $f_{RX} = f_{TX} \sqrt{\frac{1 - \frac{v}{c}}{1 + \frac{v}{c}}}$ in the longitudinal case, with v the relative velocity between the transmitter and the receiver ($v > 0$ if they are moving away from each other). Decoupling $\boldsymbol{v}_{RX}$ and $\boldsymbol{v}_{TX}$ as in (2.2) is therefore an approximation, valid for small transmitter and receiver velocities w.r.t. the speed of light. Luckily this is commonly the case for V2V communications.

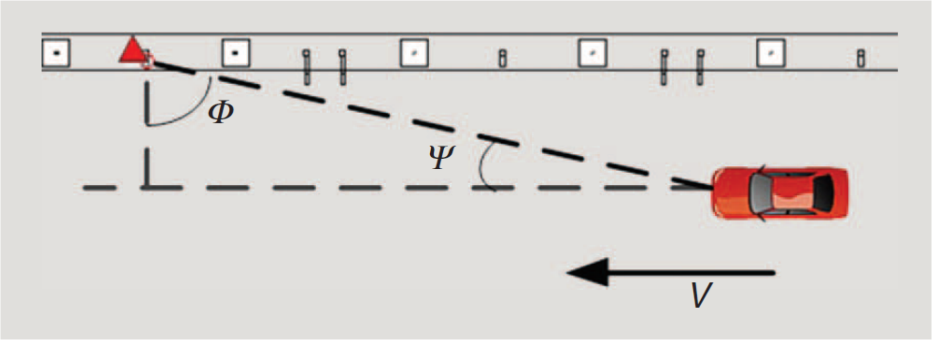

Figure 2.2: Doppler shift for a moving receiver (Source: [5])

where f_d is the Doppler shift and is equal to $f_d = \frac{v}{\lambda}\cos(\Psi)$ as stated in [5], since $c = \lambda f_{TX}$ with λ the wavelength.

Extension to non-LOS (NLOS) rays with multiple interactions is possible thanks to an iterative method [40, 41]. Indeed, the received frequency is

$$f_{RX} \approx f_{TX} \prod_{i=1}^{n+1} \left(\frac{c - \boldsymbol{v}_i \cdot \hat{\boldsymbol{k}}_i}{c - \boldsymbol{v}_{i-1} \cdot \hat{\boldsymbol{k}}_i} \right), \tag{2.4}$$

with n the number of interactions and the index i denoting the i-th interaction. One has $\boldsymbol{v}_0 = \boldsymbol{v}_{TX}$ and $\boldsymbol{v}_{n+1} = \boldsymbol{v}_{RX}$, other $\boldsymbol{v}_i$'s corresponding to the velocities of the objects on which there is an interaction point (reflection or diffraction point). Finally, $\hat{\boldsymbol{k}}_i$ is the direction of propagation for the i-th interaction.

In [40], applying this approach to millimeter wave mobile scenarios where the receiver is moving and the BS is fixed has shown that the Doppler power spectrum obtained is far from the "bathtub" spectrum of the Jakes' model [42]. This is nothing but another motivation for DRT, since classical stochastic or statistical models (such as the Jakes' model) fail to obtain relevant results at millimeter waves.

However, equation (2.4) is actually not accurate. In fact, the velocities $\boldsymbol{v}_i$'s are not the velocities of the objects on which there is an interaction but rather the velocities of the interaction points themselves. Indeed, interaction points also slide on the surface and have therefore their own velocity, and this phenomenon is often disregarded [41].

2.3.3 Sliding of interaction points

The sliding of interaction points (i.e. reflection or diffraction points) has been presented in [41]. Figure 2.3 details the approach followed to compute the velocity $\boldsymbol{v}_Q$ of the reflection point, and also highlights why the sliding occurs, especially in short-range scenarios with large obstacles. $\boldsymbol{P}_T$ (resp. $\boldsymbol{P}_R$) is the TX (resp. RX) position at time t_0, while $\boldsymbol{P}'_T$ (resp. $\boldsymbol{P}'_R$) is the position at time $t_0 + \partial t$. The rays are obtained using image theory and the law of reflection, which are reviewed in Section 3.2.

To compute $\boldsymbol{v}_Q$, it is easier to work in the reference frame linked to the reflecting wall. The relative velocities of the TX and the RX w.r.t. the wall must therefore be used. Since the

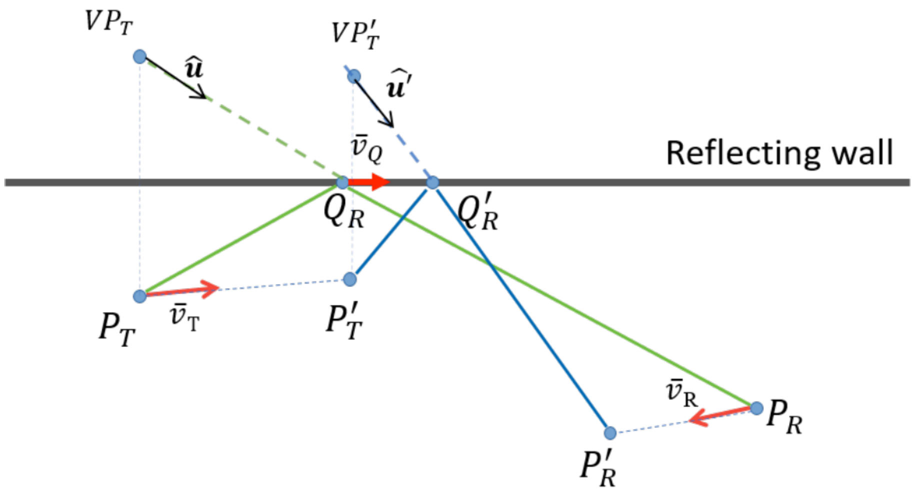

Figure 2.3: Illustration of sliding of reflection point - $\overline{\boldsymbol{v}}_T$ *corresponds to* $\boldsymbol{v}_{TX}$*,* $\overline{\boldsymbol{v}}_R$ *to* $\boldsymbol{v}_{RX}$ *and* $\overline{\boldsymbol{v}}_Q$ *to* $\boldsymbol{v}_Q$ (Source: [41])

dynamic evolution of the geometry is known, the positions of the transmitter or receiver can be computed at any instant, and especially at $t_0 + \partial t$. Then, it is possible to compute the position of the reflection point at time $t_0 + \partial t$ (i.e. at the intersection between the reflection wall and the line going through the TX image point $\boldsymbol{VP}'_T$ and the receiver in $\boldsymbol{P}'_R$) and compare it to the one obtained thanks to a RT simulation at time t_0 to get the velocity $\boldsymbol{v}_Q$. Based on this velocity, Doppler shifts can be obtained (using equation (2.4) but this time with $\boldsymbol{v}_i$ being the velocity of the i-th reflection point itself) as well as the new positions of the reflection points at any instant, thanks to $\boldsymbol{Q}_R(t) = \boldsymbol{Q}_R(t_0) + (t - t_0)\boldsymbol{v}_Q$. Further details as well as analytical equations for this approach are not presented in [41] but are part of this work, in Chapter 4.

Actually, [41] lays the foundations of fast, deterministic, accurate and dynamic ray tracing: based on a single RT simulation at time t_0, knowledge of the channel (such as Doppler shifts) can be obtained at any instant belonging to the interval $[t_0, t_0 + T_c]$, with T_c denoting the lifetime of the main MPCs of the channel. Indeed, it is expected that some rays may appear or disappear, impacting the predictions made during the extrapolation time. This effect has also been further studied in this work.

2.4 Extrapolation from a single simulation

The idea of extrapolating results from a single RT simulation to get fast and accurate deterministic knowledge of a communication channel is not new and not especially related to DRT. Indeed, it has already been suggested in order to compute the electric field in the vicinity of the receiver, i.e. to perform a kind of spatial extrapolation [43, 44].

The obtained mathematical expressions depend on the type of ray considered (LOS, one reflection, multiple reflections, diffraction,...) but involve the same principles. Starting from the electric field value received in RX_1, the one obtained in position RX_2 suffers from:

- An attenuation coefficient related to the distance between TX and the second receiver (and not TX-RX$_1$ anymore) and impacting the module of the field;

- A phase shift coming from the extra distance traveled, between RX$_1$ and RX$_2$.

Mathematical expressions are given in [44] and are related to the GO expressions of the electric field, presented in Section 3.1.

This method has a low complexity and provides good extrapolation results in a small area around the receiver as long as the contributions are coming from the same rays (no new ray). It also relies on some assumptions, namely the fact that reflection coefficients are kept constant even though the angles of incidence of the rays will be different for the receivers RX$_1$ and RX$_2$. No assumption is made regarding the diffraction coefficients since they are recomputed. Indeed, considering these to be constant can lead to large phase errors for the fields [44].

2.5 Summary of the RT approach and its limitations

In a nutshell, ray tracing is a channel modeling tool enabling to obtain deterministic representations of wave propagation in a given environment. It relies on solving Maxwell's equations with the GO assumption, and obtaining RT equations will be the purpose of Chapter 3. Moreover, at the heart of any RT software, there is a trade-off between the desired level of accuracy and the computation time. The main limitations of the RT approach are:

- GO approximation: Maxwell's equations are solved assuming that the frequency of the considered electromagnetic waves tends to infinity. Equivalently, the wavelength is assumed to tend to zero. Since it is not the case in practice, results obtained are approximations. However, going from radio waves towards millimeter or optical waves makes these approximations more valid since the considered frequency is increasing.
- Computation time: this is the Achilles' heel of RT. Obtaining deterministic representations requires a large amount of computation time since, for each environment, a new simulation must be performed.
- Accuracy of the environment model: if the digital map of the environment is not accurate enough, prediction results will be impacted. Furthermore, the higher the targeted frequencies, the higher the level of details needed. This explains why this is a hot topic, especially now that RT is applied to millimeter waves. Indeed, even if the GO approximation is more valid for such waves, results will be more accurate only if a more detailed representation of the environment is used.
- Dynamic environment: in order to obtain descriptions of dynamic environments (for which the dynamic evolution is known), RT simulations must be performed at each instant, increasing drastically the computation time. Another approach is to use hybrid semi-deterministic RT models, giving stochastic descriptions of dynamic environments.

In this work, the dynamic limitation of RT is tackled using deterministic DRT. Since this dynamic approach is designed to be as deterministic and accurate as possible, the sliding of reflection points needs to be taken into account and is actually paramount in the approach followed and presented in Chapter 4.

Chapter 3

Ray tracing theory and implementation

The purpose of this chapter is to gather all the physical equations related to the concept of rays and that are widely used in RT software. A brief summary of these can be found in [2].

This chapter is structured as follows: starting from Maxwell's equations, the ray concept is derived. Then, the main propagation mechanisms (reflection, refraction and diffraction) are explored, before discussing briefly their software implementations. Finally, all the characteristics of rays are summarized.

3.1 From Maxwell's equations to geometrical optics

As stated in [45], GO is based on an approximate high-frequency method in order to determine wave propagation fields (mainly incident, reflected and refracted fields, as GO fails to describe diffraction). It uses the concept of rays and can directly be derived from Maxwell's equations. Indeed, Maxwell's equations in free space for time-harmonic fields are [46]

$$\begin{aligned}
\nabla \times \boldsymbol{E}(\boldsymbol{r},\omega) + j\omega\mu\, \boldsymbol{H}(\boldsymbol{r},\omega) &= 0, \qquad (3.1)\\
\nabla \times \boldsymbol{H}(\boldsymbol{r},\omega) - j\omega\epsilon\, \boldsymbol{E}(\boldsymbol{r},\omega) &= 0, \qquad (3.2)\\
\nabla \cdot \boldsymbol{E}(\boldsymbol{r},\omega) &= 0, \qquad (3.3)\\
\nabla \cdot \boldsymbol{H}(\boldsymbol{r},\omega) &= 0, \qquad (3.4)
\end{aligned}$$

where $\boldsymbol{E}(\boldsymbol{r},\omega)$ and $\boldsymbol{H}(\boldsymbol{r},\omega)$ are the electric and magnetic field vectors (phasor quantities, since the harmonic time variation is dropped). The vector $\boldsymbol{r}$ is the position vector, and ω is the pulsation. The permittivity of the medium is denoted ϵ and μ is the permeability. Both are assumed to be constant since they do not appear in the zero-divergence equations (i.e. media are considered homogeneous, or can be divided in homogeneous subregions). Moreover, non-magnetic media are usually considered and $\mu = \mu_0 = 4\pi \times 10^{-7} \left[\frac{kg\, m}{A^2 s^2}\right]$ is the permeability of vacuum.

Eliminating the magnetic field $\boldsymbol{H}(\boldsymbol{r},\omega)$ from equations (3.1) and (3.2), one can obtain the Helmholtz equation:

$$\nabla^2 \boldsymbol{E}(\boldsymbol{r},\omega) \; + \; k^2 \boldsymbol{E}(\boldsymbol{r},\omega) \; = \; 0, \qquad (3.5)$$

with $k = \omega\sqrt{\mu_0\epsilon}$ the wavenumber [27]. A similar equation can be found for $\boldsymbol{H}$.

The *Luneburg-Kline ansatz* (i.e. anticipated solution), or *high-frequency expansion*, is a series expansion providing a bridge between GO and wave propagation [45]. In the case of a source-free region, with constitutive parameters ϵ and μ_0 [46]:

$$\boldsymbol{E}(\boldsymbol{r},\omega) \;\sim\; \mathrm{e}^{-jk\Psi(\boldsymbol{r})} \sum_{m=0}^{+\infty} \frac{\boldsymbol{E}_m(\boldsymbol{r})}{(j\omega)^m}, \tag{3.6}$$

$$\boldsymbol{H}(\boldsymbol{r},\omega) \;\sim\; \mathrm{e}^{-jk\Psi(\boldsymbol{r})} \sum_{m=0}^{+\infty} \frac{\boldsymbol{H}_m(\boldsymbol{r})}{(j\omega)^m}. \tag{3.7}$$

Equations (3.6) and (3.7) lead to several comments:

- $\Psi(\boldsymbol{r})$ is the phase function, denoting eikonal surfaces, i.e. surfaces having the same phase, also called wavefronts;
- $\boldsymbol{E}_m$ and $\boldsymbol{H}_m$ are amplitude vectors (for some physical interpretations, see [47]);
- The symbol $\sim$ denotes the equality in an asymptotic sense, i.e. when ω (thus the frequency) approaches infinity or, equivalently, when the wavelength λ tends to zero.

In the case where ω tends to infinity, only the first term remains, leading to the so-called GO fields, i.e. *rays* [27]:

$$\lim_{\omega\to+\infty} \boldsymbol{E}(\boldsymbol{r},\omega) \;=\; \boldsymbol{E_0}(\boldsymbol{r})\,\mathrm{e}^{-jk\Psi(\boldsymbol{r})}. \tag{3.8}$$

Substituting the Luneberg-Kline equations (3.6-3.7) in the Helmholtz equation (3.5), as well as using zero-divergence Maxwell's equations (3.3-3.4), one can obtain:

1) The eikonal equation [46]:

$$\|\nabla\Psi(\boldsymbol{r})\|^2 \;=\; 1. \tag{3.9}$$

This equation is often written with the phase function $S(\boldsymbol{r})$, such that $S(\boldsymbol{r}) = \sqrt{\epsilon_r}\Psi(\boldsymbol{r})$. This corresponds to have $k_0 = \omega\sqrt{\mu_0\epsilon_0}$ in the Luneberg-Kline equations, instead of $k = \omega\sqrt{\mu_0\epsilon}$, such that [45]

$$\|\nabla S(\boldsymbol{r})\|^2 \;=\; n^2(\boldsymbol{r}), \tag{3.10}$$

with $n = \sqrt{\epsilon_r}$ the refractive index of the media (ϵ_r is the relative permittivity of the medium, such that $\epsilon = \epsilon_r\epsilon_0$, with $\epsilon_0 = 8.854 \times 10^{-12}$ $[Fm^{-1}]$ the vacuum permittivity). This expression is also valid for non-homogeneous media, as long as the variation of $n(\boldsymbol{r})$ (equivalently, $\epsilon(\boldsymbol{r})$) is continuous. Denoting by s the distance along the path, the differential equation of rays (well-known in optics) can be derived from equation (3.10) [2]:

$$\frac{\mathrm{d}}{\mathrm{d}s}\left(n(\boldsymbol{r})\frac{\mathrm{d}\boldsymbol{r}}{\mathrm{d}s}\right) \;=\; \nabla n(\boldsymbol{r}). \tag{3.11}$$

In the case of a homogeneous medium, equation (3.11) reduces to $\frac{\mathrm{d}^2\boldsymbol{r}}{\mathrm{d}s^2} \;=\; 0$, for which the solution is a straight line ($\boldsymbol{r} \;=\; \boldsymbol{a}s + \boldsymbol{b}$ with $\boldsymbol{a}$ and $\boldsymbol{b}$ being constant vectors). Therefore, the ray trajectory is a straight line in homogeneous media.

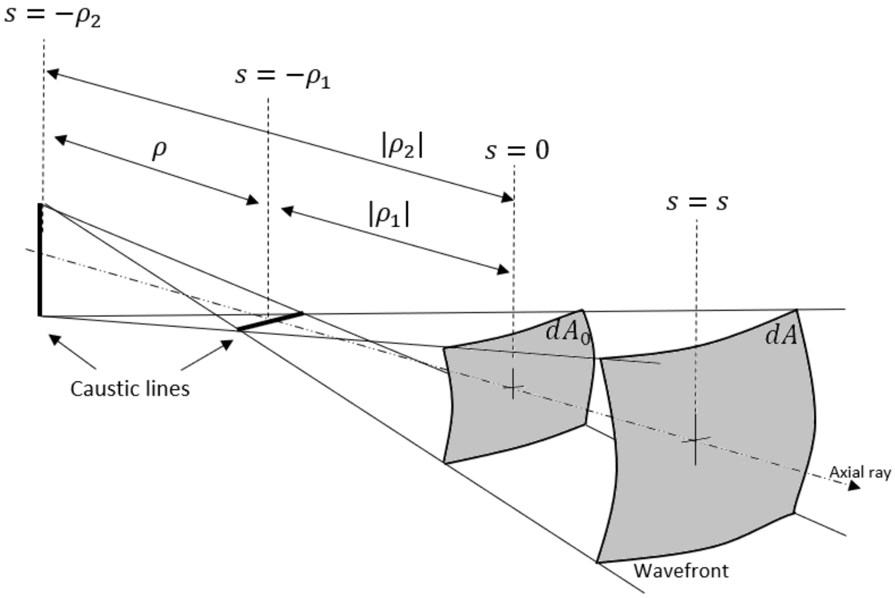

Figure 3.1: Astigmatic ray tube (reproduced from [46])

2) Locally plane wave property: $\boldsymbol{E_0}$, $\boldsymbol{H_0}$ and $\hat{\boldsymbol{s}} := \nabla\Psi(\boldsymbol{r})$ are mutually perpendicular at any point of a ray [46], meaning that

$$\boldsymbol{E_0} = \sqrt{\frac{\mu}{\epsilon}}\,(\boldsymbol{H_0} \times \hat{\boldsymbol{s}}) \tag{3.12}$$

is satisfied. Power flows in the direction of $\hat{\boldsymbol{s}}$ and there is no field components in this direction.

3) The transport equations. For the first-order term, with s the distance along the ray path [46]:

$$\frac{\partial \boldsymbol{E_0}}{\partial s} + \frac{1}{2}(\nabla^2\Psi(\boldsymbol{r}))\boldsymbol{E_0} = 0. \tag{3.13}$$

Integration of this equation gives the continuation of the amplitude of a ray, that can also be derived from the conservation of the electric field intensity. Indeed, for a general representation of rays (astigmatic tube, see Figure 3.1), electric field intensities are related by [45]

$$\frac{\|\boldsymbol{E}\|}{\|\boldsymbol{E_0}\|} = \sqrt{\frac{\mathrm{d}A_0}{\mathrm{d}A}} = \sqrt{\frac{\rho_1\rho_2}{(\rho_1+s)(\rho_2+s)}}, \tag{3.14}$$

with ρ_1 and ρ_2 the radii of curvature for the reference constant phase surface $\Psi(0)$ (i.e. the wavefront, associated with an area $\mathrm{d}A_0$), measured along the central ray. Caustic, or focal, lines are crossed by all the rays of a wave, and the distance $\rho = \rho_2 - \rho_1$ is the astigmatic difference (i.e. if this distance is zero, the ray is stigmatic and its focus is a point). The factor given by equation (3.14) is called the *spreading factor* (or divergence factor).

4) Phase continuation: in a homogeneous isotropic media, the phase along the ray path is [46]

$$\mathrm{e}^{-jk\Psi(s)} = \mathrm{e}^{-jk\Psi(0)}\,\mathrm{e}^{-jks}. \tag{3.15}$$

In summary, using all the previous results, one can give the expression of the GO field for an astigmatic tube, along the ray trajectory [45]:

$$\boldsymbol{E}(s) = \underbrace{\boldsymbol{E_0}(0)\,\mathrm{e}^{-j\Psi(0)}}_{\text{Field at reference point}} \underbrace{\sqrt{\frac{\rho_1\rho_2}{(\rho_1+s)(\rho_2+s)}}}_{Spreading factor} \underbrace{\mathrm{e}^{-jks}}_{Phase factor}. \tag{3.16}$$

This equation simplifies when describing particular cases such as plane, cylindrical and spherical waves.

Plane waves In this case, wavefronts are planar surfaces perpendicular to the direction of travel, with $\rho_1 \to \infty$ and $\rho_2 \to \infty$, such that equation (3.16) reduces to

$$\boldsymbol{E}(s) = \boldsymbol{E_0}(0)\,\mathrm{e}^{-j\Psi(0)}\mathrm{e}^{-jks}. \tag{3.17}$$

Cylindrical waves Wavefronts are cylindrical surfaces perpendicular to cylindrical radial vectors, with one of the radii of curvature being infinite ($\rho_1 \to \infty$, $\rho_2 = \rho$ for example):

$$\boldsymbol{E}(s) = \boldsymbol{E_0}(0)\,\mathrm{e}^{-j\Psi(0)}\sqrt{\frac{\rho}{\rho+s}}\,\mathrm{e}^{-jks}. \tag{3.18}$$

Spherical waves For a spherical wave, wavefronts are spherical surfaces perpendicular to radial vectors, and $\rho_1 = \rho_2 = \rho$, such that equation (3.16) is now

$$\boldsymbol{E}(s) = \boldsymbol{E_0}(0)\,\mathrm{e}^{-j\Psi(0)}\,\frac{\rho}{\rho+s}\,\mathrm{e}^{-jks}. \tag{3.19}$$

Equations (3.16) to (3.19) describe only LOS propagation. Interactions with the environment, such as reflection or transmission, result in modifications of such expressions and are considered in the next section.

3.2 Reflection and transmission coefficients

Geometrical optics is also able to describe phenomena occurring at an (infinite) interface between two media, i.e. reflections and refractions. Indeed, at an interface, part of the incident field is reflected in a particular direction (specular reflection, as opposed to diffuse reflection), whereas another component is transmitted (refracted) in the second medium. From Maxwell's equations, with the proper limit conditions for electric and magnetic fields at the interface, one can derive the law of reflection, Snell's law, as well as Fresnel coefficients. The considered geometry is depicted in Figure 3.2, where $\boldsymbol{E}_i$ is the incident electric field, $\boldsymbol{E}_r$ the reflected field and $\boldsymbol{E}_t$ the transmitted field. Ray-fixed coordinate systems are also depicted, highlighting the polarisation vectors parallel and perpendicular to the plane of incidence. One has $\hat{\boldsymbol{e}}_{i,\perp} = \hat{\boldsymbol{e}}_{r,\perp} = \hat{\boldsymbol{e}}_{t,\perp} = \hat{\boldsymbol{e}}_{\perp}$, all going out of the page.

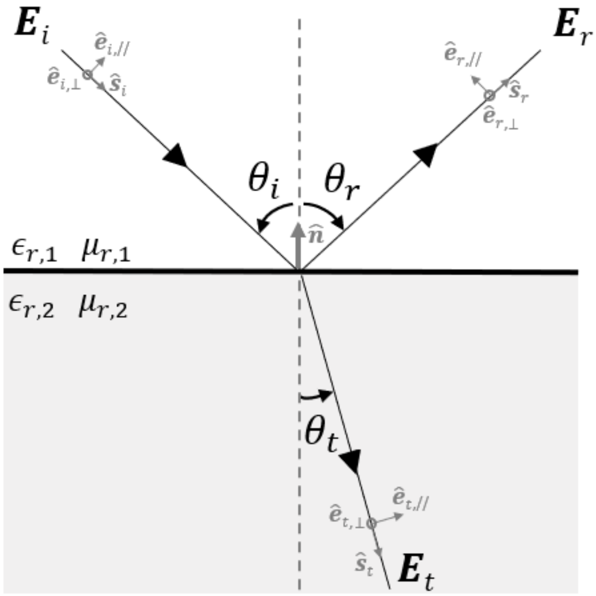

Figure 3.2: Incidence plane - incident, reflected and transmitted rays

Law of reflection Incident and reflected rays, as well as the normal to the interface, lie in the same plane, called *plane of incidence*. Incident and reflected angles, measured with respect to the normal, are equal (and lie on opposite sides of the normal):

$$\theta_i = \theta_r, \tag{3.20}$$

where θ_i is the incidence angle and θ_r the angle of the reflected ray.

Snell's law Again, incident, refracted rays and the normal to the interface lie in the plane of incidence. Angles are measured w.r.t. the normal and the angle of the refracted ray is related to the angle of the incident ray thanks to

$$k_1 \sin(\theta_i) = k_2 \sin(\theta_t), \tag{3.21}$$

with θ_t the angle of the refracted ray, $k_1 = \sqrt{\epsilon_{r,1}\mu_{r,1}}\,\omega\sqrt{\epsilon_0\mu_0}$ the wavenumber for the first medium and $k_2 = \sqrt{\epsilon_{r,2}\mu_{r,2}}\,\omega\sqrt{\epsilon_0\mu_0}$ the wavenumber for the second medium.

In the particular case of non-magnetic media (relative permeabilities $\mu_{r,1} = \mu_{r,2} = 1$ such that $\mu = \mu_0$), the well-known expression of Snell's law using the refractive indexes is found:

$$n_1 \sin(\theta_i) = n_2 \sin(\theta_t), \tag{3.22}$$

with $n_1 = \sqrt{\epsilon_{r,1}}$ the refractive index of the first medium and $n_2 = \sqrt{\epsilon_{r,2}}$ the refractive index of the second medium.

Fresnel coefficients The law of reflection and Snell's law describe the directions of all rays (geometrical aspects) but do not provide the amplitudes and polarisations of the reflected and refracted fields. These latter are given by Fresnel coefficients and depend on the polarisation of the incident fields (either parallel or perpendicular to the plane of incidence). In a general case, they are expressed with the wave impedance $Z = \sqrt{\frac{\mu}{\epsilon}} = \sqrt{\frac{\mu_r\,\mu_0}{\epsilon_r\,\epsilon_0}}$:

$$R_h = \frac{Z_1\cos(\theta_i) - Z_2\cos(\theta_t)}{Z_2\cos(\theta_t) + Z_1\cos(\theta_i)} \qquad T_h = \frac{2\,Z_2\cos(\theta_i)}{Z_2\cos(\theta_t) + Z_1\cos(\theta_i)} \tag{3.23}$$

$$R_s = \frac{Z_2\cos(\theta_i) - Z_1\cos(\theta_t)}{Z_2\cos(\theta_i) + Z_1\cos(\theta_t)} \qquad T_s = \frac{2\,Z_2\cos(\theta_i)}{Z_2\cos(\theta_i) + Z_1\cos(\theta_t)}, \tag{3.24}$$

where R_h and R_s (resp. T_h and T_s) are the reflection (resp. transmission) coefficients for the parallel and perpendicular polarisations. The conventions presented in Figure 3.2 are followed.

For non-magnetic media, they can be expressed using only the relative permittivities of the media (or equivalently the refractive indexes) instead of their impedances:

$$R_h = \frac{\frac{\epsilon_{r,2}}{\epsilon_{r,1}}\cos(\theta_i) - \sqrt{\frac{\epsilon_{r,2}}{\epsilon_{r,1}} - \sin^2(\theta_i)}}{\frac{\epsilon_{r,2}}{\epsilon_{r,1}}\cos(\theta_i) + \sqrt{\frac{\epsilon_{r,2}}{\epsilon_{r,1}} - \sin^2(\theta_i)}} \qquad T_h = \frac{2\sqrt{\frac{\epsilon_{r,2}}{\epsilon_{r,1}}}\cos(\theta_i)}{\frac{\epsilon_{r,2}}{\epsilon_{r,1}}\cos(\theta_i) + \sqrt{\frac{\epsilon_{r,2}}{\epsilon_{r,1}} - \sin^2(\theta_i)}} \tag{3.25}$$

$$R_s = \frac{\cos(\theta_i) - \sqrt{\frac{\epsilon_{r,2}}{\epsilon_{r,1}} - \sin^2(\theta_i)}}{\cos(\theta_i) + \sqrt{\frac{\epsilon_{r,2}}{\epsilon_{r,1}} - \sin^2(\theta_i)}} \qquad T_s = \frac{2\,\cos(\theta_i)}{\cos(\theta_i) + \sqrt{\frac{\epsilon_{r,2}}{\epsilon_{r,1}} - \sin^2(\theta_i)}}. \tag{3.26}$$

Usually, the first propagation medium is air, with a relative permittivity assumed to be comparable to the one of vacuum, i.e. $\epsilon_{r,1} = 1$. Regarding the second medium, the relative permittivity can be complex[3] with the imaginary part depicting the absorption losses and being frequency-dependent. Typical values can be found in [48].

Furthermore, the reflection coefficients can be gathered in a dyadic coefficient $\overline{\mathbf{R}} = R_h\hat{\boldsymbol{e}}_{i,\parallel}\hat{\boldsymbol{e}}_{r,\parallel} + R_s\hat{\boldsymbol{e}}_\perp\hat{\boldsymbol{e}}_\perp$, expressed in the frame parallel/perpendicular to the plane of incidence [48], whose matrix representation is

$$\left[\overline{\mathbf{R}}\right] = \begin{bmatrix} R_h & 0 \\ 0 & R_s \end{bmatrix}. \tag{3.27}$$

Finally, the reflected field at a distance s' from the point of reflection (denoted Q_r) can be written as [45]

$$\boldsymbol{E}_r(s') = \underbrace{\boldsymbol{E}_i(Q_r)}_{\text{Field reference}} \cdot \underbrace{\overline{\mathbf{R}}}_{\text{Reflection coefficients}} \underbrace{\sqrt{\frac{\rho_1^r\rho_2^r}{(\rho_1^r + s')(\rho_2^r + s')}}}_{\text{Spreading factor}} \underbrace{\mathrm{e}^{-jks'}}_{\text{Phase factor}}, \tag{3.28}$$

with $\boldsymbol{E}_i(Q_r)$ the incident electric field phasor at the point of reflection. The radii of curvature of the reflected wavefront ρ_1^r and ρ_2^r are linked to the incident wave's radii of curvature, as stated in [45]. In the case of spherical waves and planar interfaces, $\rho_1^r = \rho_2^r = s$ and equation (3.28) reduces to

$$\boldsymbol{E}_r(s') = \boldsymbol{E}_i(Q_r) \cdot \overline{\mathbf{R}}\ \frac{s}{s + s'}\,\mathrm{e}^{-jks'}, \tag{3.29}$$

---

[3] In this case, one talks about *effective relative permittivity*, ϵ_r^{eff}.

with s the path of the incident ray from its reference to the reflection point.

Similar developments can be done for the transmitted field but it is not often considered for RT simulations, except when outdoor to indoor propagation is studied.

3.3 Edge diffraction

Another common wave propagation mechanism modeled in RT is the diffraction by an edge, for which GO must be extended. Indeed, geometrical optics, along with its law of reflection, is unable to predict the existence of field in shadow regions as well as the field in the shadow boundary. This field is known as a diffracted field. Historically, Keller presented his geometrical theory of diffraction (GTD) in 1953 [49] and published it in 1962 [50]. His work was further extended in 1974 by Kouyoumjian and Pathak, leading to the UTD [51].

In this work, only the diffraction by a straight edge is considered. For such a geometry, GO defines three regions [46], depicted in Figure 3.3, containing:

- incident and reflected fields in region I (lit region);
- incident field only in region II (lit region);
- no field in region III (shadow region).

The boundaries between the regions are the reflection shadow boundary (RSB) and the incident shadow boundary (ISB). Adding the GTD (and UTD), the total field in the different regions is given by [48]

$$\boldsymbol{E}_{tot} = \begin{cases} \boldsymbol{E}_i + \boldsymbol{E}_r + \boldsymbol{E}_d & \text{for } 0 \leq \phi < \pi - \phi_{inc} \text{ (Region I)}, \\ \boldsymbol{E}_i + \boldsymbol{E}_d & \text{for } \pi - \phi_{inc} < \phi < \pi + \phi_{inc} \text{ (Region II)}, \\ \boldsymbol{E}_d & \text{for } \pi + \phi_{inc} < \phi \leq 2\pi - \alpha \text{ (Region III)}, \end{cases} \tag{3.30}$$

with $\boldsymbol{E}_i$ the incident electric field, $\boldsymbol{E}_r$ the reflected field and $\boldsymbol{E}_d$ the diffracted field. Moreover, α is the interior angle of the edge and ϕ_{inc} is the angle between the incident ray and one face of the edge. Usually the two faces are named "o" and "n", choosing the "o-face" as reference for $\phi = 0$ such that the "n-face" is in $\phi = n\pi$, with the parameter n defined by $n = 2 - \alpha/\pi$ [48]. Then, the value of $\boldsymbol{E}_d$ is either given by the GTD or the UTD.

3.3.1 Geometrical theory of diffraction

Geometrically, the position of the diffraction point on the edge can be found using Keller's law of diffraction:

Law of diffraction (Keller) "*A diffracted ray and the corresponding incident ray make equal angles with the edge at the point of diffraction, provided they are in the same medium. They lie on opposite sides of the plane normal to the edge at the point of diffraction* [46]."

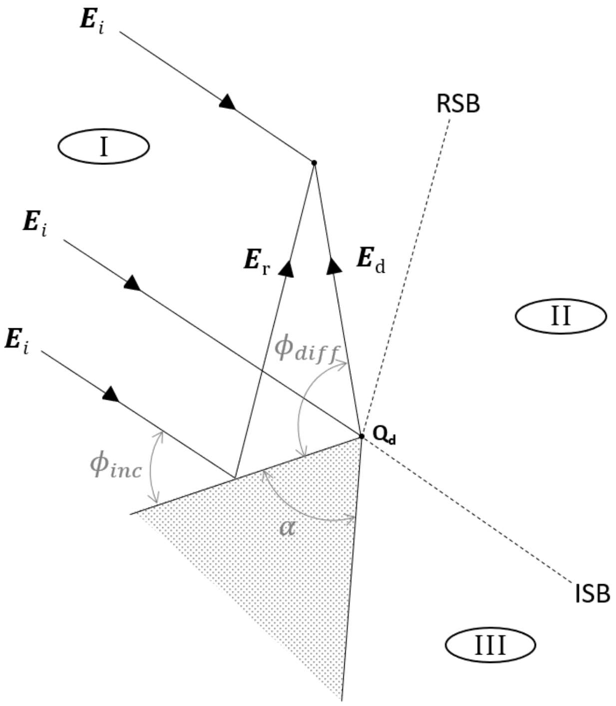

Figure 3.3: Geometry for diffraction by an edge (reproduced from [48])

This means that for an incident ray forming an angle $\beta_{0,inc}$ with an edge, all diffracted rays will form a cone of diffraction with an angle $\beta_{0,diff}$, such that $\beta_{0,inc} = \beta_{0,diff} := \beta_0$. The position of the diffraction point Q_d can then be found thanks to

$$\sin(\beta_0) \;=\; |\hat{\boldsymbol{s}}_i \;\times\; \hat{\boldsymbol{t}}| \;=\; |\hat{\boldsymbol{s}}_d \;\times\; \hat{\boldsymbol{t}}|, \tag{3.31}$$

with $\hat{\boldsymbol{t}}$ the unit vector tangent to the edge, $\hat{\boldsymbol{s}}_i$ and $\hat{\boldsymbol{s}}_d$ being the unit vectors along the direction of propagation of the incident and diffracted rays (see Figure 3.4).

Knowing the position of the diffraction point, the GTD can then give the value of the diffracted field based on diffraction coefficients. However, these coefficients are not detailed here since the GTD has been superseded by the UTD. Indeed, the main drawback of the GTD is that its diffraction coefficients become singular in the transition regions surrounding the shadow boundaries. This problem is solved in the UTD by adding a transition function in the coefficients. Nevertheless, the GTD remains very useful to identify the geometric positions of the diffraction points.

3.3.2 Uniform theory of diffraction

Considering **straight edges** and **spherical waves**, the UTD diffracted field at a distance s' from the point of diffraction (Q_d) is given by [45, 48]

$$\boldsymbol{E}_d(s') \;=\; \boldsymbol{E}_i(Q_d) \;\cdot\; \overline{\mathbf{D}} \;\sqrt{\frac{s}{s'(s+s')}}\;\mathrm{e}^{-jks'}, \tag{3.32}$$

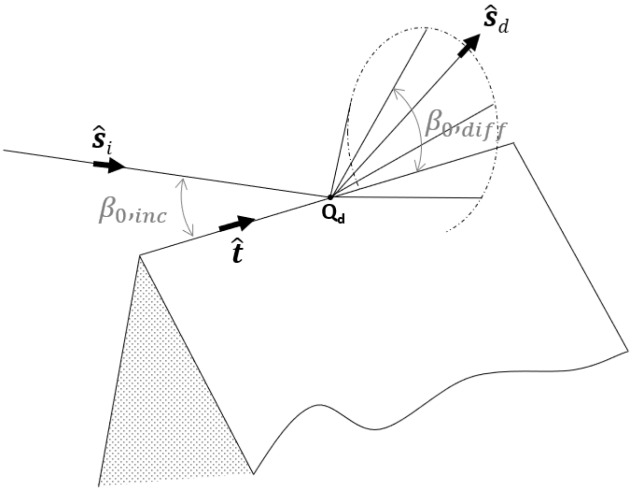

Figure 3.4: Cone of diffracted rays (reproduced from [48])

with s the path of the incident ray from its reference to the diffraction point. The dyadic coefficient $\overline{\mathbf{D}}$ is a matrix gathering the UTD coefficients, defined by [45, 48]

$$\overline{\mathbf{D}} = -D_s\,\hat{\boldsymbol{\beta}}_i\hat{\boldsymbol{\beta}}_d - D_h\,\hat{\boldsymbol{\phi}}_i\hat{\boldsymbol{\phi}}_d, \tag{3.33}$$

$$D_{s,h} = D_1 + D_2 + R_{s,h}\,(D_3 + D_4), \tag{3.34}$$

with $R_{s,h} = \pm 1$ being the reflection coefficients for a **perfectly conducting surface**.

The vectors involved in equation (3.33) come from edge-fixed coordinate systems, such that

$$\left(\hat{\boldsymbol{s}}_i\,,\,\hat{\boldsymbol{\beta}}_i\,,\,\hat{\boldsymbol{\phi}}_i\right) \quad \text{with} \quad \hat{\boldsymbol{\phi}}_i = \frac{\hat{\boldsymbol{s}}_i \times \hat{\boldsymbol{t}}}{|\hat{\boldsymbol{s}}_i \times \hat{\boldsymbol{t}}|} \quad \text{and} \quad \hat{\boldsymbol{\beta}}_i = \hat{\boldsymbol{\phi}}_i \times \hat{\boldsymbol{s}}_i, \tag{3.35}$$

$$\left(\hat{\boldsymbol{s}}_d\,,\,\hat{\boldsymbol{\beta}}_d\,,\,\hat{\boldsymbol{\phi}}_d\right) \quad \text{with} \quad \hat{\boldsymbol{\phi}}_d = \frac{\hat{\boldsymbol{s}}_d \times \hat{\boldsymbol{t}}}{|\hat{\boldsymbol{s}}_d \times \hat{\boldsymbol{t}}|} \quad \text{and} \quad \hat{\boldsymbol{\beta}}_d = \hat{\boldsymbol{\phi}}_d \times \hat{\boldsymbol{s}}_d. \tag{3.36}$$

The components of the diffraction coefficients D_1 and D_2 correspond to the diffraction of the incident field, whereas D_3 and D_4 correspond to the diffraction of the reflected field. They are given by [48]

$$D_1 = \frac{-e^{-j\pi/4}}{2n\sqrt{2\pi k}\sin(\beta_0)}\cot\left(\frac{\pi + (\phi_{diff} - \phi_{inc})}{2n}\right)F\left(kL\,a^{+}\left(\phi_{diff} - \phi_{inc}\right)\right), \tag{3.37}$$

$$D_2 = \frac{-e^{-j\pi/4}}{2n\sqrt{2\pi k}\sin(\beta_0)}\cot\left(\frac{\pi - (\phi_{diff} - \phi_{inc})}{2n}\right)F\left(kL\,a^{-}\left(\phi_{diff} - \phi_{inc}\right)\right), \tag{3.38}$$

$$D_3 = \frac{-e^{-j\pi/4}}{2n\sqrt{2\pi k}\sin(\beta_0)}\cot\left(\frac{\pi + (\phi_{diff} + \phi_{inc})}{2n}\right)F\left(kL\,a^{+}\left(\phi_{diff} + \phi_{inc}\right)\right), \tag{3.39}$$

$$D_4 = \frac{-e^{-j\pi/4}}{2n\sqrt{2\pi k}\sin(\beta_0)}\cot\left(\frac{\pi - (\phi_{diff} + \phi_{inc})}{2n}\right)F\left(kL\,a^{-}\left(\phi_{diff} + \phi_{inc}\right)\right). \tag{3.40}$$

The transition function $F(x)$ is related to Fresnel integrals and is defined by

$$F(x) = 2j\sqrt{x}\,e^{jx}\int_{\sqrt{x}}^{\infty} e^{-ju^2}du. \tag{3.41}$$

The coefficients $a^{\pm}(y)$ come from

$$a^{\pm}(y) \;=\; 2\cos^2\left(\frac{2n\pi N^{\pm} - y}{2}\right), \tag{3.42}$$

with the integers $N^{\pm}$ that most nearly satisfy $2n\pi N^{\pm} - y \;=\; \pm\pi$.

L is a distance parameter and for straight edges and spherical wavefront, is given by

$$L \;=\; \frac{s\,s'}{s+s'}\sin^2(\beta_0). \tag{3.43}$$

As already stated, the expression of the diffraction coefficients given in (3.34) is only valid for perfectly conducting surfaces. For surfaces with finite conductivity, a generalisation has been suggested by Luebbers in 1984, involving the reflection coefficients of the "*o-*" and "*n-faces*" of the edge [52]:

$$D_{s,h} \;=\; D_1 + D_2 + R^{n}_{s,h}\,D_3 + R^{o}_{s,h}\,D_4. \tag{3.44}$$

However, this generalisation presented by Luebbers is not reciprocal and is inaccurate in the shadow regions [53]. Based on the expression of Luebbers' coefficients, the Guevara's coefficients have been derived as another heuristic UTD model for lossy surfaces. These latter ensure reciprocity by changing the face assignment ("*o-*" or "*n-faces*") depending on the region from which the incident ray is coming. Furthermore, the angles used to compute Fresnel reflection coefficients are also slightly adapted [53].

3.4 Software implementation

Based on the theory presented in previous sections, RT software can be designed. For a given environment geometry as input, these tools provide a geometric description of all the rays linking a transmitter and a receiver, as well as the values of the electric field phasor for each ray observed at RX.

The computation of the electric field associated with a given ray directly involves equations (3.29) and (3.32) for example, and is possible only if the ray geometry is known. In order to obtain this latter, the (geometric) laws of reflection and diffraction are used. The purpose of the following subsections is to present some numerical and efficient implementations of these laws.

3.4.1 Computation of reflection points

To determine the geometric positions of reflection points, the image method is usually used. As a first step, the image point of either the receiver or the transmitter is determined. With homogeneous coordinates[4], the image point for an arbitrary plane can be found thanks to matrix computation, i.e. $\boldsymbol{x'} \;=\; \mathbf{M}\,\boldsymbol{x}$, with $\mathbf{M}$ given by [54]

$$\mathbf{M} \;=\; \mathbf{T}(-p_x,-p_y,-p_z)\;\mathbf{M}_x(\theta_x)\;\mathbf{M}_y(-\theta_y)\;\mathbf{I}_{xy}\;\mathbf{M}_y(\theta_y)\;\mathbf{M}_x(-\theta_x)\;\mathbf{T}(p_x,p_y,p_z), \tag{3.45}$$

---

[4] Using homogeneous coordinates, a point (x, y, z) in the three-dimensionnal space $\mathbb{R}^3$ is represented by a vector $(\lambda x, \lambda y, \lambda z, \lambda)$ in $\mathbb{R}^4$, with λ being a scaling factor different from zero. It enables to represent common transformations of space, such as translations, rotations, scalings or perspective projections, with matrix multiplications.

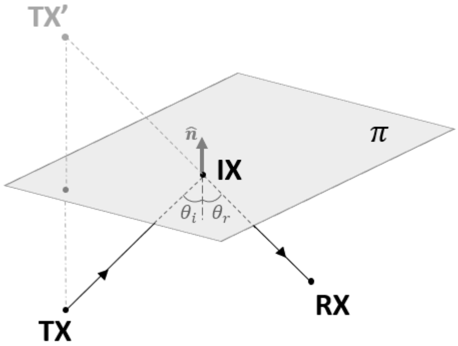

Figure 3.5: Illustration of image method (TX, TX' and RX lie in the same incidence plane)

where $\mathbf{T}$ is a translation matrix associated with a point $\boldsymbol{P} : (p_x, p_y, p_z)^T$ belonging to the plane; $\mathbf{M}_x(\theta_x)$ and $\mathbf{M}_y(\theta_y)$ are rotation matrices, respectively with respect to the x- and y-axis, of angles θ_x and θ_y that are such that $\sin(\theta_x) = n_y/\sqrt{n_y^2 + n_z^2}$, $\cos(\theta_x) = n_z/\sqrt{n_y^2 + n_z^2}$, $\sin(\theta_y) = n_x$ and $\cos(\theta_y) = \sqrt{n_y^2 + n_z^2}$, with $\hat{\boldsymbol{n}} : (n_x, n_y, n_z)^T$ the normal to the plane. Finally, $\mathbf{I}_{xy}$ is the reflection matrix associated with the plane x-y [54].

Then, the reflection point is found to be located at the intersection between the plane and the line passing through the receiver RX and the image of the transmitter TX', as seen in Figure 3.5 (or equivalently, the line going through the transmitter TX and the image of the receiver RX').

3.4.2 Computation of diffraction points

As stated in [27], the geometric application of Keller's law of diffraction can be performed using similar triangles, see Figure 3.6. Indeed, these triangles are obtained by projecting the incident and diffracted rays on the edge. Then, the evaluation of the distances B-Rx and A-Tx enables to find the aspect ratios of the triangles, and thus the distances B-Q_d and A-Q_d, which gives the position on the edge of the diffraction point Q_d. More details are given in Section 4.1.2.1, related to the tracking of diffraction points.

3.4.3 UCLouvain ray tracing software

UCLouvain RT software is based on [27, 33] and involves the methods presented previously to compute the positions of reflection and diffraction points. On top of that, the BSP tree is used to partition the geometry and enable faster computation of polygon visibility [33]. Moreover, the software is limited to one diffraction, which is only possible at the last interaction.[5]

For each ray, it outputs a cell of type "*ray*", containing all the quantities given in Table 3.1. Based on these quantities, other quantities, metrics or figures of merit can be derived (see Chapter 5).

---

[5] This strong hypothesis helps to drastically reduce the complexity of the RT software, in terms of implementation and computation time.

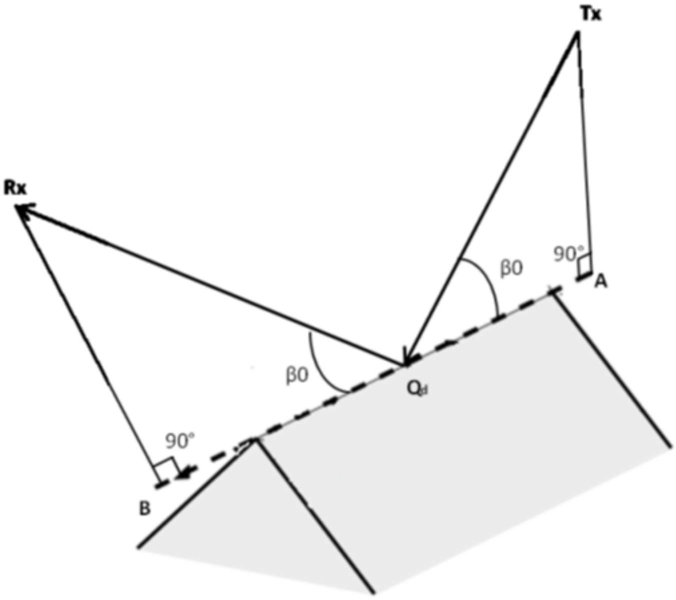

Figure 3.6: Geometry for the determination of the diffraction point (Source: [27])

Quantity	Description	Unit
Order	Number of interactions (0 = LOS,...)	-
Type	1: Only reflections 2: Reflections with diffraction at last interaction	-
$E_{\phi,x}$	x-component of azimuthal electric field	[V/m]
$E_{\phi,y}$	y-component of azimuthal electric field	[V/m]
$E_{\phi,z}$	z-component of azimuthal electric field	[V/m]
$E_{\theta,x}$	x-component of elevation electric field	[V/m]
$E_{\theta,y}$	y-component of elevation electric field	[V/m]
$E_{\theta,z}$	z-component of elevation electric field	[V/m]
θ_{RX}	Elevation angle of arrival, at RX	[rad]
ϕ_{RX}	Azimuth angle of arrival, at RX	[rad]
θ_{TX}	Elevation angle of departure, at TX	[rad]
ϕ_{TX}	Azimuth angle of departure, at TX	[rad]
d	Total distance traveled by the ray, between TX and RX	[m]
RX index	Index of the receiver (if several RXs)	-

Table 3.1: Quantities in a *ray cell*

The various components of the electric field phasor and vector $\boldsymbol{E}$ given in Table 3.1 are linked with the following relations:

$$\begin{aligned} E_x &= E_{\phi,x} + E_{\theta,x} \\ E_y &= E_{\phi,y} + E_{\theta,y} \\ E_z &= E_{\phi,z} + E_{\theta,z} \\ E_\phi &= \sqrt{E_{\phi,x}^2 + E_{\phi,y}^2 + E_{\phi,z}^2} \\ E_\theta &= \sqrt{E_{\theta,x}^2 + E_{\theta,y}^2 + E_{\theta,z}^2} \end{aligned} \quad \Rightarrow \quad \boldsymbol{E} = E_x\,\hat{\boldsymbol{x}} + E_y\,\hat{\boldsymbol{y}} + E_z\,\hat{\boldsymbol{z}} = E_\phi\,\hat{\boldsymbol{\phi}} + E_\theta\,\hat{\boldsymbol{\theta}},$$

since, in the ray-associated frame $(\hat{\boldsymbol{s}}, \hat{\boldsymbol{\phi}}, \hat{\boldsymbol{\theta}})$, there is no field component in the direction of propagation $\hat{\boldsymbol{s}}$, and $(\hat{\boldsymbol{x}}, \hat{\boldsymbol{y}}, \hat{\boldsymbol{z}})$ is the cartesian frame.

3.5 Summary of ray propagation

This chapter presented the ray concept as an approximate high-frequency solution of Maxwell's equations (i.e. in the framework of GO). As derived previously, the main characteristics of a ray are:

- The LOS propagation of a ray is given by the eikonal equation. In the case of homogeneous media, a ray travels in straight line;
- Rays carry energy and should actually be modeled as tubes. As such, a spreading factor is used to take into account the spreading of the energy, and depends on the considered type of waves (plane, cylindrical or spherical);
- At (infinite) interfaces, rays obey the laws of reflection and refraction, involving Fresnel coefficients;
- Close to edges, rays are diffracted following the law of diffraction, with diffraction coefficients given by the UTD.

These are really the basic characteristics of rays used in RT. However, the ray concept is often extended to add other propagation mechanisms, such as reflection on curved surfaces, diffraction on curved edges, scattering from rough surfaces, attenuation by vegetation,... [27].

Finally, some basic software implementations of RT have been given and Table 3.1 summarized the outputs of UCLouvain RT software.

Chapter 4

Dynamic Ray Tracing

In the previous chapter, RT has been introduced. As long as the geometry of the environment is known, it enables to completely characterize a communication channel, i.e. determine all rays linking the transmitter and the receiver.

In this work, focus is given to time-varying geometries where one would like to know the communication channel not only at a given instant but also during a given time interval. This could be handled by performing RT simulations at each instant. However, this would be quite computationally expensive. Instead, a DRT approach is investigated in this chapter. It relies on a single RT simulation and a perfect knowledge of the environment and its time evolution. Doing so, it is possible to predict the evolution of any ray identified by the RT simulation, thanks to the tracking of the interaction points (i.e. reflection and diffraction points).

First, a description of the DRT approach is presented, along with the necessary equations enabling to track reflection and diffraction points. Then, two possible implementations of DRT are given and the approach is validated on simple examples.

4.1 Description of dynamic ray tracing

To extrapolate the geometry of a given ray, one needs to characterize the time evolution of the positions of any of the interaction points constituting this ray. From the geometry of the problem, the following quantities are known:

- the position and velocity of the transmitter and the receiver;
- the position and velocity of any body (buildings, vehicles, etc.) in the environment.

This information can be stored in a database containing the description of the environment geometry at any instant, especially if the velocities are time-varying. However, it will be often assumed in this work that all velocities are constant during the channel stationarity time, i.e. the time during which the main MPCs are related to the same rays. This is a strong assumption as this time will depend on the considered geometries and is not known beforehand. Furthermore, rigid-body rotations or deformations are not allowed. With such assumptions, only the initial positions along with the constant values of the (initial) velocities are needed.

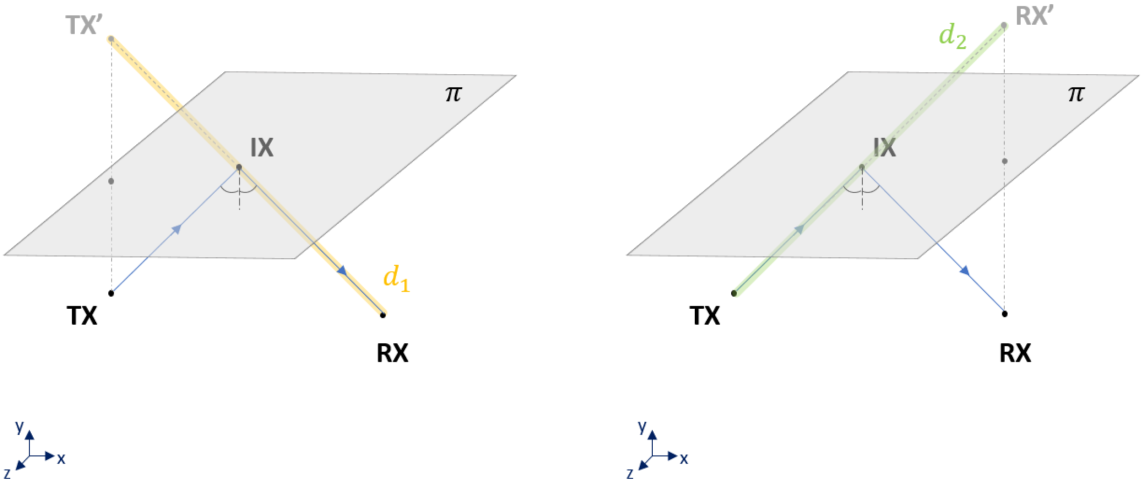

Figure 4.1: Reflection on a horizontal plane - TX *and* RX *are below the plane*

Then, from a unique RT simulation at time t_0, it is possible to extract the positions of all interaction points (all reflection and diffraction points). From the initial positions, the motion of these points can be fully characterized by computing their instantaneous positions and velocities.

The equations stating the positions and the velocities of reflection points for a horizontal plane are first derived, before being generalized to oblique and multiple planes. Next, a similar approach is applied to diffraction points.

4.1.1 Tracking of reflection points

4.1.1.1 Horizontal plane

A simple 3D case is considered, with a horizontal plane, a transmitter and a receiver located at different heights. The transmitter and receiver positions are known, as well as the position of the reflecting plane:

$$\text{TX}: \ (x_{TX}, y_{TX}, z_{TX})^T \qquad\qquad \text{RX}: \ (x_{RX}, y_{RX}, z_{RX})^T. \tag{4.1}$$

The plane, assumed infinite for the moment, has for equation

$$\Pi: \ y = y_w \qquad \text{and} \qquad x, z \in \mathbb{R}. \tag{4.2}$$

The first step is to characterize the position of the reflection point on the plane, denoted by IX. This can be achieved thanks to the image method with orthogonal projections (i.e. projections along the direction of the normal vector of the plane), ensuring that the distance between TX (resp. RX) and the plane Π is the same as the distance between TX' (resp. RX') and Π. This is depicted in Figure 4.1.

Then, as already stated in Section 3.4.1, the reflection point IX is at the intersection between the plane Π and the lines going through either the image of the transmitter TX' and the receiver RX, or the transmitter TX and the image of the receiving point RX'. These lines are called d_1 and d_2, having for equations:

$$d_1: \quad \frac{x - x_{TX'}}{x_{RX} - x_{TX'}} = \frac{y - y_{TX'}}{y_{RX} - y_{TX'}} = \frac{z - z_{TX'}}{z_{RX} - z_{TX'}}, \tag{4.3}$$

$$d_2: \quad \frac{x - x_{RX'}}{x_{TX} - x_{RX'}} = \frac{y - y_{RX'}}{y_{TX} - y_{RX'}} = \frac{z - z_{RX'}}{z_{TX} - z_{RX'}}, \tag{4.4}$$

with the positions of TX' and RX' given by

$$\mathrm{TX}' : (x_{TX'}, y_{TX'}, z_{TX'})^T = (x_{TX}, 2y_w - y_{TX}, z_{TX})^T, \tag{4.5}$$

$$\mathrm{RX}' : (x_{RX'}, y_{RX'}, z_{RX'})^T = (x_{RX}, 2y_w - y_{RX}, z_{RX})^T. \tag{4.6}$$

Since the reflection point IX belongs to the plane, substitution of y by y_w in equations (4.3-4.4) leads to the expressions of its position $(x_{IX}, y_{IX}, z_{IX})^T$:

$$\text{Using } d_1\text{:} \begin{cases} x_{IX} &= x_{TX} + \left(\frac{x_{RX} - x_{TX}}{y_{RX} - 2y_w + y_{TX}}\right)(y_{TX} - y_w) \\ y_{IX} &= y_w \\ z_{IX} &= z_{TX} + \left(\frac{z_{RX} - z_{TX}}{y_{RX} - 2y_w + y_{TX}}\right)(y_{TX} - y_w) \end{cases}, \tag{4.7}$$

$$\text{Using } d_2\text{:} \begin{cases} x_{IX} &= x_{RX} - \left(\frac{x_{RX} - x_{TX}}{y_{RX} - 2y_w + y_{TX}}\right)(y_{RX} - y_w) \\ y_{IX} &= y_w \\ z_{IX} &= z_{RX} - \left(\frac{z_{RX} - z_{TX}}{y_{RX} - 2y_w + y_{TX}}\right)(y_{RX} - y_w) \end{cases}. \tag{4.8}$$

Equations (4.7) and (4.8) are equivalent. In these equations, one can notice that coordinates x and z can be treated independently since they do not influence each other. Deriving these last expressions with respect to the time gives the instantaneous velocity of the reflection point. Assuming a purely vertical motion for the plane (with speed $v_{w,y}$) and constant velocities for the transmitter and the receiver, i.e.

$$\boldsymbol{v}_{TX} = (v_{TX,x}\ ,\ v_{TX,y}, v_{TX,z})^T\ , \tag{4.9}$$

$$\boldsymbol{v}_{RX} = (v_{RX,x}\ ,\ v_{RX,y}, v_{RX,z})^T\ , \tag{4.10}$$

the x-velocity of IX is given by

$$v_{IX,x} = \frac{dx_{IX}}{dt} = \frac{\partial x_{IX}}{\partial x_{TX}}\frac{dx_{TX}}{dt} + \frac{\partial x_{IX}}{\partial y_{TX}}\frac{dy_{TX}}{dt} + \frac{\partial x_{IX}}{\partial x_{RX}}\frac{dx_{RX}}{dt} + \frac{\partial x_{IX}}{\partial y_{RX}}\frac{dy_{RX}}{dt} + \frac{\partial x_{IX}}{\partial y_w}\frac{dy_w}{dt}, \tag{4.11}$$

$$= \frac{\partial x_{IX}}{\partial x_{TX}} v_{TX,x} + \frac{\partial x_{IX}}{\partial y_{TX}} v_{TX,y} + \frac{\partial x_{IX}}{\partial x_{RX}} v_{RX,x} + \frac{\partial x_{IX}}{\partial y_{RX}} v_{RX,y} + \frac{\partial x_{IX}}{\partial y_w} v_{w,y}, \tag{4.12}$$

with all derivatives

$$\frac{\partial x_{IX}}{\partial x_{TX}} = \frac{y_{RX} - y_w}{y_{RX} - 2y_w + y_{TX}} \qquad \frac{\partial x_{IX}}{\partial y_{TX}} = \frac{(x_{RX} - x_{TX})(y_{RX} - y_w)}{(y_{RX} - 2y_w + y_{TX})^2} \tag{4.13}$$

$$\frac{\partial x_{IX}}{\partial x_{RX}} = \frac{y_{TX} - y_w}{y_{RX} - 2y_w + y_{TX}} \qquad \frac{\partial x_{IX}}{\partial y_{RX}} = -\frac{(x_{RX} - x_{TX})(y_{TX} - y_w)}{(y_{RX} - 2y_w + y_{TX})^2} \tag{4.14}$$

$$\frac{\partial x_{IX}}{\partial y_w} = \frac{(x_{RX} - x_{TX})(y_{TX} - y_{RX})}{(y_{RX} - 2y_w + y_{TX})^2}. \tag{4.15}$$

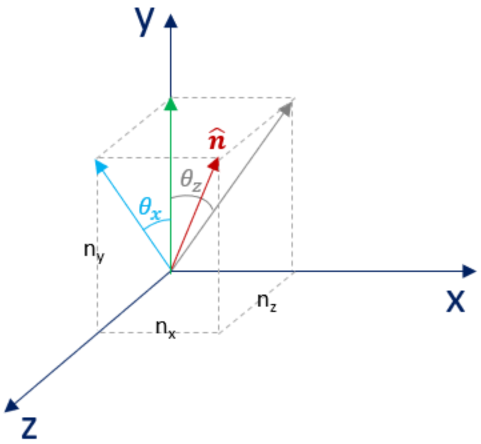

Figure 4.2: Representation of 3D normal vector and associated angles

This last result comes from the first equation in (4.7), and the same approach can be performed to obtain the z-velocity (which is equivalent to substitute all x by z in equations 4.11 to 4.15). The y-velocity of IX is given by $v_{w,y}$.

Equation 4.12 stipulates that the instantaneous velocity of the reflection point depends on the velocities of the transmitter, receiver and plane, as well as on their instantaneous positions. **This velocity is thus not constant even if the TX, RX or the plane velocities are assumed to be constant.**

4.1.1.2 Oblique plane

Mathematical expressions derived previously assumed the plane to be horizontal, meaning that its normal is along the y-axis: $\hat{\boldsymbol{n}} = (0, \pm 1, 0)$. Nevertheless, oblique planes can be handled using a change of coordinate system in order to end up in the local frame associated with the plane (i.e. the frame where the normal is aligned with the y-axis). Therefore, for an oblique plane with an arbitrary normal vector $\hat{\boldsymbol{n}} = (n_x, n_y, n_z)$, one can find two successive rotations that will align the normal of the plane with the y-axis. Figure 4.2 gives the coordinate system and the angles used to perform the rotation of vector $\hat{\boldsymbol{n}}$ to a vector aligned with the y-axis.

First, a rotation around z-axis of angle θ_z is performed on $\hat{\boldsymbol{n}}$, leading to the blue vector, with

$$\mathbf{M}_z(\theta_z) = \begin{bmatrix} \cos(\theta_z) & -\sin(\theta_z) & 0 \\ \sin(\theta_z) & \cos(\theta_z) & 0 \\ 0 & 0 & 1 \end{bmatrix} = \begin{bmatrix} \frac{n_y}{\sqrt{n_x^2+n_y^2}} & -\frac{n_x}{\sqrt{n_x^2+n_y^2}} & 0 \\ \frac{n_x}{\sqrt{n_x^2+n_y^2}} & \frac{n_y}{\sqrt{n_x^2+n_y^2}} & 0 \\ 0 & 0 & 1 \end{bmatrix}, \tag{4.16}$$

$$\mathbf{M}_z(\theta_z) \begin{bmatrix} n_x \\ n_y \\ n_z \end{bmatrix} = \begin{bmatrix} 0 \\ \sqrt{n_x^2 + n_y^2} \\ n_z \end{bmatrix}. \tag{4.17}$$

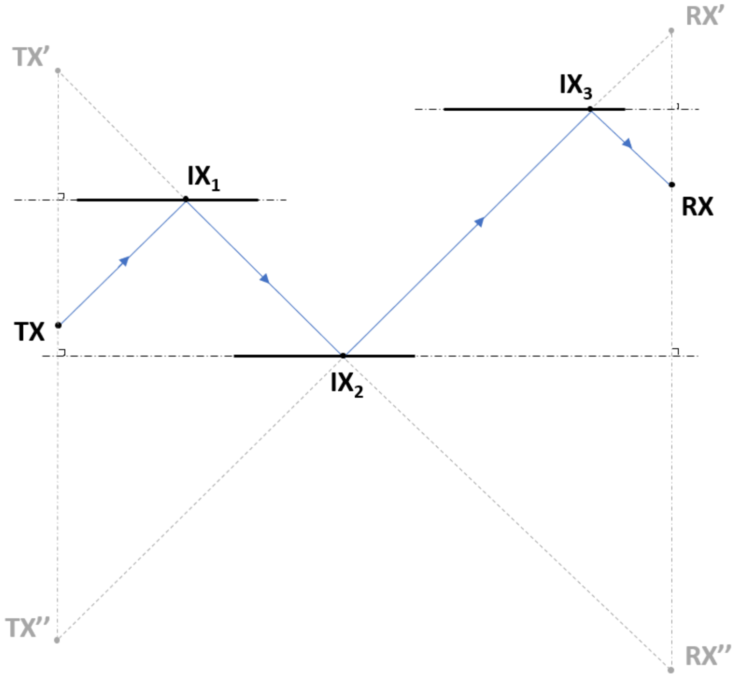

Figure 4.3: Example of generalization to three planes, in 2D

After that, a rotation around x-axis is applied to the blue vector of Figure 4.2, given by

$$\mathbf{M}_x(\theta_x) = \begin{bmatrix} 1 & 0 & 0 \\ 0 & \cos(\theta_x) & -\sin(\theta_x) \\ 0 & \sin(\theta_x) & \cos(\theta_x) \end{bmatrix} = \begin{bmatrix} 1 & 0 & 0 \\ 0 & \sqrt{n_x^2+n_y^2} & -n_z \\ 0 & n_z & \sqrt{n_x^2+n_y^2} \end{bmatrix}, \tag{4.18}$$

since $\hat{\boldsymbol{n}}$ is normalized ($\sqrt{n_x^2+n_y^2+n_z^2}=1$).

In short, the combined rotation matrix $\mathbf{M} = \mathbf{M}_x(\theta_x)\mathbf{M}_z(\theta_z)$ is first applied to all quantities (TX/RX positions and velocities, and plane position and velocity). Then, the reflection point is computed with the equations from the previous section. Finally, the inverse rotation matrix is applied to the obtained vector to get back to the original frame.

4.1.1.3 Generalization to multiple planes

Generalization to an arbitrary number of planes is not straightforward. Simply taking the previous and the next interaction points to be respectively the transmitter and the receiver of the plane currently under consideration (i.e. the plane for which one wants to characterize the motion of its interaction point) leads to a significant coupling between equations. Indeed, for the geometry given in Figure 4.3 for example, the motion of the interaction point IX$_2$ is influenced by the motion of IX$_1$ and IX$_3$, but also influences their motions.

Instead, it is possible to use corresponding images of the transmitter and the receiver as TX and RX for the plane under consideration. This means, for example, that TX' and RX' are used in Figure 4.3 to characterize the motion of IX$_2$. By doing so, the motion of each interaction point can be computed independently (applying equations (4.7) or (4.8) for example), but this is only possible if the instantaneous positions (and velocities) of TX and

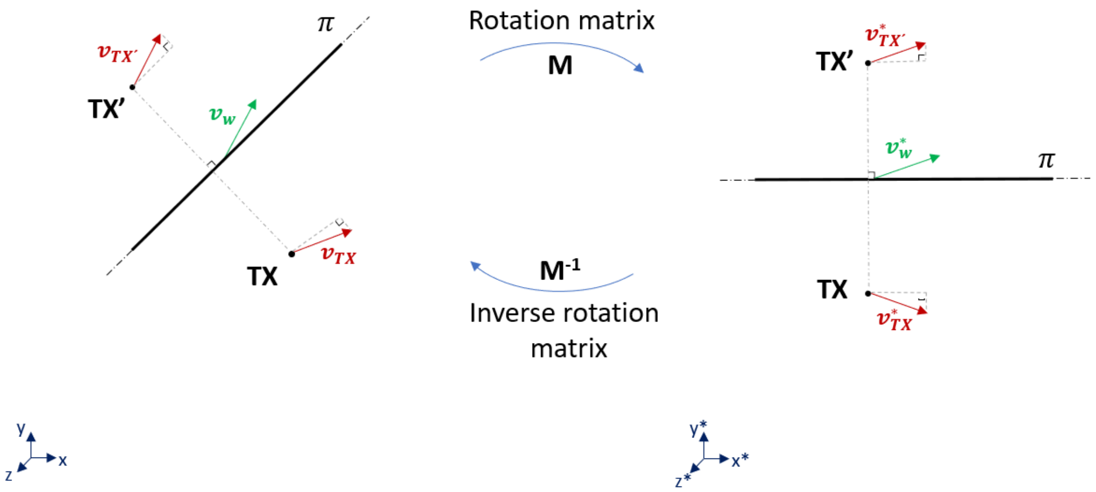

Figure 4.4: Computation of image points velocity

RX images are known. These depend on the TX and RX initial positions and velocities, as well as the velocities of all planes used to construct the image points.

Thanks to the assumption of constant velocities, the velocities of the image points will also be constant and can therefore be computed once, during the first RT iteration. Indeed, considering one plane for computing TX' (resp. RX'), the components of TX (resp. RX) velocity orthogonal to the normal vector of this plane are conserved, while the component aligned with the normal vector is reversed and augmented by twice the velocity of the plane. One should thus reason in the local frame associated with the plane (i.e. after having applied the rotation matrix **M** of the plane), as depicted in Figure 4.4. Then, the velocity of the TX image point, for example, is given by

$$\begin{cases} v^*_{TX',x^*} &= v^*_{TX,x^*} \\ v^*_{TX',y^*} &= 2v^*_{w,y^*} - v^*_{TX,y^*} \\ v^*_{TX',z^*} &= v^*_{TX,z^*} \end{cases} , \tag{4.19}$$

with $[.]^*$ denoting the local frame coordinates ($\boldsymbol{v}^*_{TX} = \mathbf{M}\,\boldsymbol{v}_{TX}$ and $\boldsymbol{v}^*_w = \mathbf{M}\,\boldsymbol{v}_w$). The rotation matrix **M** is the same as the one computed previously for this plane, in Section 4.1.1.2.

After that, the inverse rotation matrix is applied to $\boldsymbol{v}^*_{TX'}$ to get back to the initial frame, i.e.

$$\boldsymbol{v}_{TX'} = \mathbf{M^{-1}} \left(v^*_{TX',x^*} \, , \, v^*_{TX',y^*} \, , \, v^*_{TX',z^*} \right)^T . \tag{4.20}$$

Similarly, velocities of RX image points are found and this approach can be generalized for any image points of the receiver or the transmitter. Indeed, for example, the velocity of TX", i.e. the second image point of TX, is computed recursively from $\boldsymbol{v}_{TX'}$ and the rotation matrix **M** associated with the second plane.

Finally, to obtain the positions of the image points at a given instant t from the initial positions (subscript 0), the following expressions are used (for TX' as an example):

$$\begin{cases} x_{TX'} &= x_{TX'_0} + v_{TX',x}\, t \\ y_{TX'} &= y_{TX'_0} + v_{TX',y}\, t \\ z_{TX'} &= z_{TX'_0} + v_{TX',z}\, t \end{cases} . \tag{4.21}$$

This simply corresponds to an analytical integration, made possible thanks to the constant velocities of the image points (and therefore thanks to the assumption of constant velocities for all the geometry).

4.1.2 Tracking of diffraction points

In a similar way to what has been done for the tracking of reflection points, the equations describing the positions of diffraction points are derived.

4.1.2.1 Canonical configuration

Following Keller's law of diffraction (see Section 3.3.1), the diffraction by an edge is depicted in Figure 4.5. In this canonical configuration, the edge vector $\hat{\boldsymbol{e}}$ is assumed to be aligned with the y-axis, i.e. $\hat{\boldsymbol{e}} = (0, 1, 0)^T$.

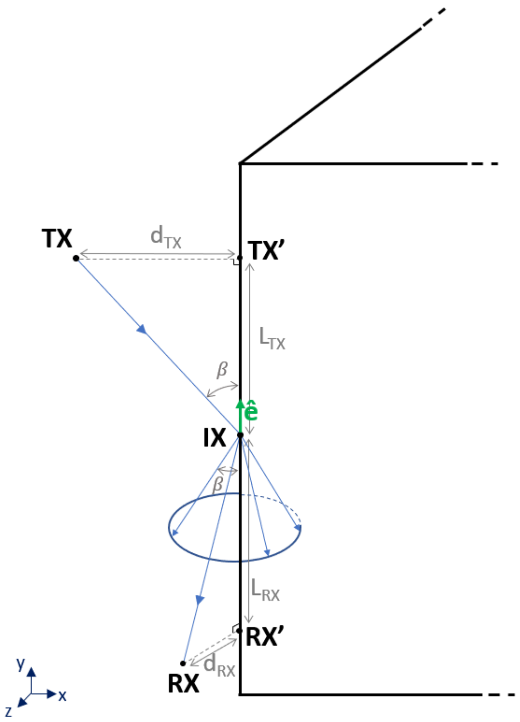

Figure 4.5: Diffraction by an edge

The goal is to characterize the position of the diffraction point IX : $(x_{IX}, y_{IX}, z_{IX})^T$. The known quantities are:

$$\text{TX}:\ (x_{TX}, y_{TX}, z_{TX})^T \qquad\qquad \text{RX}:\ (x_{RX}, y_{RX}, z_{RX})^T, \tag{4.22}$$

as well as the x- and z-position of the diffraction point IX, since the diffraction point must be located on the edge (which is assumed to be aligned with the y-axis). Therefore, we define $x_{IX} = x_e$ and $z_{IX} = z_e$, both known. Only y_{IX} remains to be computed, and this can be achieved using the theory of similar triangles (as already stated in Section 3.4.2).

First, the orthogonal projection on the edge of the transmitter and the receiver is performed, defining TX' and RX'. The points TX, TX' and IX form a right triangle, whereas the points RX, RX' and IX also define a right triangle, having the same angles. Therefore, these two triangles are similar and share the following properties in terms of distance ratios (distances are defined in Figure 4.5):

$$c := \frac{d_{TX}}{d_{RX}} = \frac{L_{TX}}{L_{RX}} \tag{4.23}$$

with

$$d_{TX} = \sqrt{\left(x_{TX} - x_e\right)^2 + \left(z_{TX} - z_e\right)^2} \qquad L_{TX} = y_{TX} - y_{IX} \tag{4.24}$$

$$d_{RX} = \sqrt{\left(x_{RX} - x_e\right)^2 + \left(z_{RX} - z_e\right)^2} \qquad L_{RX} = y_{IX} - y_{RX}. \tag{4.25}$$

Hence,

$$c = \frac{y_{TX} - y_{IX}}{y_{IX} - y_{RX}} \iff y_{IX} = \frac{y_{TX} + c\, y_{RX}}{c+1}, \tag{4.26}$$

leading to

$$y_{IX} = \frac{\sqrt{\left(x_{RX} - x_e\right)^2 + \left(z_{RX} - z_e\right)^2}\, y_{TX} + \sqrt{\left(x_{TX} - x_e\right)^2 + \left(z_{TX} - z_e\right)^2}\, y_{RX}}{\sqrt{\left(x_{TX} - x_e\right)^2 + \left(z_{TX} - z_e\right)^2} + \sqrt{\left(x_{RX} - x_e\right)^2 + \left(z_{RX} - z_e\right)^2}}, \tag{4.27}$$

$$x_{IX} = x_e \qquad \text{and} \qquad z_{IX} = z_e. \tag{4.28}$$

This equation enables to find directly the y-position of the diffraction point, knowing the edge position (x_e and z_e) and orientation (y-axis), and the TX and RX positions. It assumes the edge to be infinite, therefore one must verify whether the obtained position of IX belongs to the real edge, i.e. if the value of y_w is between the y-positions of the edge extremities.

Time derivation of equation (4.27) to obtain the instantaneous velocity of the diffraction point is not trivial and has not been further studied.

4.1.2.2 Oblique edge

As for reflections, if the edge is not oriented along the y-axis, a rotation matrix is first applied so that one ends up in the local coordinate system considered previously. This rotation matrix is the same as the one computed in Section 4.1.1.2, substituting the normal vector $\hat{\boldsymbol{n}}$ by the edge vector $\hat{\boldsymbol{e}}$. The edge vector (normed) is obtained thanks to the knowledge of the positions of the extremities of the edge.

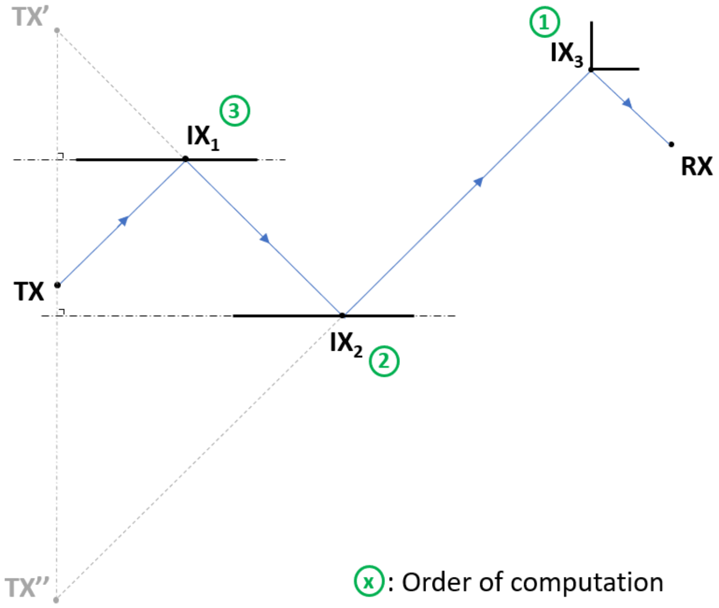

Figure 4.6: Generalization for diffraction - *First,* IX_3 *is determined thanks to* RX *and* TX". *Then,* IX_2 *can be found using* TX' *and* IX_3*. Finally,* IX_1 *is obtained with* TX *and* IX_2*.*

4.1.2.3 Generalization

Since it is assumed that diffraction is only possible at the last interaction, image points of the transmitter can only come from reflections. They are therefore computed the same way as above. However, there are not such receiver image points since the diffraction does not have image points, compared to reflections. Nevertheless, it is still possible to generalize to several interactions but one will not benefit from the decoupling of the equations previously found, i.e. while considering only reflections.

Indeed, using the transmitter image points, it is possible to determine the position of the diffraction point (at the last interaction) independently from the position of the reflection point(s). Knowing the position of the diffraction point, it can be used as receiver to determine the position of the previous reflection point. If there is a third interaction, again, the freshly computed reflection point is used as receiver for the new reflection point one would like to compute. By doing so, one is actually working backwards, starting by determining the last interaction point and then progressively all reflection points until the first one (see Figure 4.6). Such an approach, made only possible thanks to the fact that the diffraction is at the last interaction, can be generalized to one diffraction at any interaction. By recursively computing the TX and RX image points up to the diffraction, one can find the diffraction point and then work backwards. However, generalization to multiple diffraction in a single ray remains an open question.

4.2 Implementation

Based on the previous section, it is possible to track the positions of the interaction points, if, during an initial RT simulation, all the following quantities are recorded for each ray:

- Position and velocity of TX;
- Position and velocity of RX;
- For each wall/edge i interacting with the ray:
  - Reflection/diffraction point position (IX_i);
  - Velocity of the wall ($\boldsymbol{v}_w$);
  - Position and velocity of corresponding image of TX;
  - Position and velocity of corresponding image of RX.

This is done thanks to a dedicated data structure, which is then given to the next step of the DRT algorithm. Indeed, for each wall, relations from Section 4.1.1 can be applied **independently** and the positions of all the *reflection* points can be found at any instant.

Regarding rays involving a *diffraction*, the positions of RX image points do not exist (and are therefore not recorded). Thus, equation (4.27) is used first with the corresponding TX image points to find the diffraction point, before applying equations from Section 4.1.1 **recursively**.

Please note that this relies on the presented generalization approaches which are only possible if all the velocities of the geometry are constant. Otherwise, it is not possible to compute velocities of image points and record them once for all (i.e. during the initial RT simulation). Instead, they must be recomputed at each DRT iteration using the TX, RX and walls' velocities at this instant. This is possible since the dynamic evolution of the geometry is known.

In this section, two different approaches have been identified to evaluate the positions of the interaction points: either a step-by-step (numerical) integration, or a fully analytical integration. Both rely on different hypotheses.

4.2.1 Step-by-step (numerical) integration

This approach is particularly suited for geometries where the velocities of the bodies are time-varying, even though the presented generalization approach must be adapted to recompute the image point velocities at each instant. Nevertheless, it can be used and generalized for geometries having constant velocities.

In such an approach, the new positions of the TX, RX or interaction points are computed successively, by assuming the velocities to be constant only during a small time interval Δt. Two implementations are possible.

4.2.1.1 Closed-form for reflection only

If only reflections are considered, one can directly work on the positions of the reflection points IX and compute the following quantities:

$$\begin{cases} x_{IX}(t+\Delta t) & = x_{IX}(t) \ + \ v_{IX,x}(t)\,\Delta t \\ y_{IX}(t+\Delta t) & = y_{IX}(t) \ + \ v_{IX,y}(t)\,\Delta t \ , \\ z_{IX}(t+\Delta t) & = z_{IX}(t) \ + \ v_{IX,z}(t)\,\Delta t \end{cases} \tag{4.29}$$

with $\boldsymbol{v}_{IX}(t) = (v_{IX,x}(t), v_{IX,y}(t), v_{IX,z}(t))^T$ computed thanks to equation (4.12), using the velocities of TX-RX and the bodies at time t (if time-varying velocities), retrieved in the database description of the environment.

This leads to an iterative algorithm, starting from the results of the RT simulation, and updating the positions of the interaction points every Δt (see Algorithm 1).

```
Initial ray tracing simulation
for $t = 0 : \Delta t : end\_time$ do
    for each ray do
        if want to know the ray quantities at this instant $t$ then
            Plot the current ray trajectory
            Compute the physical quantities based on the ray geometry (Electric field,
              angles of departure and arrival,...)
        end
        Update the ray geometry by computing new IX positions
    end
end
```

Algorithm 1: Step-by-step integration

However, this implementation cannot be used with diffraction, the main reason being that the presented generalization for diffraction with multiple interactions does not allow independent computations for interaction points. Moreover, a closed-form for the velocity of a diffraction point has not been derived.

4.2.1.2 With analytical substitution, for reflection and diffraction

Here, the new positions of the TX, RX or their image points are first computed by numerical integration. For example, using:

$$\begin{cases} x_{TX}(t+\Delta t) & = x_{TX}(t) \ + \ v_{TX,x}(t)\,\Delta t \\ y_{TX}(t+\Delta t) & = y_{TX}(t) \ + \ v_{TX,y}(t)\,\Delta t \ . \\ z_{TX}(t+\Delta t) & = z_{TX}(t) \ + \ v_{TX,z}(t)\,\Delta t \end{cases} \tag{4.30}$$

Then, these positions can be substituted in the equations (4.7) and (4.27) to determine the position of the reflection points.

For geometries with constant velocities, this approach is equivalent to the analytical approach explained in the next section. Indeed, all $v_{TX,\cdot}(t)$ in equations (4.30) are now constant. Hence, no approximations regarding the velocities to be constant only during a small Δt are made and the obtained positions for TX, RX,... are infinitely accurate.

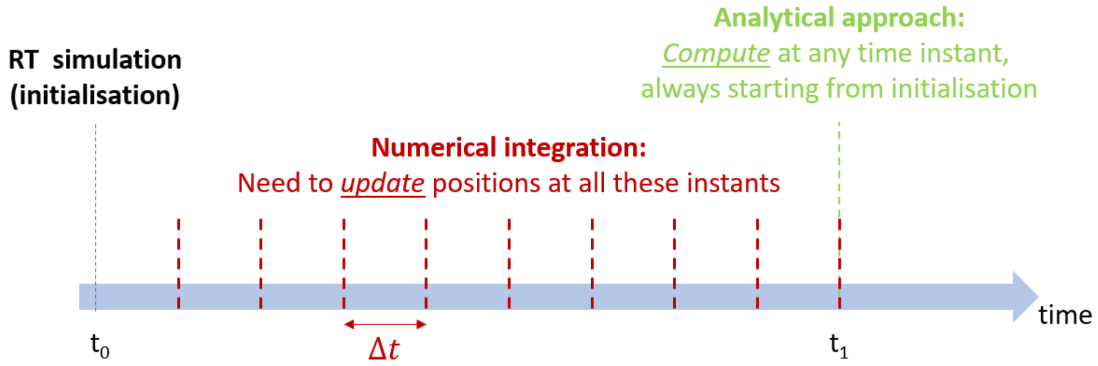

Figure 4.7: Representation of numerical and analytical approaches

4.2.2 Analytical approach

Thanks to the assumption of constant velocities for the transmitter, the receiver and any body of the geometry, a fully analytical approach is possible. Indeed, the time dependency can be made explicit in (4.7), stating $x_{TX} = x_{TX_0} + v_{TX,x}\, t$ for example (and so forth for all axis, RX and the plane y_w). Therefore, one only has to evaluate these equations at any desired instant, i.e. by substituting t. The same explicit time dependency is made in equation (4.27) for the diffraction.

4.2.3 Suppression of rays

All equations obtained in Section 4.1 assumed the planes or the edges to be infinite, which is not the case in practice. Hence, the computation of the new IX positions must be compared with the evolution of the geometry. Indeed, the computed IX positions may end up falling out of the body surface on which reflection was possible before, or out of the edge where there was a diffraction. In this case, the whole ray should be suppressed since it does not exist anymore and will not be found by the classical RT algorithm.

Such a ray-suppression mechanism is actually implemented after having computed the new IX positions, by checking that they still belong to the environment geometry.

4.2.4 Summary of possible implementations

For the sake of clarity, Figure 4.7 represents graphically the numerical and analytical approaches. Starting from a unique RT simulation performed at t_0, one would like to know the rays at time t_1. With the numerical approach, the ray positions must be updated every Δt up to t_1, whereas, with the analytical method, the new rays can directly be computed at time t_1.

On top of that, the numerical integration is further split in two: either it is directly performed on the reflection points (closed-form), or it first updates the TX, RX and their image point positions before involving evaluation of the analytical equations to get the reflection and diffraction point positions.

All possible implementations will now be compared on small examples, involving several and different hypotheses.

4.3 Geometric validation

Simple cases involving only one plane or one edge are first considered, to validate the tracking approach. Then, more complex geometries are studied, using the presented generalization methods. In most examples, constant velocities are considered so that a comparison between the numerical integration and the analytical approach is possible.

Some important precisions regarding the numerical integration:

- Sections 4.3.1 and 4.3.3, involving only reflections, use the closed-form numerical integration given in Section 4.2.1.1. Indeed, the other form of numerical integration is equivalent to analytical integration since velocities are assumed to be constant;
- Sections 4.3.2 and 4.3.4 only use the analytical approach since diffraction is considered. Therefore, only the second form of numerical integration can be used, which, in this case, is equivalent to the analytical approach because constant velocities are assumed;
- Section 4.3.5 gets rid of the assumption of constant velocities and compares the two numerical integration approaches.

4.3.1 Reflection on a single plane

A single plane, fixed, whose equation is $\Pi : 2x - y + 2z = 2$, is first considered. The transmitter is located in (-1, 1, 0.5)^T and has a velocity given by (0.3, 0, -0.4)^T. The receiver is in (0.5, 0.2, -1.2)^T and moves with a velocity (-0.1, 0.2, -0.5)^T. This geometry is depicted in Figure 4.8a, along with the trajectories of TX and RX (blue points), and the corresponding reflection points (red points). The plane Π is in green. The label TX (resp. RX) is located next to the initial position of the transmitter (resp. receiver). Since constant velocities are assumed, TX and RX are moving in straight line. However, it is not the case for the reflection points, whose trajectory is a curve. This is a direct consequence of the time-varying velocity of the reflection points given by (4.12).

The metric used to compare the different approaches is the distance error Δd between the reflection point positions computed using RT at each instant and the ones obtained by DRT (either by numerical integration or from the analytical approach), i.e.

$$\Delta d(t) = \sqrt{\left(x_{IX}^{RT} - x_{IX}^{DRT}\right)^2 + \left(y_{IX}^{RT} - y_{IX}^{DRT}\right)^2 + \left(z_{IX}^{RT} - z_{IX}^{DRT}\right)^2}, \tag{4.31}$$

where the time dependency of IX positions is implicit.

The evolution of this distance is given in Figure 4.8b. This leads to several comments:

- the analytical approach exhibits infinite accuracy, the distance error only originates from numerical errors (10^{-16} being the numerical precision);

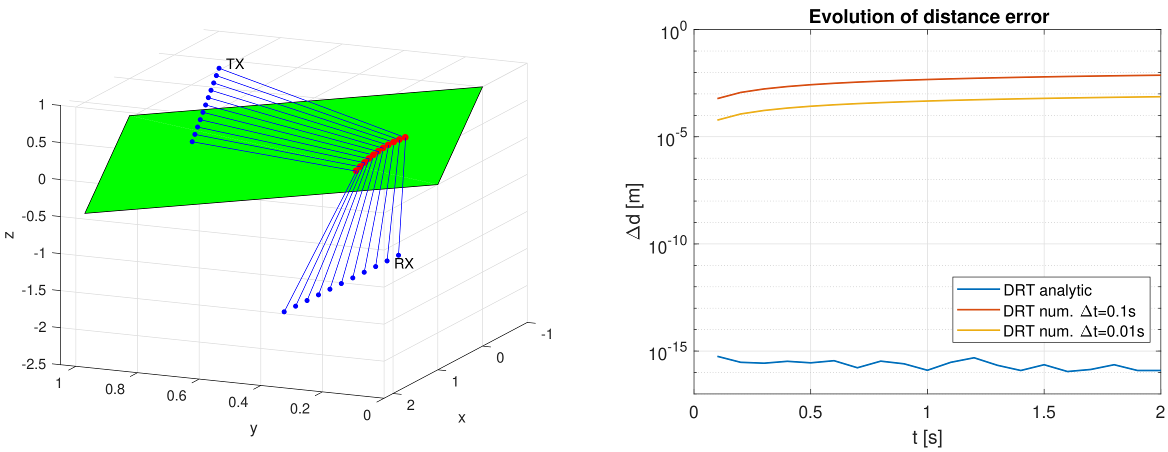

(a) Geometry (b) Evolution of distance error

Figure 4.8: Reflection on a single plane

- the numerical integration has an increasing error along with time, since errors propagate throughout the computations;
- reducing the time step improves the accuracy of the numerical integration but increases the computation time.

This demonstrates that tracking is indeed possible when considering one plane. Moreover, the analytical approach should always be preferred (if possible, i.e. when the velocities of any body of the geometry are not time-varying).

4.3.2 Diffraction on a single edge

The implementation of the diffraction in 3D is verified on a single edge, whose extremities are located in $(1, 0, 4)^T$ and $(1, 2, 2)^T$. The edge is fixed, and the transmitter and receiver are moving with constant velocities. The transmitter is initially located in $(0, -2, -4)^T$ and moves with a velocity $(1, 0.5, 0)^T$, whereas the receiver is initially in $(0, 0, 2)^T$ and has a velocity $(0, 2, 2)^T$. The evolution of the geometry is given in Figure 4.9, with the edge being the black line segment and the diffraction points being the red dots. Again, the labels of TX and RX are located next to their initial positions.

Comparison between RT and DRT computation of the diffraction points is also made using the distance error metric defined in equation (4.31). Simulations are performed every 0.1 s, up to 2 seconds, using the analytical DRT approach. The measured average distance error is 3.22×10^{-16} meter, with a maximum value of 3.22×10^{-16} m. The error is thus very close to the numerical precision, validating the analytical approach for diffraction. Moreover, this is the only relevant approach in this case since the numerical integration for diffraction falls back to the analytical approach when considering constant velocities.

4.3.3 Multiple reflections

UCLouvain RT software has been used with the maximal number of interactions set to three. Furthermore, only reflections are considered so far. The studied configuration, along with the

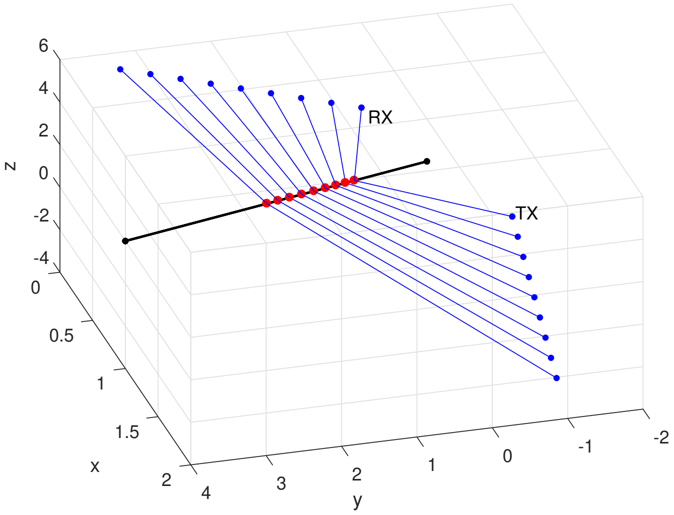

Figure 4.9: Geometry for diffraction on a single edge

rays identified at initialisation, is depicted in Figure 4.10. The transmitter is given a velocity $(0.1, -0.2, 0)^T$, and the receiver $(0, 0.5, 0)^T$. The bodies in the environment are also moving, having for velocities $\boldsymbol{v}_1 = (1, 1, 0)^T$, $\boldsymbol{v}_2 = (0, -0.5, 0)^T$ and $\boldsymbol{v}_3 = (0, 0, 1)^T$.

Based on this initial configuration, the DRT approach is used to characterize the rays geometry every $\Delta t = 0.1$ s, to a time horizon of 3 seconds. Results are compared with the ones obtained by RT simulations at these instants, in terms of total distance traveled by each ray, as given in Figure 4.11a. In this figure, from the bottom to the top, one can identify the LOS ray, the ray with one reflection on the ground, the two rays being reflected by the second body, and finally the triple reflection. Some of the rays also disappear, when one of their reflection points is found to be outside the body and cannot exist anymore (see for example the ray with a triple reflection, starting at 85 meters in $t = 0$ s, and disappearing at $t = 1.5$ seconds). Moreover, there seems to be a total agreement between the distances computed based on RT simulations and the ones from the DRT approach since the points are superimposed. This agreement is quantified using the mean of the absolute distance errors on all rays, i.e.

$$\epsilon_d(t) = \frac{1}{N_{\text{ray}}} \sum_{n=1}^{N_{\text{ray}}} \left| d_n^{RT}(t) - d_n^{DRT}(t) \right|, \tag{4.32}$$

which is depicted in Figure 4.11b. N_{ray} is the total number of rays (which also depends on time), d_n^{RT} (resp. d_n^{DRT}) is the total distance of ray n computed from RT simulations (resp. from DRT simulations).

First, the error propagation mechanism for the numerical integration approach is observed again (in Figure 4.11b). However, most of the error is coming from the rays having a reflection on the second body, as the error drops drastically when these rays are suppressed. In fact, the error is related to the ray having a reflection on the ground and at the bottom of the second body. Because they are (3D) reflections, the interaction point velocities are not constant (as stated in Section 4.1.1.1). Therefore, considering them constant during a small time interval in the numerical approach leads to errors. On the contrary, in this particular case, equation

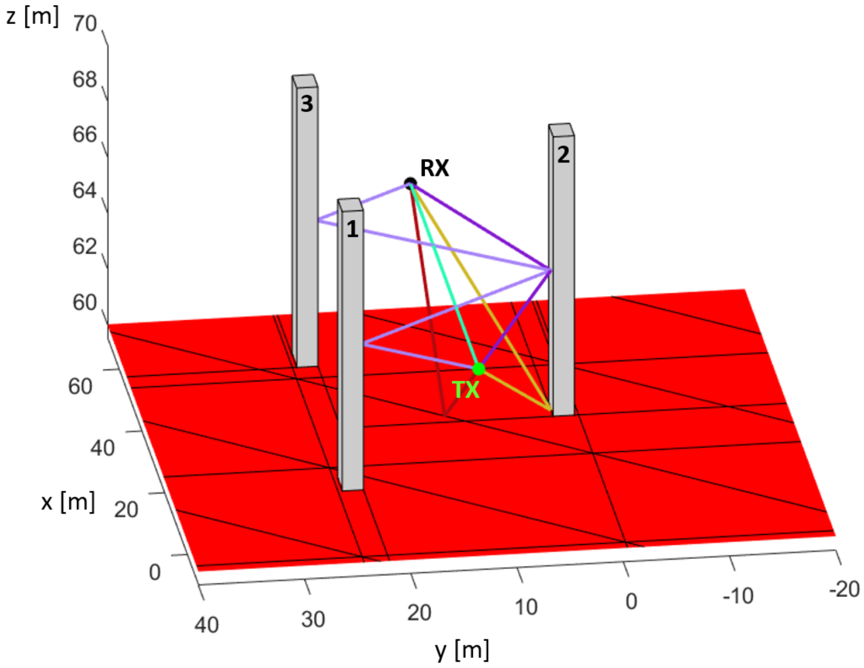

Figure 4.10: Multiple reflections: rays at initialisation - *the ground is depicted in red, black lines highlighting the mesh used in the RT software*

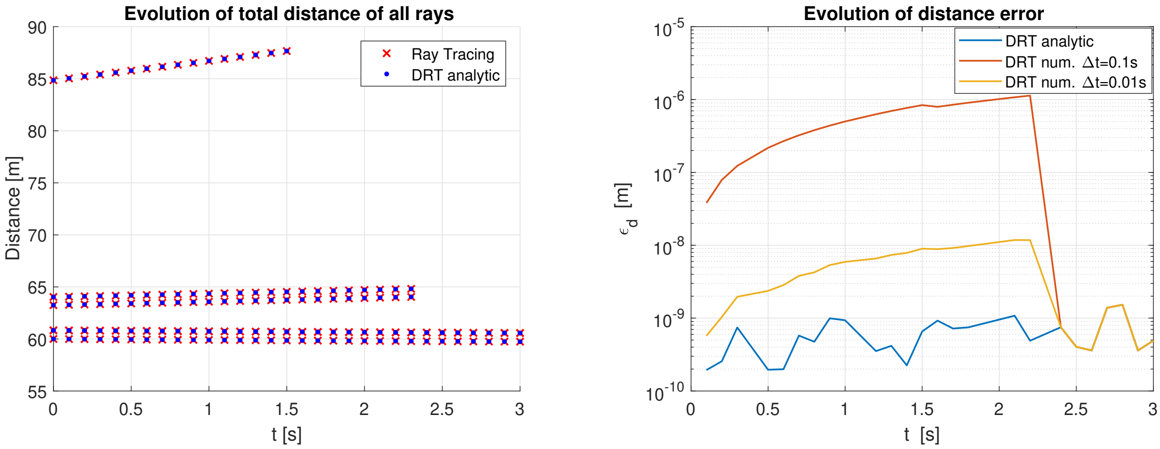

(a) Evolution of total distance of all rays

(b) Evolution of distance error

Figure 4.11: Multiple reflections: results

(4.12) leads to constant velocities for the interaction point of the ground reflection. Since only the LOS and the ground reflection remain at the end of the simulation, this explains why results are superimposed with the analytical approach.

Then, the best achievable accuracy is obtained thanks to the analytical approach and is close to the nanometer. Results are not as good as in the case of a single plane, owing to the tolerance level set in the RT software (10^{-10} meter). This tolerance level is used to determine if a point belongs to a surface or if some rays can be merged. Nevertheless, this nanometer accuracy is, on average, the ground level for all rays. Indeed, even when some rays are suppressed, the accuracy remains close to the nanometer with the analytical approach. Please note that in this example, some rays are suppressed but no rays are created.

The computation times for the different approaches are detailed in Table 4.1. These numbers exclude the extra 10 seconds corresponding to the time of the first RT iteration performed to feed the DRT algorithm.

As mentioned previously, reducing the timestep Δt for the numerical integration increases the computation time (see Table 4.1), while improving the accuracy (see Figure 4.11b). Again, the DRT analytic approach should be preferred in terms of computation time and accuracy.

In Table 4.1, the computation time of the RT simulations (performed at each instant) is given for information. It should not be directly compared to the other computation times. Indeed, RT simulations involve other computations not implemented in the DRT approach at this stage, such as the computation of diffraction rays and their associated electric field quantities. This will be further discussed in Section 6.2.

Ray Tracing	DRT numerical		DRT analytic
	$\Delta t = 0.1s$	$\Delta t = 0.01s$	
263.1 s	1.96 s	16.76 s	1.80 s

Table 4.1: Computation time, excluding the first ray tracing iteration (for geometry with multiple reflections)

4.3.4 Multiple reflections with diffraction

The same geometry as the one given in Section 4.3.3 is considered, with the same initial positions and velocities for all the environment. Now, diffraction rays are added, leading to more than 20 rays at initialisation (see Figure 4.12, where diffraction rays are depicted with dashed lines).

The evolution of the total distance error (defined in equation (4.32)) for all rays (reflected and diffracted) is monitored. Only the analytical approach is used in this case. As already observed previously when considering only reflections, the accuracy (on all rays) is close to the nanometer. Indeed, the average value of ϵ_d is 5.51×10^{-10} m, whereas the maximum observed value is 8.97×10^{-10} meter.

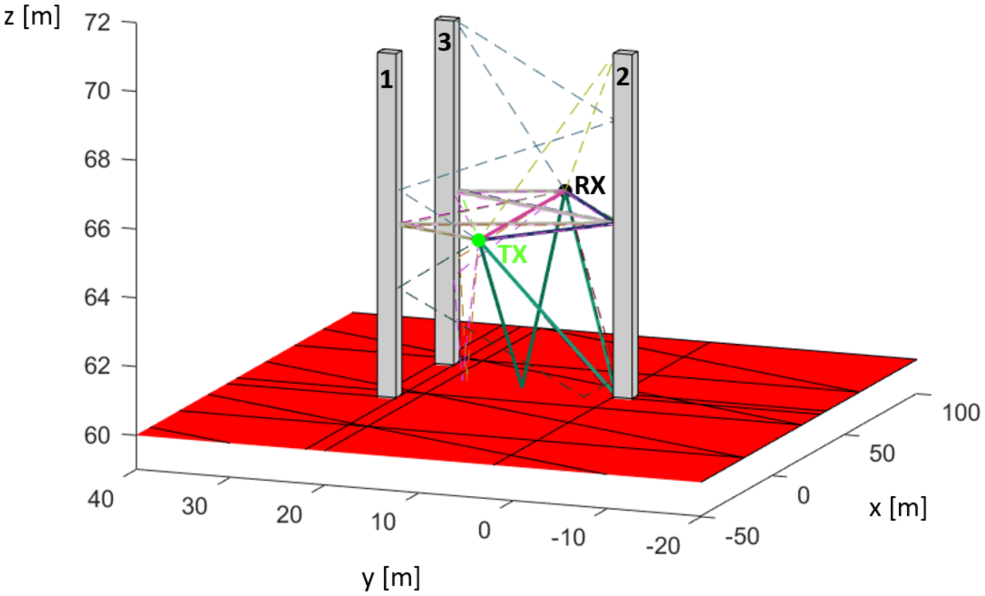

Figure 4.12: Multiple reflections with diffraction: rays at initialisation - *diffraction rays are in dashed lines*

4.3.5 Reflection on a single plane with time-varying velocities

The same plane as the one used in Section 4.3.1 is considered, with the same initial positions for the transmitter and the receiver. However, these latter now have time-varying velocities. The evolution of the distance error metric $\Delta d(t)$, given in (4.31), is monitored and computed for both numerical integration approaches: the closed-form, given in Section 4.2.1.1, and the analytical substitution from Section 4.2.1.2.

For example, instead of having a constant velocity, the receiver can have a constant acceleration, meaning that its velocity is now linearly varying with time. Results for a fixed plane, a transmitter moving with a constant velocity $(0.3,\ 0,\ -0.4)^T$ and a receiver with a velocity $(-0.2\,t,\ 0.2,\ -1.5\,t)^T$ are given in Figure 4.13 (in red, method from Section 4.2.1.1, and in blue, from Section 4.2.1.2).

First, the accuracy improvement obtained by reducing the timestep Δt is clearly noticeable for both approaches, as it enables a gain of roughly two orders of magnitude. Then, regarding the comparison itself of the two approaches, the numerical integration with analytical substitution achieves an accuracy which is close to one order of magnitude below the one obtained by the closed-form numerical approach. Since their computational costs are quite similar, it is therefore advisable to use the numerical integration with analytical substitution for this particular example.

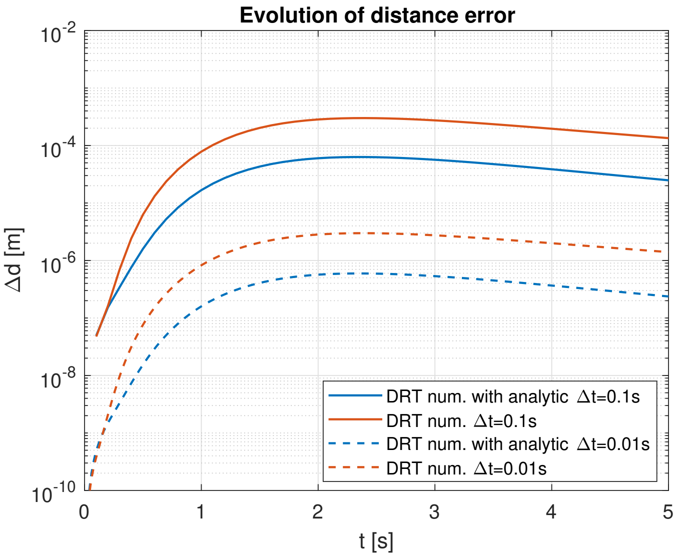

Figure 4.13: Evolution of distance error for a single reflection with time-varying velocities

A study of further examples showed that the numerical integration with analytical substitution seems to achieve a better accuracy most of the time, especially for more physical time dependencies of the velocities (constant, linear or quadratic dependencies). Furthermore, it was also found to be less sensitive to error propagation. On the contrary, the closed-form approach sometimes suffered from oscillations in the distance error and its poorer performance can be linked to equation (4.12), as it involves many terms and derivatives. Indeed, small errors on several terms add up and can badly impact the computed velocity of the reflection point, increasing the distance error.

A final remark regarding constant velocities: it is always better to use the numerical approach with analytical substitution since, in this particular case, it is equivalent to an analytical integration.

4.3.6 Conclusion of geometric validation

The various implementations of DRT have been validated and compared on small examples. From these examples, it appears that:

- The analytical approach offers a theoretically infinite accuracy for geometries with constant velocities. In practice, this infinite accuracy is limited by numerical precision (10^{-16}) or by the tolerance level (10^{-10}) set in RT simulations.

- Regarding the numerical integration, it is necessary for geometries where velocities are time-varying. Moreover, the analytical substitution, designed for diffraction and reflection, usually gives better accuracy for the same timestep Δt and should therefore be preferred.

Figure 4.14 summarizes the different DRT implementations studied and highlights their main characteristics. It also depicts the methods that were proven to give the best results (blue ellipses):

- Analytical approach for geometries with constant velocities;

- Numerical integration suited for diffraction and reflection, i.e. with analytical substitution, for geometries with time-varying velocities.

In conclusion, the main contribution of this chapter is the new DRT approach. Several implementations as well as a geometric validation have been presented, showing that a high-accuracy tracking of reflection and diffraction points is possible. Furthermore, suppression of rays has been handled. However, the creation of new rays has not been studied and will be at the heart of the following chapters. Indeed, one can expect new rays to be created because of the evolution of the geometry. These new rays will not be identified by the DRT algorithm, since they were not found by the RT simulation used for the initialisation of DRT. For this, channel (and not geometric) quantities will be needed.

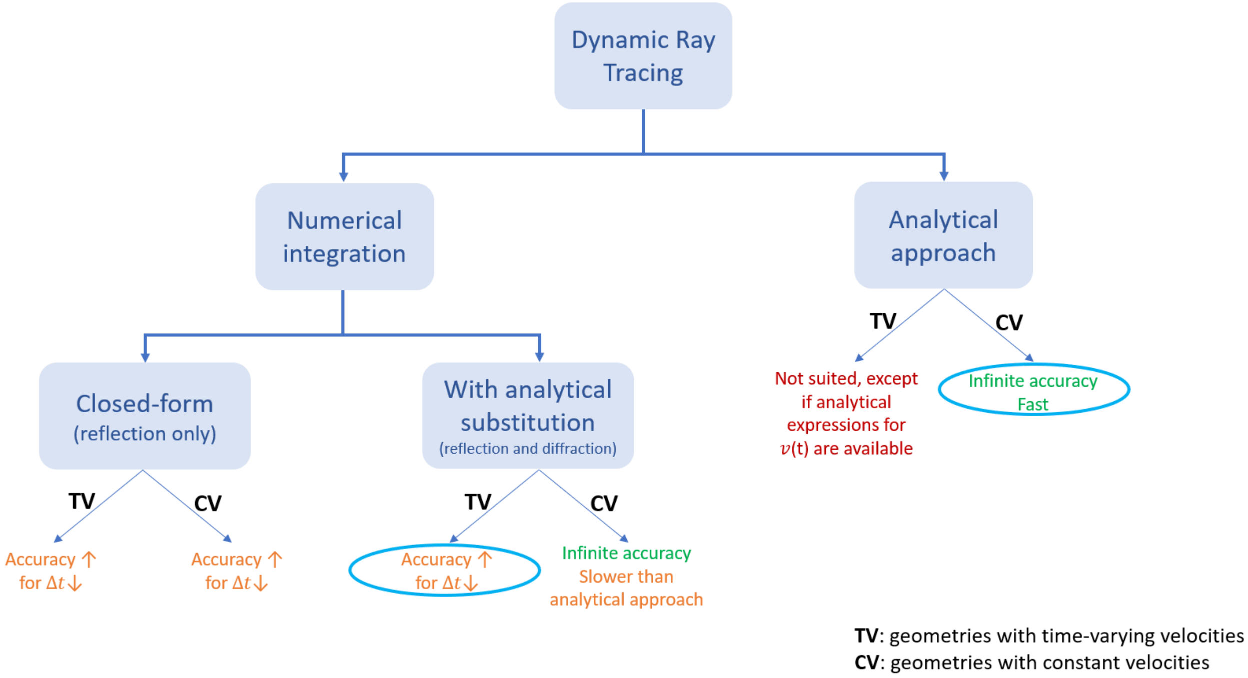

Figure 4.14: Summary of all DRT methods considered

Chapter 5

From rays to channel quantities

The goal of the following chapters of this work is to compare the results obtained by RT and DRT at the channel level. To do so, one last step should be added to the DRT algorithm: reconstruction of the ray quantities (see the ones given in Table 3.1) from the ray geometry obtained by DRT. This actually corresponds to the last step of a classical RT algorithm, that uses the theory given in Chapter 3. Therefore, this step is actually duplicated and part of the RT and DRT approaches. At its end, the DRT algorithm also returns a ray cell, for each identified DRT ray.

From this ray cell, metrics or quantities at the channel level can be obtained and used to compare the RT and DRT approaches at a higher level (and not only geometrically as it was done in Chapter 4). It also enables to study the impact of the forgotten rays and help to define what is actually a "*good knowledge*" of the channel.

In a first step, the importance of considering a receiving antenna to obtain the channel impulse response (CIR) is detailed. Then, from this CIR, delay-based, angular-based and other channel quantities are derived and applied to a simple example that involves the creation of new rays. Finally, a conclusion is drawn about all the studied metrics and the ones that will be useful for the next chapters.

The geometry of the example considered in this chapter is given in Figure 5.1. The transmitter is located in $(-25, 10, 5)^T$ and the receiver is in $(25, 10, 5)^T$. Both are kept fixed. The ground level is at $z = 0$ m, and there is only one moving body (of a height of 10 meters) in the environment. The body is initially located 10 meters away from the transmitter in the y-direction and is only moving towards the receiver in the x-direction, i.e. its velocity vector is $(20, 0, 0)^T$. After 3 seconds, the body is now located next to the receiver (symmetric situation w.r.t. the initial configuration) and the simulation is completed. *Analytical DRT* is performed every 0.02 second, always based on the RT simulation at time $t = 0$ s. For the comparison, RT simulations are performed every 0.1 s. The chosen carrier frequency is 1.8 GHz, and the effective relative permittivity (of the ground and the body) is set to $\epsilon_r^{eff} = 4.44 - j\,0.001$ [31,55].

Such a geometry has been chosen since it involves the creation of new reflection rays approximately in the middle of the simulation time, when the body is at equal distance of TX and RX. Therefore, all considered metrics will be relevant if the creation of new rays can be clearly identified on this simple example.

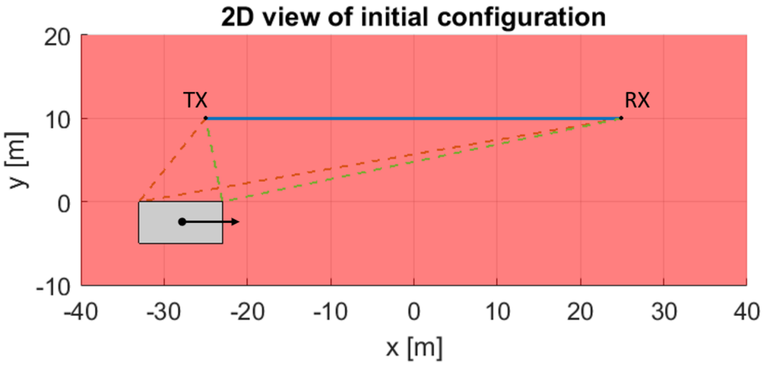

(a) Rays at initialisation

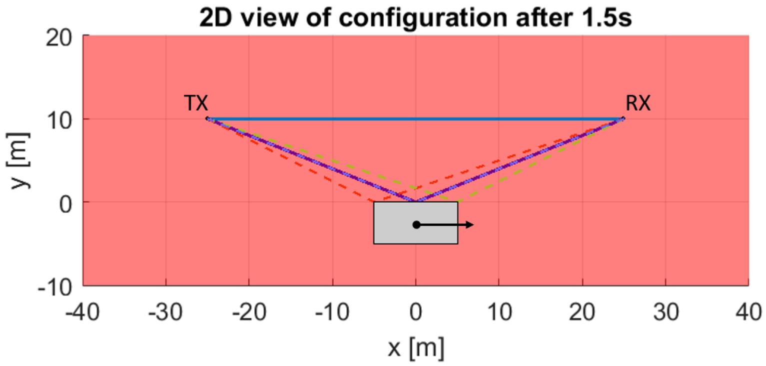

(b) Rays after 1.5 seconds, with a new reflection ray on the body

Figure 5.1: Geometry and rays configuration for example with one moving body *(diffraction rays are in dashed lines)*

5.1 Channel impulse response

Starting from the electric field vector given in the ray-frame $(\hat{\boldsymbol{s}}, \hat{\boldsymbol{\phi}}, \hat{\boldsymbol{\theta}})$ in the *ray cell* (see Table 3.1), one needs to take into account the radiation pattern of the receiving antenna to get the CIR. Indeed, the received electric field $\boldsymbol{E} = E_\phi\, \hat{\boldsymbol{\phi}} + E_\theta\, \hat{\boldsymbol{\theta}}$ coming from one ray k is projected on the RX antenna radiation pattern in order to get the scalar quantity α_k measured at the antenna[6]:

$$\alpha_k \;=\; \boldsymbol{f}_{RX}^{*} \cdot \boldsymbol{E} \;=\; \begin{bmatrix} f_{RX,\phi}(\phi_{RX}, \theta_{RX}) & f_{RX,\theta}(\phi_{RX}, \theta_{RX}) \end{bmatrix}^{*} \begin{bmatrix} E_\phi \\ E_\theta \end{bmatrix}, \tag{5.1}$$

with $\boldsymbol{f}_{RX}$ being the radiation pattern (in field) of the receiving antenna. Subscript k is implicit in all quantities related to ray k and coming from the same *ray cell*, i.e. in the electric field values but also in the azimuth and elevation angles of arrival ϕ_{RX} and θ_{RX}. Moreover, since dynamic environments are considered, these quantities are also time-varying and $\boldsymbol{\alpha_k}$ **implicitely depends on time**. All in all, the CIR in the time, delay and space domains is

---

[6] Since phasor quantities are considered, the quantity α_k is complex and to obtain what is physically measured at the RX antenna, the harmonic time-variation must be made explicit by multiplying by $e^{j\omega_c t}$ and taking the real part ($\omega_c = 2\pi f_c$, with f_c being the carrier frequency).

given by

$$h\left(t,\tau,\boldsymbol{\Omega}_{TX},\boldsymbol{\Omega}_{RX}\right) = \sum_{k=1}^{N(t)} \alpha_k \;\delta(\tau-\tau_k)\,\delta(\boldsymbol{\Omega}_{TX}-\boldsymbol{\Omega}_{TX,k})\,\delta(\boldsymbol{\Omega}_{RX}-\boldsymbol{\Omega}_{RX,k}), \tag{5.2}$$

where:

- τ_k is the delay associated with ray k computed thanks to $\tau_k = \frac{d_k}{c}$, with d_k the total distance traveled by the ray and c the speed of light;
- $\boldsymbol{\Omega}_{TX} = [\cos(\phi_{TX})\sin(\theta_{TX}),\ \sin(\phi_{TX})\sin(\theta_{TX}),\ \cos(\theta_{TX})]^T$ is the direction vector of departure of the ray that gathers the azimuth and elevation angles of departure (ϕ_{TX} and θ_{TX}). $\boldsymbol{\Omega}_{TX,k}$ is this vector evaluated at the azimuth and elevation angles of departure of ray k. Similarly, $\boldsymbol{\Omega}_{RX}$ is defined as the direction vector of arrival of the ray, gathering the azimuth and elevation angles of arrival (ϕ_{RX} and θ_{RX});
- $\delta(x)$ is the Dirac delta function, used to denote that the contribution of a given ray in the delay and space domains only arises at the delays and arrival/departure angles associated with this ray;
- $N(t)$ is the number of rays and is a function of the time. Indeed, rays can be created or suppressed due to the dynamic evolution of the channel.

Since RT (or DRT) simulations are only performed at discrete instants t_j, the CIR is only known at these instants, meaning that one does not have access to $h\left(t,\tau,\boldsymbol{\Omega}_{TX},\boldsymbol{\Omega}_{RX}\right)$ but rather to $h\left(t_j,\tau,\boldsymbol{\Omega}_{TX},\boldsymbol{\Omega}_{RX}\right)$. The number of rays at time t_j is denoted $N(t_j) := N_j$.

5.1.1 Radiation pattern of a dipole antenna

To be able to compute the coefficient α_k from equation (5.1), the radiation pattern of the RX antenna must be known. This antenna is assumed to be an ideal dipole of length l, whose radiation pattern is given by [56]

$$\begin{cases} f_\theta(\phi,\theta) &= \frac{\cos(kl\cos(\theta/2))-\cos(kl/2)}{\sin(\theta)} \\ f_\phi(\phi,\theta) &= 0 \end{cases}, \tag{5.3}$$

where f_θ and f_ϕ represent the θ- and ϕ-components of the radiation pattern that are evaluated at the angles of arrival (resp. departure if the antenna is at TX) of the coming (resp. leaving) rays, whereas $k = \frac{2\pi}{\lambda}$ is the wavenumber. Since $f_\phi(\phi,\theta) = 0$ whatever the angles, no component of the electric field in the azimuth direction can be measured by the antenna.

5.2 Delay-based quantities

Integration of equation (5.2) over the angular domains ($\boldsymbol{\Omega}_{TX}$ and $\boldsymbol{\Omega}_{RX}$) enables to obtain a two-dimensional CIR, depending only on the time t and the delay τ. At time t_j, this bidimensional CIR is given by

$$h(t_j,\tau) = \int_{\boldsymbol{\Omega}_{TX}}\int_{\boldsymbol{\Omega}_{RX}} h(t_j,\tau,\boldsymbol{\Omega}_{TX},\boldsymbol{\Omega}_{RX})\,d\boldsymbol{\Omega}_{TX}\,d\boldsymbol{\Omega}_{RX} = \sum_{k=1}^{N_j} \alpha_k \;\delta(\tau-\tau_k), \tag{5.4}$$

where the property of the integration of a delta function over its domain has been used, i.e. $\int_{-\infty}^{+\infty} \delta(x)\, dx = 1$.

The instantaneous power delay profile (at time t_j) is then given by

$$P(t_j, \tau) \;=\; |h(t_j, \tau)|^2 \;=\; \sum_{k=1}^{N_j} |\alpha_k|^2 \;\delta(\tau - \tau_k), \tag{5.5}$$

while the average power delay profile over the discrete time instants $t_j \in \{t_0, t_1, t_2, ..., t_{J-1}\}$ has for expression:

$$P(\tau) \;=\; \frac{1}{J} \sum_{j=0}^{J-1} P(t_j, \tau) \;=\; \frac{1}{J} \sum_{j=0}^{J-1} \sum_{k=1}^{N_j} |\alpha_k|^2 \;\delta(\tau - \tau_k). \tag{5.6}$$

However, averaging over all simulations time instants is not considered useful in our case. Indeed, the goal of the studied metrics is to be able to identify dynamic evolution of quantities and not their mean values.

5.2.1 Delay spread

Starting from the expression (5.5) of the instantaneous power delay profile, the instantaneous mean delay is obtained thanks to

$$\tau_M(t_j) \;=\; \frac{\int_0^{+\infty} \tau P(t_j, \tau)\, d\tau}{\int_0^{+\infty} P(t_j, \tau)\, d\tau} \;=\; \frac{\sum_{k=1}^{N_j} |\alpha_k|^2 \; \tau_k}{\sum_{k=1}^{N_j} |\alpha_k|^2}. \tag{5.7}$$

Regarding the instantaneous RMS delay spread, it is obtained with

$$\tau_{RMS}(t_j) \;=\; \sqrt{\frac{\int_0^{+\infty} (\tau - \tau_M(t_j))^2\, P(t_j, \tau)\, d\tau}{\int_0^{+\infty} P(t_j, \tau)\, d\tau}} \;=\; \sqrt{\frac{\sum_{k=1}^{N_j} |\alpha_k|^2 (\tau_k - \tau_M(t_j))^2}{\sum_{k=1}^{N_j} |\alpha_k|^2}}, \tag{5.8}$$

which is equivalent to the expression given in [57]:

$$\tau_{RMS}(t_j) \;=\; \sqrt{\frac{\sum_{k=1}^{N_j} |\alpha_k|^2 \, \tau_k^2}{\sum_{k=1}^{N_j} |\alpha_k|^2} \;-\; \left(\frac{\sum_{k=1}^{N_j} |\alpha_k|^2 \, \tau_k}{\sum_{k=1}^{N_j} |\alpha_k|^2}\right)^2}. \tag{5.9}$$

The evolution of the mean delay and RMS delay spread for the example considered in this chapter are given in Figure 5.2. As expected from the example, the apparition of the new reflection rays is clearly noticeable, between 1.25 and 1.75 seconds of simulation time. Indeed, dots correspond to the values obtained by performing a RT simulation at these instants, considering or neglecting diffraction rays, whereas blue lines correspond to the results obtained using the DRT approach. Results are superimposed except when the new reflection rays appear, since they are not present in the DRT approach, leading to an underestimation of the delay spread at these instants. One can also clearly see the impact of the diffraction rays on the RMS delay spread, especially when their relative power increases. This latter depends on the diffraction coefficients which themselves depend on the angles of the geometry of the diffracted rays.

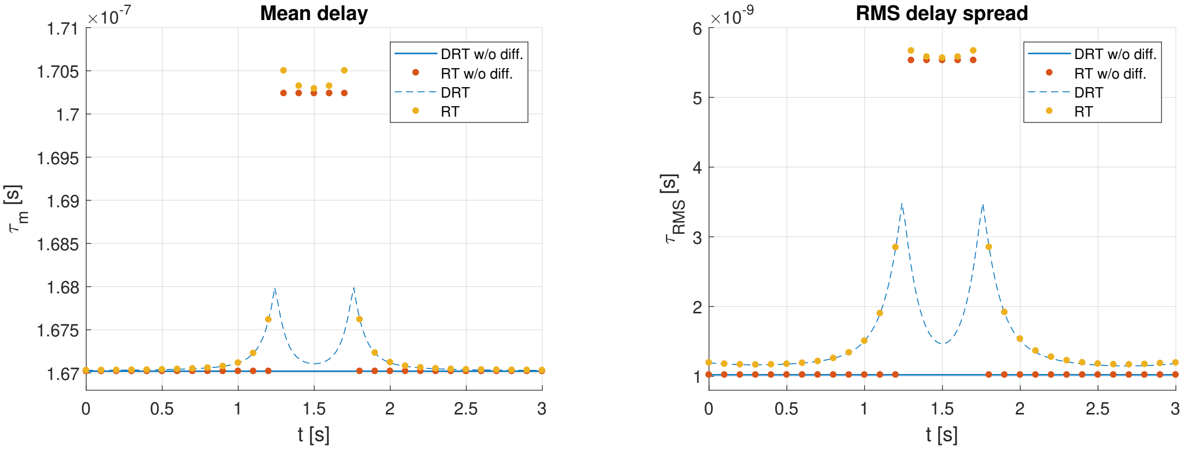

Figure 5.2: Mean delay and RMS delay spread for example of Chapter 5

5.2.2 Spectral divergence

The instantaneous RMS delay spread is a channel-based quantity since it is independent of the system parameters such as the bandwidth. To take into account the bandwidth, one must remember that, in practice, the CIR is convoluted with the pulse shaping at TX and the matched filter at RX. Usually, the convolution between the pulse shaping and the matched filter is a raised-cosine filter, so that the Nyquist criterion is fulfilled and intersymbol interference (ISI) is avoided. The expression of such a filter $u(\tau)$ is

$$u(\tau) \;=\; \frac{1}{T}\,\mathrm{sinc}\left(\frac{\tau}{T}\right)\,\frac{\cos\left(\frac{\pi\alpha\tau}{T}\right)}{1-\left(\frac{2\alpha\tau}{T}\right)^2}, \tag{5.10}$$

where the normalized sinc function is used, i.e. $\mathrm{sinc}(x) = \frac{\sin(\pi x)}{\pi x}$, T is the symbol period ($T = (1+\alpha)/(2B)$, B being the bandwidth in Hz), and α is the roll-off factor ($\alpha \in [0,1]$). The total impulse response of the channel with the pulse shaping and the matched filter is now

$$\tilde{h}(t_j,\tau) \;=\; h(t_j,\tau) * u(\tau) \;=\; \sum_{k=1}^{N_j} \alpha_k\, u(\tau-\tau_k). \tag{5.11}$$

Taking the power:

$$P_s(t_j,\tau) \;=\; \left|\tilde{h}(t_j,\tau)\right|^2 \;=\; \sum_{k=1}^{N_j} |\alpha_k|^2\; u^2(\tau-\tau_k). \tag{5.12}$$

Doing so with the CIRs obtained at time t_j using either RT or DRT, one gets two continuous functions of the delay τ, denoted $P_s^{RT}(t_j,\tau)$ and $P_s^{DRT}(t_j,\tau)$. In order to compare these two functions and get rid of the delay-dependency (i.e. to obtain only one scalar value for a given t_j), a measure of distance based on the Kullback-Leibler divergence is used. Indeed, the Kullback-Leibler divergence is useful to compare probability distributions and can be used as a metric with some modifications to make it symmetric, non-negative (with an equality to zero only if the two functions are the same) and obeying the triangular inequality [58]. In our case, the considered functions are not truly probability distributions (since they are not normalized to one) but they are non-negative and therefore the divergence remains well-defined.

Furthermore, numerically one can only have access to sampled versions of $P_s^{RT}(t_j,\tau)$ and $P_s^{DRT}(t_j,\tau)$ over the delay domain, meaning that these are only known at the delay-instants $\tau_n \in \{\tau_0,\tau_1...,\tau_{N-1}\}$. Based on these observations, the proposed metric is finally (inspired from [59]):

$$D(t_j) \;=\; \log\left(\frac{1}{N^2}\left[\sum_{n=0}^{N-1}\frac{P_s^{RT}(t_j,\tau_n)}{P_s^{DRT}(t_j,\tau_n)}\right]\left[\sum_{n=0}^{N-1}\frac{P_s^{DRT}(t_j,\tau_n)}{P_s^{RT}(t_j,\tau_n)}\right]\right). \tag{5.13}$$

This metric $D(t_j)$ is named the *instantaneous spectral divergence* at time t_j [59]. Expression (5.13) is symmetric in $P_s^{RT}(t_j,\tau)$ and $P_s^{DRT}(t_j,\tau)$, as well as independent of scaling factors between these two quantities. Only the shape of the two functions is compared, and if the shape is similar, the spectral divergence tends to zero. The absolute level of the metric is quite arbitrary as any basis for the logarithm can be taken, leading to the multiplication of $D(t_j)$ by a constant value. In this work, the natural logarithm is chosen.

Study of the bandwidth parameter B The study of the bandwidth B on the spectral divergence value has been performed on this chapter's example. Only B is varying, leading to a variation of the symbol period, while other parameters are kept fixed. The roll-off factor α is set to 0.5, the sampling frequency for the delay τ_n is chosen to be 10 GHz. Moreover, an artificial (white) noise level is added in the computed power delay profiles $P_s^{RT}(t_j,\tau)$ and $P_s^{DRT}(t_j,\tau)$ in order to avoid division by zero in (5.13) at instants where nothing is received. To limit its impact on the metric, the power level of this noise is set to one order of magnitude below the power of the weakest diffraction ray.

The evolution of the spectral divergence is given in Figure 5.3 for several bandwidth values. The impact of the new rays (around 1.5 seconds) is visible for any bandwidth but is more important for a bandwidth of 100 MHz. In order to explain this result, one must look at both power delay profiles ($P_s^{RT}(t_j,\tau)$ and $P_s^{DRT}(t_j,\tau)$) at a time where there are new rays (say $t_j = 1.5$ s). This is given in Figure 5.4, depicting the power profiles coming from the reflection rays only. The discrete rays are given in green (i.e. corresponding to $P(t_j,\tau)$), whereas other curves consider the convolution with the raised-cosine at different bandwidths, i.e. $P_s(t_j,\tau)$. The left graph gives the RT results, whereas the DRT results are depicted on the right graph. One can then identify the new reflection rays, only present in the RT power profile, that have a delay close to 180 ns.

For small bandwidth values (1 MHz and 10 MHz), all rays fall into the same channel tap, impacting its amplitude but affecting slightly its shape. Since the spectral divergence metric is sensitive to the shape difference between both profiles, its value remains small. However, for a bandwidth of 100 MHz, two taps start to appear and are a bit merged (yellow curves in Figure 5.4). This drastically modifies the shape of the power profiles, explaining why the spectral divergence is quite high for this bandwidth value. Increasing more the bandwidth (e.g. 1 GHz) enables a clearer identification of the channel taps, whose effect is then very located. Therefore, the difference between both profiles is important but only on a small delay interval, hence the spectral divergence is not that much impacted, i.e. it will be more difficult to use it to deduce that new rays have been created.

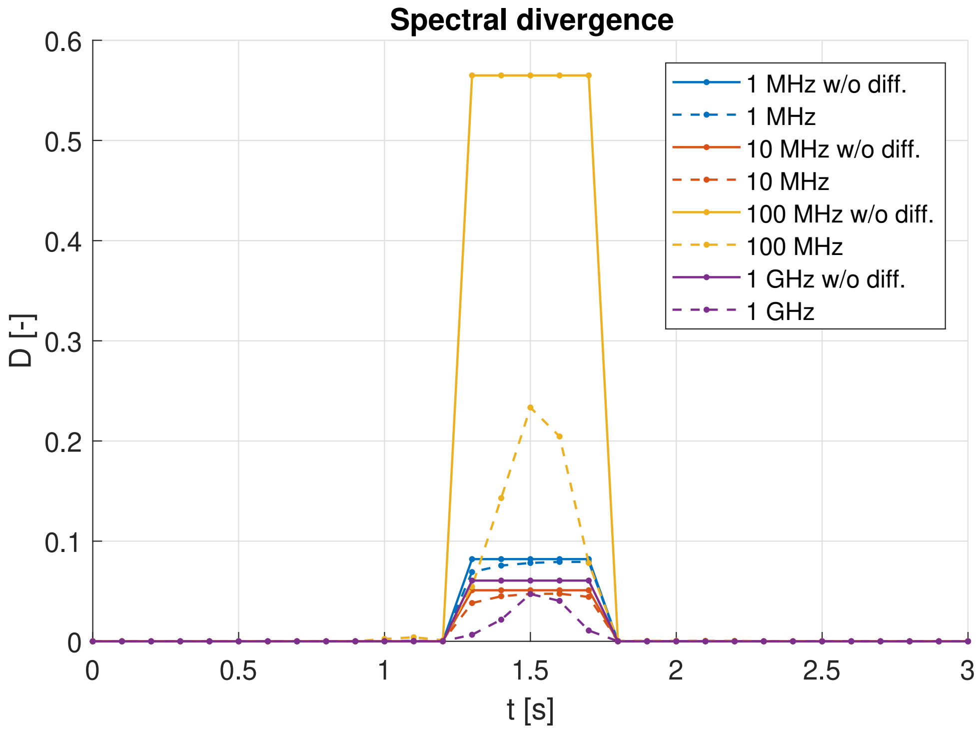

Figure 5.3: Evolution of spectral divergence for example of Chapter 5

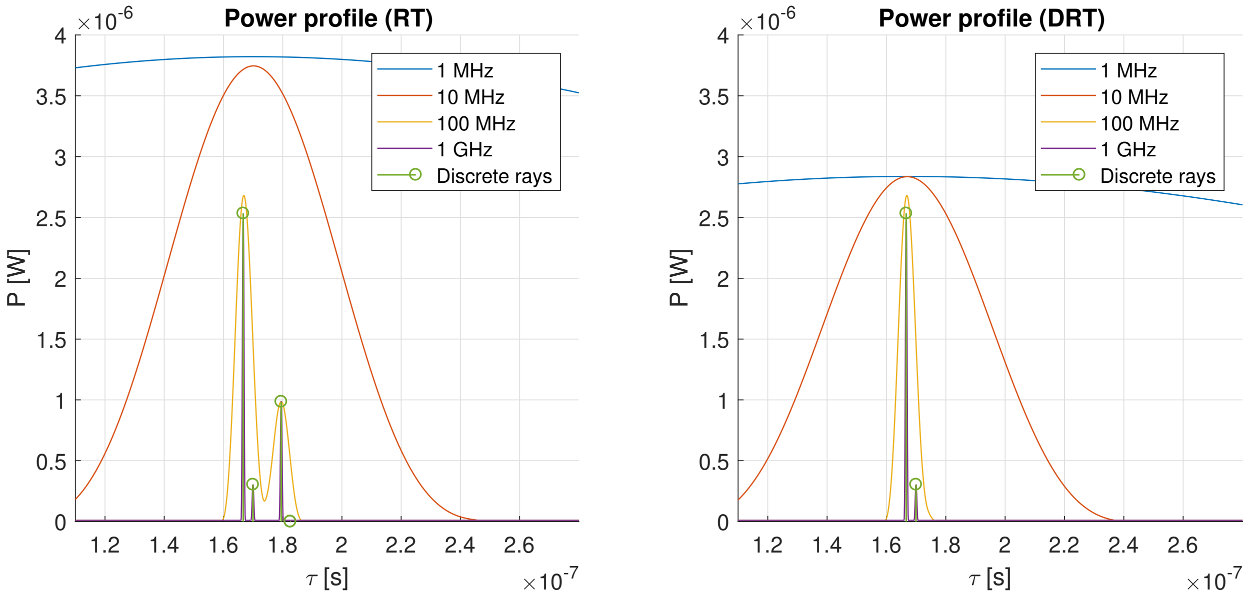

Figure 5.4: Power profile at time $t = 1.5$ seconds (reflection rays only)

Furthermore, considering diffraction rays reduces the spectral divergence value (see dashed lines in Figure 5.3). Again, this can be explained by directly looking at the power delay profiles (not represented here), where one will see that the contribution of some extra diffraction rays is to add power around the delay value of 180 ns. Therefore, the second channel tap (at 100 MHz) starts to appear also in the DRT profile and the global shapes of both power delay profiles are more similar, decreasing the value of the spectral divergence.

In summary, in order to maximize the effect of new rays on the spectral divergence, one must use a bandwidth whose associated symbol period has the same order of magnitude than the difference of delays between the rays, the intuition behind this observation being the appearance of channel taps that are not totally separated. In the given example, the delay difference between the two main reflection rays (see the two rays with a power higher than 10^{-6} W in the left part of Figure 5.4) is close to 13 ns (meaning that the difference of traveled distance is about 3.9 meters), which is roughly the symbol period associated with a bandwidth of 100 MHz.

5.3 Angular-based quantities

In a similar way to what has been done for the delay-based quantities, equation (5.2) is now integrated over the delay-domain. Moreover, integration on either the departure or the arrival angles is also achieved, leading to several instantaneous direction power spectra. More precisely, one has:

- the instantaneous joint direction power spectrum $A(t_j, \mathbf{\Omega}_{TX}, \mathbf{\Omega}_{RX})$, defined as

$$A(t_j, \mathbf{\Omega}_{TX}, \mathbf{\Omega}_{RX}) = \left| \int_\tau h(t_j, \tau, \mathbf{\Omega}_{TX}, \mathbf{\Omega}_{RX})\, d\tau \right|^2 = \sum_{k=1}^{N_j} |\alpha_k|^2\, \delta(\mathbf{\Omega}_{TX} - \mathbf{\Omega}_{TX,k})\, \delta(\mathbf{\Omega}_{RX} - \mathbf{\Omega}_{RX,k}); \tag{5.14}$$

- the instantaneous transmit direction power spectrum $A_{TX}(t_j, \mathbf{\Omega}_{TX})$, given by

$$A_{TX}(t_j, \mathbf{\Omega}_{TX}) = \left| \int_\tau \int_{\mathbf{\Omega}_{RX}} h(t_j, \tau, \mathbf{\Omega}_{TX}, \mathbf{\Omega}_{RX})\, d\tau\, d\mathbf{\Omega}_{RX} \right|^2 = \sum_{k=1}^{N_j} |\alpha_k|^2\, \delta(\mathbf{\Omega}_{TX} - \mathbf{\Omega}_{TX,k}); \tag{5.15}$$

- the instantaneous receive direction power spectrum $A_{RX}(t_j, \mathbf{\Omega}_{RX})$, from

$$A_{RX}(t_j, \mathbf{\Omega}_{RX}) = \left| \int_\tau \int_{\mathbf{\Omega}_{TX}} h(t_j, \tau, \mathbf{\Omega}_{TX}, \mathbf{\Omega}_{RX})\, d\tau\, d\mathbf{\Omega}_{TX} \right|^2 = \sum_{k=1}^{N_j} |\alpha_k|^2\, \delta(\mathbf{\Omega}_{RX} - \mathbf{\Omega}_{RX,k}). \tag{5.16}$$

5.3.1 Angular spread

Only the receive direction, i.e. the arrival angles ϕ_{RX} and θ_{RX}, is considered here, but a similar development can be performed for the transmit direction. Moreover, working directly on ϕ_{RX} and θ_{RX} rather than on the direction vector $\mathbf{\Omega}_{RX}$ enables to get more insights about the geometry, as the azimuth and elevation directions are clearly separated. Hence, the instantaneous receive direction power spectra in which this dependency is made explicit are given by

$$A_{RX}(t_j, \phi_{RX}, \theta_{RX}) = \sum_{k=1}^{N_j} |\alpha_k|^2 \, \delta(\phi_{RX} - \phi_{RX,k}) \, \delta(\theta_{RX} - \theta_{RX,k}), \tag{5.17}$$

$$A_{RX}(t_j, \phi_{RX}) = \sum_{k=1}^{N_j} |\alpha_k|^2 \, \delta(\phi_{RX} - \phi_{RX,k}), \tag{5.18}$$

$$A_{RX}(t_j, \theta_{RX}) = \sum_{k=1}^{N_j} |\alpha_k|^2 \, \delta(\theta_{RX} - \theta_{RX,k}). \tag{5.19}$$

Using (5.18), the mean instantaneous azimuth angle $\phi_{RX,m}(t_j)$ and the instantaneous RMS angle spread $\phi_{RX,RMS}(t_j)$ for the RX azimuth angle are

$$\phi_{RX,m}(t_j) = \frac{\int_0^{2\pi} \phi_{RX} A_{RX}(t_j, \phi_{RX}) \, d\phi_{RX}}{\int_0^{2\pi} A_{RX}(t_j, \phi_{RX}) \, d\phi_{RX}} = \frac{\sum_{k=1}^{N_j} |\alpha_k|^2 \; \phi_{RX,k}}{\sum_{k=1}^{N_j} |\alpha_k|^2}, \tag{5.20}$$

$$\phi_{RX,RMS}(t_j) = \sqrt{\frac{\int_0^{2\pi} (\phi_{RX,k,m}(t_j))^2 \, A_{RX}(t_j, \phi_{RX}) \, d\phi_{RX}}{\int_0^{2\pi} A_{RX}(t_j, \phi_{RX}) \, d\phi_{RX}}} = \sqrt{\frac{\sum_{k=1}^{N_j} |\alpha_k|^2 \, (\phi_{RX,k,m}(t_j))^2}{\sum_{k=1}^{N_j} |\alpha_k|^2}}, \tag{5.21}$$

with

$$\phi_{RX,k,m}(t_j) = \mod (\phi_{RX,k} - \phi_{RX,m}(t_j) + \pi, 2\pi) - \pi, \tag{5.22}$$

to ensure that it remains between $[-\pi, \pi]$ [57]. Similarly, the instantaneous elevation mean angle $\theta_{RX,m}(t_j)$ and the instantaneous RMS elevation angle spread $\theta_{RX,RMS}(t_j)$ are computed.

Figure 5.5 regroups the mean and RMS angle spread for both elevation and azimuth angles at the receiver, for the example studied in this chapter. Again, differences between the RT and the DRT approaches appear due to the creation of the new reflection rays, and are clearly noticeable. Moreover, thanks to the independent study of the azimuth and elevation angles, one can notice that the azimuth angle spread is more impacted by the new rays than the elevation angle spread (see bottom graphs in Figure 5.5). This is a hint that the newly created rays are coming from new azimuth directions but similar elevation directions.

5.3.2 MIMO correlation

In order to add some system parameters, the MIMO correlations are studied. Indeed, they are related to the antenna array used, and especially to the antenna spacing relative to the wavelength of the carrier frequency.

The considered antenna array is made of eight dipole antennas, uniformly distributed on two circles located at different heights. This enables to obtain spatial resolution both in the azimuth and elevation angle domains. The geometric configuration of the array is given in Figure 5.6. Such an array is only considered at the receiver.

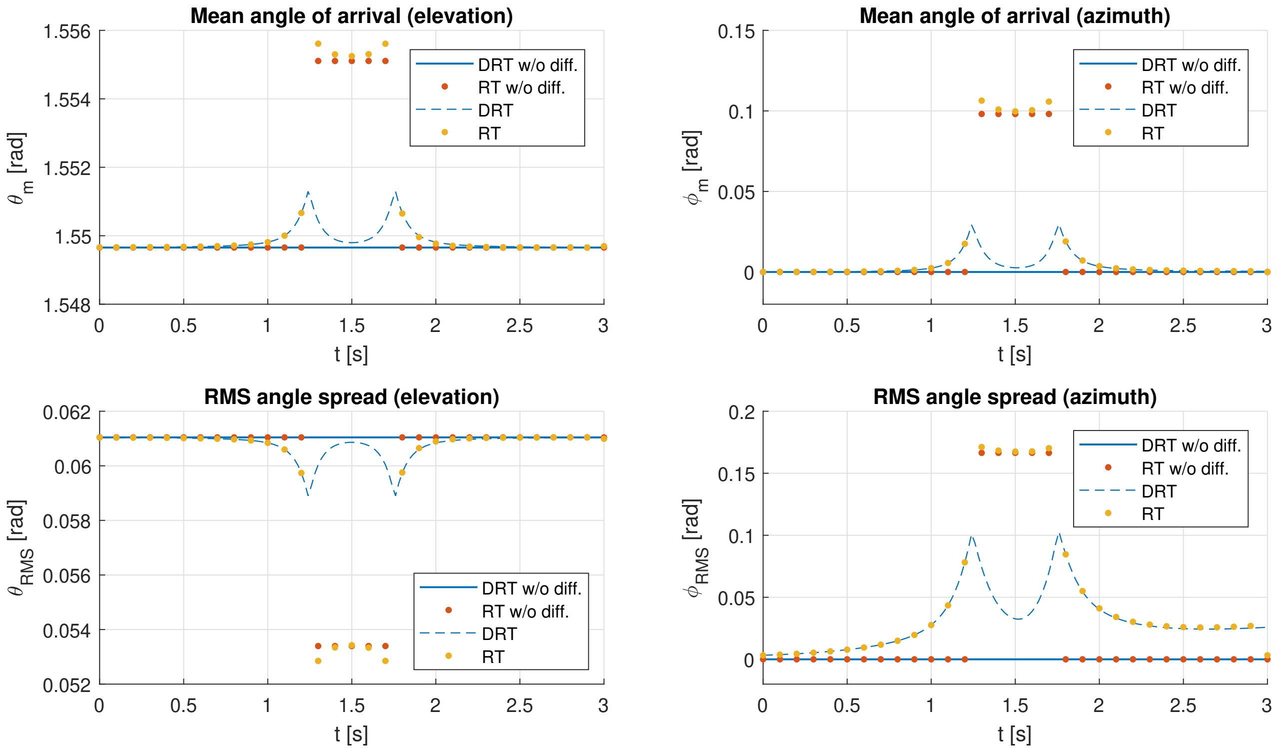

Figure 5.5: Mean and RMS angle spread of RX elevation and azimuth angles, for example of Chapter 5 - *vertical scales are different*

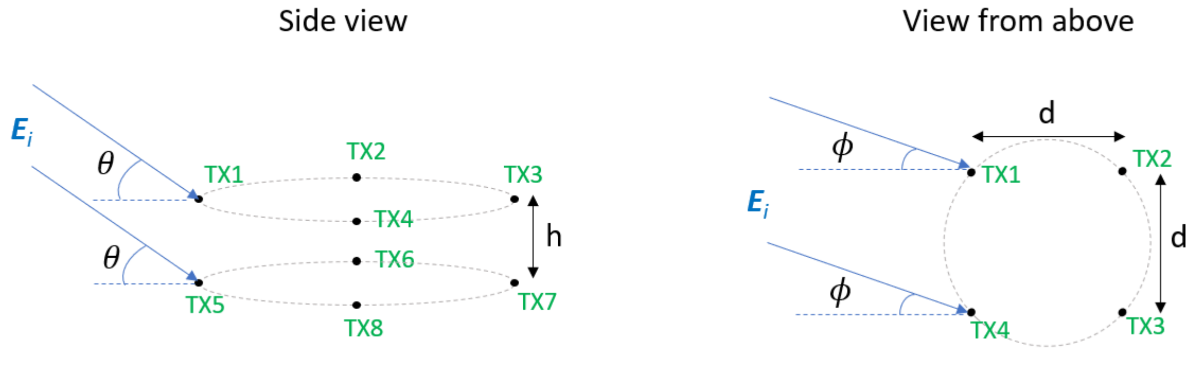

Figure 5.6: Antenna array used for MIMO correlation: ϕ is the azimuth angle of arrival, θ the elevation angle of arrival, and $\boldsymbol{E}_i$ is the incident ray

Assuming a plane wave incidence[7], it is possible to compute the phase differences between all antennas, and then obtain the correlations. Choosing antenna TX1 as phase reference, one has ψ_{1i} for phase differences between TX1 and an antenna TXi:

$$\begin{aligned}
\psi_{11}(\phi,\theta) &= 0 & \psi_{15}(\phi,\theta) &= h\sin(\theta)\\
\psi_{12}(\phi,\theta) &= d\cos(\phi) & \psi_{16}(\phi,\theta) &= h\sin(\theta) + d\cos(\phi)\\
\psi_{13}(\phi,\theta) &= d\,(\cos(\phi)+\sin(\phi)) & \psi_{17}(\phi,\theta) &= h\sin(\theta) + d\,(\cos(\phi)+\sin(\phi))\\
\psi_{14}(\phi,\theta) &= d\sin(\phi) & \psi_{18}(\phi,\theta) &= h\sin(\theta) + d\sin(\phi).
\end{aligned}$$

The instantaneous and normalized correlations between TX1 and antenna TXi are then obtained thanks to [60]

$$\begin{aligned}
\rho_{1i}(t_j) &= \frac{\int_{\theta_{RX}}\int_{\phi_{RX}} A_{RX}(t_j,\phi_{RX},\theta_{RX})\, e^{-j\frac{2\pi}{\lambda}\,\psi_{1i}(\phi_{RX},\theta_{RX})}\, d\phi_{RX}\, d\theta_{RX}}{\int_{\theta_{RX}}\int_{\phi_{RX}} A_{RX}(t_j,\phi_{RX},\theta_{RX})\, d\phi_{RX}\, d\theta_{RX}} && (5.23)\\
&= \frac{\sum_{k=1}^{N_j} |\alpha_k|^2\; e^{-j\frac{2\pi}{\lambda}\,\psi_{1i}(\phi_{RX,k},\theta_{RX,k})}}{\sum_{k=1}^{N_j} |\alpha_k|^2}. && (5.24)
\end{aligned}$$

With similar developments, the phase differences and the correlations between any two antennas can be computed, and the correlation matrix (of size 8x8) can be built:

$$\mathbf{R}_c(t_j) = [\rho_{ki}(t_j)]_{k,i}\,. \tag{5.25}$$

Monitoring the evolution of each element of the matrix is not convenient. Instead, the matrix collinearity between the initial correlation matrix $\mathbf{R}_c(t_0)$ and the one at time t_j is used, and is defined by [60]

$$c(t_j) = \frac{\left|\mathrm{Tr}\left(\mathbf{R}_c(t_0)\,\mathbf{R}_c^H(t_j)\right)\right|}{\|\mathbf{R}_c(t_0)\|_F\;\|\mathbf{R}_c(t_j)\|_F}, \tag{5.26}$$

where $\mathbf{A}^H$ denotes the Hermitian matrix of matrix $\mathbf{A}$, $Tr\,(\mathbf{A})$ is the trace of $\mathbf{A}$, and $\|\mathbf{A}\|_F$ is its Frobenius norm. The collinearity varies between zero (for orthogonal matrices) and one (fully correlated matrices).

Sensitivity to antenna spacing If the antennas are too close from each other (relatively to the wavelength of the carrier frequency), their correlation will be close to one and detection of paths with different angles of arrival will be more difficult. Hence, the ratio d/λ or h/λ that intervenes (implicitly) in equation (5.24) is an important system parameter. The evolution of the matrix collinearity for the considered example is given in Figure 5.7, for different $d/\lambda = h/\lambda$ ratios. As expected, the impact of the new reflection rays on the collinearity is negligible for small ratios, whereas it starts to become important for larger ratios. Results presented in Figure 5.7 are obtained thanks to RT simulations since the new created rays are not identified with the DRT approach. Therefore, the collinearity in DRT does not change significantly with time (even though few variations are observed since the power of the diffraction rays varies with time).

---

[7] Which is a strong assumption since rays have been modeled as spherical waves. However, provided that the distance between TX and RX is large, the wavefronts may be considered as nearly plane when reaching the receiver. To avoid this assumption, one should consider several receivers (one for each antenna) and determine the electric field value at each receiver using RT simulations for each RX.

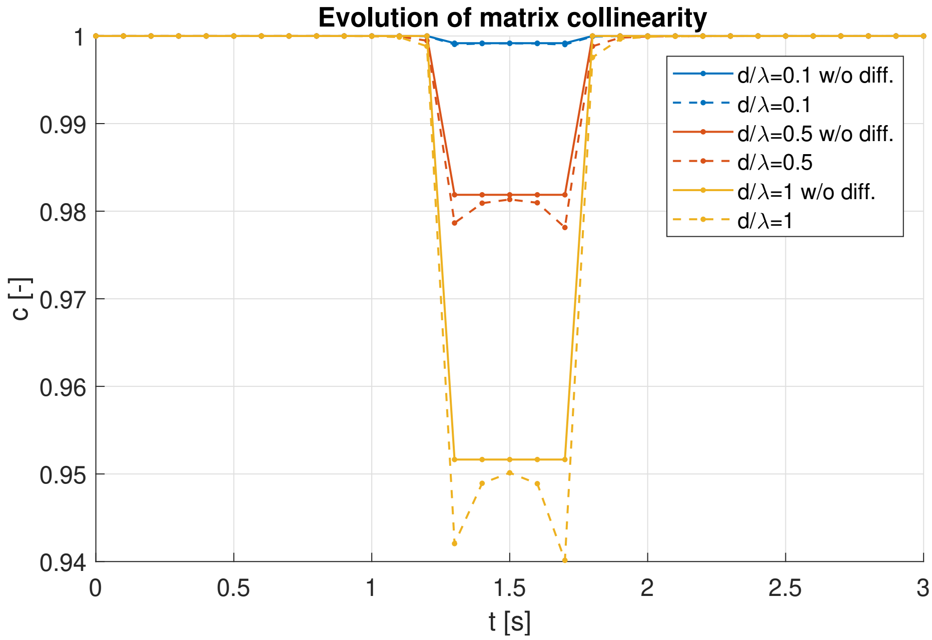

Figure 5.7: Evolution of matrix collinearity for example of Chapter 5, studied for different ratio of $d/\lambda = h/\lambda$

5.4 Other quantities

Other quantities taking into account only the power can be derived, such as the total received power and the K-factor.

5.4.1 Total received power

Starting from the instantaneous power delay profile $P(t_j, \tau)$ given by (5.4), integration over the delay τ gives the total received power $P_{tot}(t_j)$ at time t_j:

$$P_{tot}(t_j) = \int_0^{+\infty} P(t_j, \tau)\, d\tau = \sum_{k=1}^{N_j} |\alpha_k|^2 . \tag{5.27}$$

This corresponds to the total received power if all rays arrived with the same delay τ and were aggregated in one tap. This power is quite sensitive to the creation of new rays since it will be increased by the power of these rays. This is indeed observed in Figure 5.8a, where $P_{tot}(t_j)$ is normalized by the initial total received power $P_{tot}(t_0)$ and expressed in dB.

5.4.2 K-factor

The K-factor, or Rician K-factor, enables to indicate how strong is the dominant ray w.r.t. the other rays and if the channel can then be assumed to be Rician. Indeed, a channel is said to be Rician if there is a path with a contribution much more important than the contributions of all other paths. Following this interpretation, the definition of the K-factor K_F is the ratio

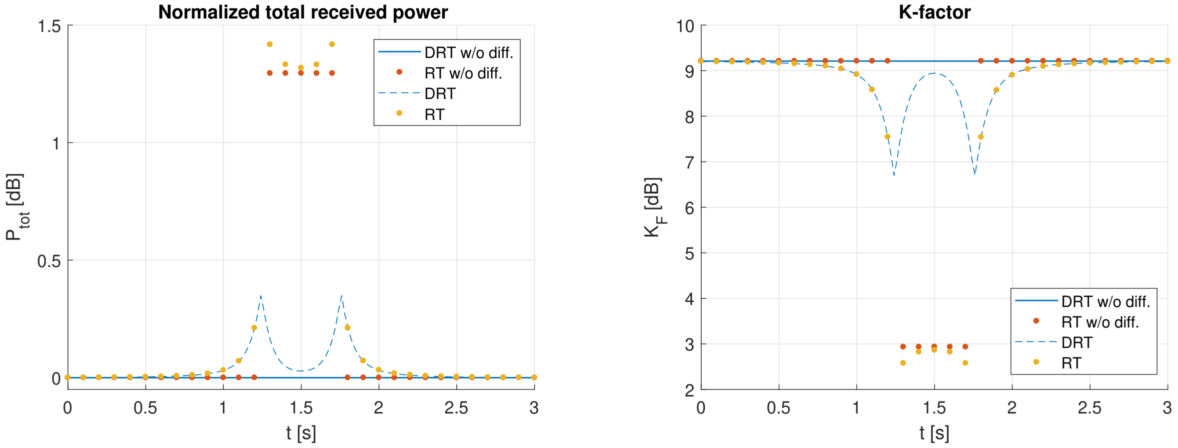

(a) Normalized total received power

(b) K-factor

Figure 5.8: Evolution of the normalized total received power and the K-factor for example of Chapter 5

between the power of the main path and the sum of the power of all other paths, expressed in dB [57]:

$$K_F(t_j) \;=\; 10\,\log_{10}\left(\frac{\max_\tau\, P(t_j,\tau)}{P_{tot}(t_j) - \max_\tau\, P(t_j,\tau)}\right) \;=\; 10\,\log_{10}\left(\frac{\max_k |\alpha_k|^2}{\sum_{k=1}^{N_j} |\alpha_k|^2 - \max_k |\alpha_k|^2}\right). \tag{5.28}$$

However, this metric may be less relevant in channels that are far from being Rician, i.e. in which there are many MPCs whose powers sum to a power greater than the one of the main path. The evolution of the K-factor for the example is given in Figure 5.8b. In this case, when the new rays appear, the power of the main path (the LOS in the example) is not modified but the denominator in the logarithm in equation (5.28) increases, reducing the K-factor.

5.5 Summary of all channel metrics

In this chapter, several channel metrics that will prove to be useful in the following part of this work have been derived.

On the one hand, some metrics, such as the delay spread, the angular spread, the total received power and the K-factor, look only at the channel itself, disregarding some system parameters. Therefore, they will always be impacted by the creation of new rays, and the higher the power of these new rays, the greater the impact on the metrics.

On the other hand, the spectral divergence and the MIMO correlations are sensitive to, respectively, the bandwidth and the antenna spacing in the antenna array. Since they involve system parameters, the impact of new rays can be mitigated depending on the considered system.

Chapter 6

Study of canonical configurations

In this chapter, several canonical configurations are studied in order to validate the DRT approach completely, from the geometry to the computation of the electric fields and the channel metrics. Moreover, the impact of the forgotten rays is now taken into account to characterize the extrapolation time, i.e. the time during which one can perform DRT simulations and still get a "*good knowledge*" of the channel. After the extrapolation time, it will be recommended to perform again a classical RT simulation and use it as a new initialisation for the DRT approach.

The analytical DRT approach is used for all examples since constant velocities are assumed. With this assumption, analytical DRT and DRT with numerical integration using analytical substitution give the same results. Hence, there is no need for considering both approaches. Furthermore, unless it is specifically stated, the carrier frequency used in the following examples is 1.8 GHz and the effective relative permittivity is set to $\epsilon_r^{eff} = 4.44 - j\,0.001$ [31, 55]. The maximum number of interactions is 3. The TX antenna is assumed isotropic whereas the RX antenna is either a vertical dipole or the antenna array presented in Section 5.3.2.

First, a simple example with only one ground reflection is considered, before studying deeper the example already presented in Section 4.3.3 (three-body configuration). Then, the example of Chapter 5 (one moving body) is reconsidered in order to characterize the lifetime of the reflection rays. This leads to several "rules" that can give the extrapolation time. Finally, the geometry of a street involving the creation of multiple rays is studied.

6.1 Ground reflection

The geometry of the first canonical configuration studied is quite simple: there is no body in the environment, only the ground is modeled. The transmitter is 5 meters above the ground, located in $(-25, 10, 5)^T$, and moving towards the receiver with a velocity vector of $(20, 0, 0)^T$. The receiver, initially in $(25, 10, 5)^T$, is moving away from the transmitter, while also moving upwards (velocity vector of $(15, 0, 5)^T$). The observed RMS delay spread as well as the evolution of the normalized total received power are given in Figure 6.1.

For this example, there is no creation or suppression of rays. Therefore, starting with a RT initialisation in $t = 0$ s, the DRT approach can then be used indefinitely, with a theoretical infinite accuracy. This is indeed observed, since DRT and RT results are superimposed (e.g. for the RMS delay, the mean error between RT and DRT results is in the order of 10^{-14} s).

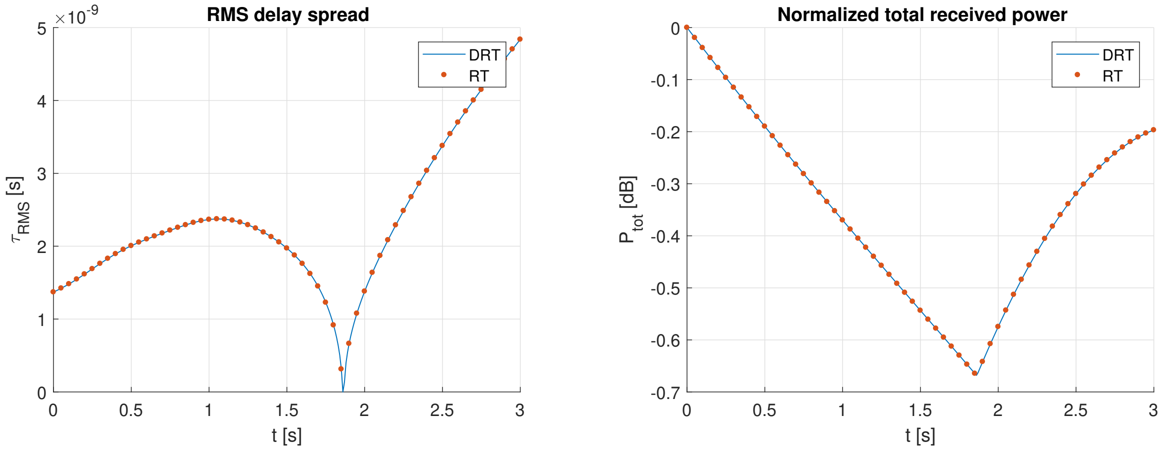

(a) RMS delay spread (b) Normalized total received power

Figure 6.1: Evolution of RMS delay spread and normalized total received power (for ground reflection)

Even though this example is quite simple, it enables to validate the DRT approach at the level of the channel metrics. Moreover, it also emphasizes the interpolation capabilities of the DRT approach: it can be used to know the smooth evolution of channel quantities between instants where RT simulations are performed (e.g. see red dots in Figure 6.1 computed every 0.05 second versus the blue smooth curve, with points every 0.01 second).

Finally, this example also highlights the possible large variations of the channel metrics, even if the same rays are considered. Indeed, close to 1.78 seconds of simulation time, an important dip is observed in both metrics, with the RMS delay spread going to zero because the ray reflected by the ground virtually disappears (i.e. the ray exists geometrically but it does not convey any power). This phenomenon is a direct consequence of the Brewster angle[8]: for a particular angle, the parallel Fresnel reflection coefficient is zero. Since the RX antenna is a vertical half-wavelength dipole, it can only recover the electric field which is parallel to the incidence plane, explaining why, if this field component goes to zero, nothing is detected at the receiver. Nevertheless, the variation of the rays power is also accurately modeled in the DRT approach, thanks to the recomputation of the electric field from the rays geometry.

6.2 Three-body configuration

The configuration presented in Section 4.3.3 of Chapter 4 on which the DRT approach has been validated geometrically is considered again (see Figure 4.10). However, this time one looks at the channel quantities (and not at the geometrical ones), in order to make sure that the (re-)computation of the electric field due to reflection and diffraction rays is correctly implemented in the DRT. Illustrations of some results are given in Figure 6.2, where DRT is performed every 0.01 second, and compared with RT every 0.1 s. Results are again superimposed, with an average error on the delay spread of 1.4 ps. The maximal value of the spectral

---

[8] In fact, since the relative permittivity takes into account the losses and is a complex number, one talks about the *pseudo-Brewster angle* [61].

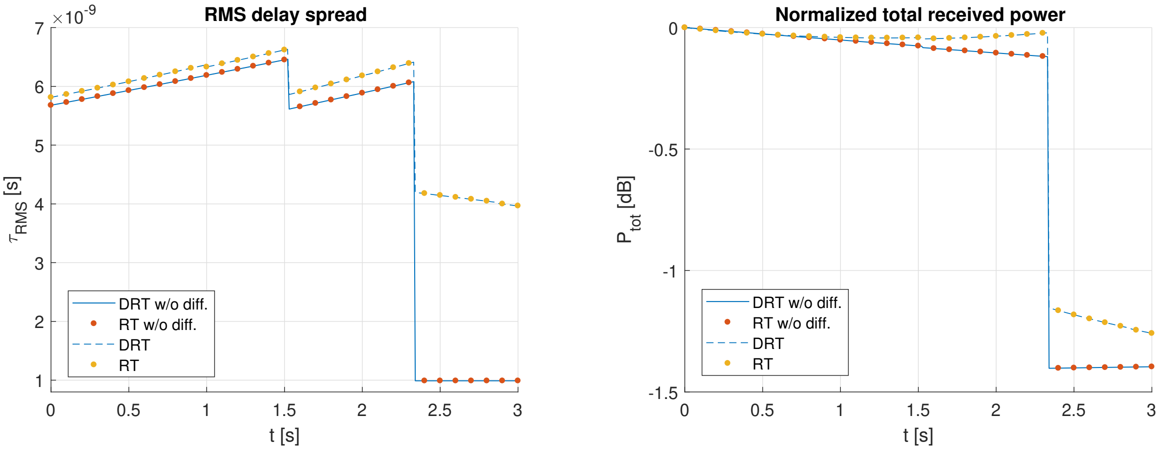

(a) Delay spread

(b) Normalized total received power

Figure 6.2: Evolution of RMS delay spread and normalized total received power (for three-body configuration)

divergence, achieved with a bandwidth of 10 MHz, is 3.3×10^{-9}, which is negligible. As a reminder, in this example there is no creation of rays, explaining this perfect fitting of the results. Nevertheless, rays suppression occurs, and is also identified thanks to the sudden falls in the metrics at 1.5 and 2.4 seconds.

Furthermore, it is now possible and meaningful to compare RT and DRT execution times on this example, since both approaches provide the same outputs, i.e. the ray quantities and the channel metrics. The RT simulations took 398.2 seconds, whereas the analytical DRT approach took 140.8 seconds (+13 seconds for the RT initialisation) to complete[9]. On such an example, the gain of computation time is small and quite far to what has been presented previously in Table 4.1. This is because results of Table 4.1 only takes into account the computation of the geometry of the reflection rays. In fact, the obtained 140.8 seconds of DRT are split according to:

- 0.25 second for computing the rays geometry;
- 0.05 second for the computation of the electric field of all reflected rays;
- 128.5 seconds corresponding to the evaluation of the electric field due to diffracted rays;
- 12 seconds for plotting the dynamic evolution of the geometry.

Clearly, a lot of time is spent in the computation of diffracted electric fields, namely owing to the Fresnel integrals involved (see Section 3.3.2). This time is also embedded in the 398.2 seconds for the RT simulations. The only way to reduce it is either to change the diffraction model or to avoid recomputing the diffracted electric fields.

Nevertheless, by removing the time necessary for the computation of diffracted electric fields from RT and DRT simulation times (assuming it is the same, which is reasonable since

---

[9] For this comparison to be relevant, DRT is now performed every 0.1 s of simulation time, i.e. only at instants where RT simulations are made.

Carrier frequency	ϵ_r^{eff} of brick wall	ϵ_r^{eff} of ground
0.1 GHz	$5.3 - 0.791\,j$	$3 - 0.027\,j$ [10]
1 GHz	$5.3 - 0.300\,j$	$3 - 0.0027\,j$
10 GHz	$5.3 - 0.700\,j$	$3 - 0.09\,j$

Table 6.1: Values of effective relative permittivities for several carrier frequencies

the same diffraction model is used), as well as the time spent in plotting in DRT, one benefits from a gain of computation time of nearly three orders of magnitude (i.e. when comparing approximately 275 s for RT and 0.3 s for DRT). This computational gain will be further studied and quantified on more complex examples.

Last but not least, the carrier frequency dependency has also been studied on this example. The major impact of the carrier frequency f_c is to modify the effective relative permittivities ϵ_r^{eff}. The link between these quantities is indeed given by

$$\epsilon_r^{eff} = \epsilon_r - j\frac{\sigma}{\omega\epsilon_0}, \tag{6.1}$$

with ϵ_r the relative permittivity, σ the conductivity of the medium, and $\omega = 2\pi f_c$.

Usually, the real part of ϵ_r^{eff} does not vary that much with the carrier frequency, on the contrary of its imaginary part varying because of the ω at the denominator but also due to the frequency dependency of the conductivity. Considering a brick wall with a relative humidity of 5% and a relatively dry ground, the computed values of the effective relative permittivities for several carrier frequencies are given in Table 6.1. These values are based on [48], using equation (6.1).

The evolution of the delay spread depending on the carrier frequency is given in Figure 6.3. It can be observed that modifying the carrier frequency and therefore the effective relative permittivities has a slight impact on the reflection rays since all curves neglecting diffraction rays are nearly superposed. However, the impact on the diffraction rays is more important. Indeed, at 0.1 GHz for example, the relative power of the diffraction rays is larger, explaining why the delay spread increases.

More conclusions can surely be drawn from a thorough study of the carrier frequency dependency of RT simulations but is not the purpose of this work. The important result from this analysis is the motivation to use relative levels instead of absolute levels when comparing the channel metrics. This comes from observations based on Figure 6.3: for a same configuration of the rays, the absolute variations in RMS delay spread depend on the chosen carrier frequency (see the variation of the absolute height of the dip at 2.4 seconds for example).

---

[10] Assuming same conductivity as at 1 GHz.

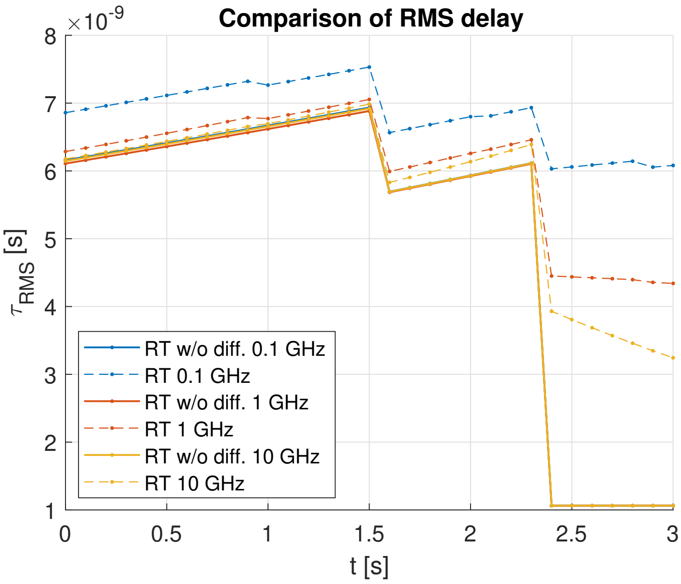

Figure 6.3: Evolution of RMS delay spread depending on carrier frequency (three-body configuration)

6.3 One moving body and associated extrapolation time

6.3.1 With fixed TX and RX

Based on the two previous examples, the extrapolation time during which DRT can be performed is infinite because there is no creation of rays in the studied geometries. On the contrary, the simplest example involving rays creation is the one given in Chapter 5, see Figure 5.1. The impact of the created rays on the metrics has already been studied in the previous chapter, now one is interested in the lifetime of the new rays. For this, focus is only given to new reflection rays, since they have most power and therefore more impacts on the channel metrics. Looking at the spectral divergence without diffraction rays (see Figure 5.3) enables to determine the time interval where DRT and RT results are different due to the new rays, giving the lifetime of these new rays. For maximizing the impact, a bandwidth of 100 MHz is considered.

Two parameters are expected to influence the lifetime: the velocity of the moving body, and its width (i.e. the length of the body along the x-axis in our case). Their respective effects are depicted in Figure 6.4, leading to several comments:

- Increasing the speed of the moving body leads to a sooner and shorter apparition of the new rays (see Figure 6.4a). This results from the fact that the new rays appear and disappear after that the body has traveled given distances, which depend only on the geometry and are independent of the velocity. One can also observe that multiplying the speed by two makes the lifetime twice smaller.
- In Figure 6.4b, one can conclude that the wider the body, the greater the lifetime. It is possible to go even further, by noticing that doubling the body width leads to a twice larger lifetime. There is thus a proportionality relationship between these two quantities.

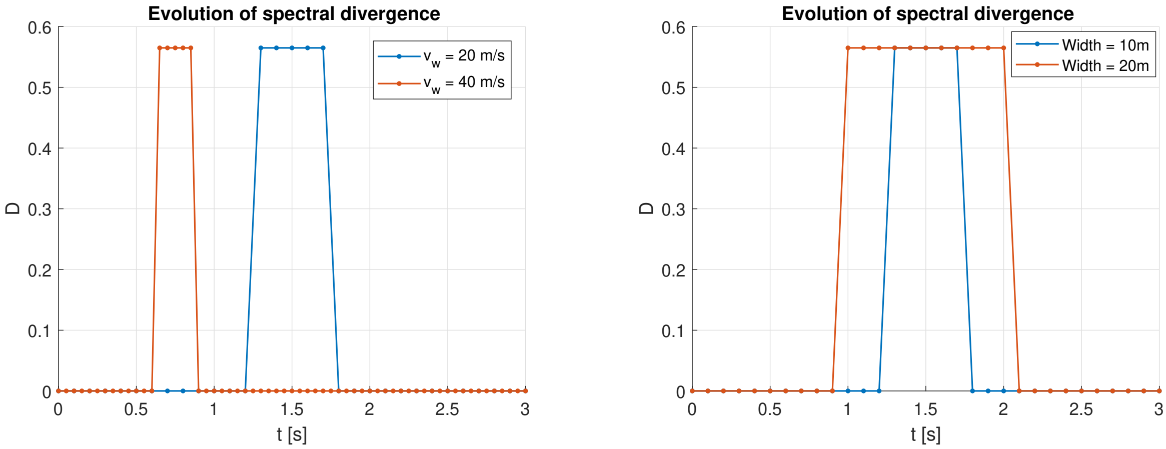

(a) Study of body velocity (width = 10 m) (b) Study of body width (velocity = 20 m/s)

Figure 6.4: Evolution of spectral divergence (for one moving body configuration)

Therefore, thinking in terms of extrapolation distances instead of extrapolation times may be more relevant. Indeed, the new reflected rays will live as long as their reflection points fall within the body surface, which is limited by its width. In this simple example, the extrapolation distance should then be shorter than the body width so that one makes sure to find the new reflected rays at least at one instant. Then, the lifetime is related to this extrapolation distance by dividing it by the body velocity. The suggested extrapolation time t_{ext} is

$$t_{ext} = \frac{d_{ext}}{v_w} \leq \frac{d_w}{v_w}, \tag{6.2}$$

where d_{ext} is the extrapolation distance (to be chosen), d_w the width of the body and v_w its velocity. The ratio $\frac{d_w}{v_w}$ is actually the lifetime of the new rays, that can be measured in Figure 6.4 (e.g. for $v_w = 20$ m/s and $d_w = 10$ m, one has a lifetime of 0.5 s, as seen in blue in Figure 6.4a, from 1.25 to 1.75 seconds).

6.3.2 With moving TX and RX

Similar expressions as (6.2) are obtained in cases where the transmitter or the receiver are moving. In these cases, v_w in (6.2) must be substituted by the relative velocity of the reflection point. An analytical expression of the absolute velocity has been obtained in Chapter 4, as given in equation (4.12). As mentioned previously, this velocity is not constant in all generality even if constant velocities have been assumed in the geometry (for TX, RX and all moving bodies). Nevertheless, in a simple case where TX, RX and the body only have velocities in the x-direction (so that their y-positions remain constant), the reflection point velocity is then a constant and is given by

$$v_{IX,x} = \frac{y_{RX} - y_w}{y_{RX} - 2y_w + y_{TX}} v_{TX,x} + \frac{y_{TX} - y_w}{y_{RX} - 2y_w + y_{TX}} v_{RX,x}, \tag{6.3}$$

and

$$t_{ext} \leq \frac{d_w}{v_{IX,x} - v_{w,x}}, \tag{6.4}$$

where $\frac{d_w}{v_{IX,x} - v_{w,x}}$ is again the lifetime of the new rays. The velocity at the denominator is the relative velocity of the reflection point, i.e. its velocity with respect to the wall velocity $v_{w,x}$. For example, considering a transmitter initially in $(-45, 10, 5)^T$ moving with a constant velocity $(12, 0, 0)^T$, and a receiver in $(-25, 10, 5)^T$ with a constant velocity of $(8, 0, 0)^T$, as well as a single body of width 10 m and centered on $x = 0$ with $y_w = 0$ (same as in Figure 5.1b), one gets the results presented in Figure 6.5. Indeed, if the body is kept fixed ($v_w = 0$), the ratio $\frac{d_w}{v_{IX,x} - v_{w,x}}$ is equals to $\frac{10}{10} = 1$ second, as seen in blue (new rays between 0.5 and 1.5 seconds of simulation time). With a body moving at 5 m/s, one gets $\frac{d_w}{v_{IX,x} - v_{w,x}} = \frac{10}{10-5} = 2$ seconds, which corresponds to the rays lifetime given by the red curve.

Finally, in cases where TX, RX or the body also have y- and z-velocity components, equations (6.3) and (6.4) are not true anymore, since the velocities of the reflection points will not be constant.

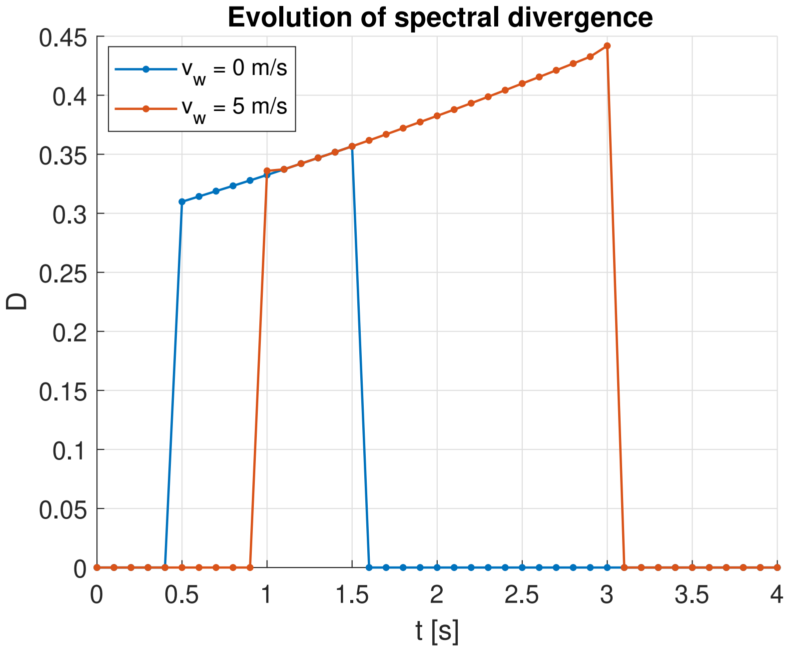

Figure 6.5: Evolution of spectral divergence (for one moving body configuration, with TX-RX moving)

6.3.3 Generalisation to complex geometries

In the case of complex geometries involving several moving bodies, it is not easy to obtain an expression of the accurate lifetime of the rays. This is especially true because there will be multiple reflection rays, having their own lifetime. These lifetimes are difficult to estimate beforehand, since it would require to know the width of the bodies with which new rays will interact. Moreover, computation of relative reflection points velocities is also difficult and these velocities will certainly not be constant.

Instead, the following rule is suggested, as an approximation for an upper bound for the extrapolation time:

$$t_{ext} \leq \frac{d_{min}}{v_{max}}, \tag{6.5}$$

where d_{min} is the minimal length (or width or height, i.e. the smallest dimension) of the bodies in the geometry on which a reflection may occur during the dynamic evolution of the geometry. Moreover, v_{max} is the maximal amplitude of all velocities in the geometry, i.e. considering the velocities of all bodies but also of the transmitter and the receiver. Equation (6.5) leads to two important observations:

- It does not provide a real upper bound for the extrapolation time, or equivalently a lower bound for all (reflection) rays lifetime. Indeed, as shown in Section 6.3.2, one must use the relative velocity of the reflection points at the denominator and not an absolute velocity. In a general case, finding these relative velocities or even an upper bound for these is difficult and not practical. However, in a scenario with 1D motion, it is possible to upper bound the maximal relative velocity by twice the maximal velocity v_{max}, i.e. $v_{rel,max} < 2\,v_{max}$. Indeed, this assumes a pessimistic scenario in which the velocity of the reflection point is equal to v_{max} (which is its maximal value, see (6.3) with $v_{TX,x} = v_{RX,x} = v_{max}$), whereas the body on which there is the reflection is moving in the opposite direction with a velocity of $-v_{max}$. In this case (1D motion), taking

  $$t_{ext} \leq \frac{d_{min}}{2\,v_{max}}, \tag{6.6}$$

  gives a real upper bound.

- Upper-bounding the extrapolation time ensures that all reflection rays will be found at least at one instant by using a new RT initialisation. Nevertheless, it does not give any confidence about the instant where the new RT initialisation will occur: it can be at the beginning of the apparition of the new rays, or at the end, and this strongly depends on the initial configuration of the geometry. A possible solution to make sure to find the new rays at the beginning of their apparition would be to use

  $$t_{ext} \leq \frac{1}{10}\frac{d_{min}}{v_{max}}, \tag{6.7}$$

  for example, so that it can be expected that each ray will be found for at least around 90% of their lifetime. However, this is a rather pessimistic and strong constraint since few or no rays will have a lifetime approximately equals to $\frac{d_{min}}{v_{max}}$.

In short, three possible "rules" giving the extrapolation time to use with complex geometries have been derived in equations (6.5) to (6.7). Each of them are based only on the knowledge of the geometry and its evolution and will be applied to more complex geometries.

6.4 Street configuration

The last canonical configuration studied in this chapter is similar to a city street with 2 lanes. It is a canyon of height 10 meters in which vehicles are moving in straight lines (1D motion). The initial and final configurations are depicted in Figure 6.6. Vehicles 1, 2 and 3 are moving to the right with respective velocities of 12, 15 and 15 m/s, whereas vehicles 4 and 5 move to the left, at -15 and -12 m/s. Cars (1, 3 and 4) are modeled by rectangular cuboids having a length of 5 meters, a width of 2 meters and a height of 2 meters; while trucks or buses (2 and 5) are 10-meter long, 2-meter large and 4-meter tall cuboids. The transmitter (resp. receiver) is initially located in $(-57.5, 0, 2.5)^T$ (resp. in $(-27.5, -2, 2.5)^T$) and is moving at 18 m/s (resp. 15 m/s) to the right. For this configuration, the maximal number of interactions is set to 2.

Such a configuration has been chosen since it involves the creation and suppression of several reflection rays as well as the LOS ray. This can be seen in Figure 6.6 on the initial and final configurations, but also in Figure 6.7 depicting the evolution of the total received power, with RT and DRT simulations performed every 0.01 second (but RT simulations are only represented every 0.1 s). In this last figure, the chosen extrapolation time is 0.01 s, explaining why RT and DRT results are perfectly superimposed. Most of the rays are modified between 1.5 and 3 seconds of simulation time.

Based on the geometry, the minimal length of the body on which there can be a reflection is 2 meters (e.g. width of body 5 in Figure 6.6) and the maximal velocity is the one of the transmitter, i.e. 18 m/s. According to (6.5), this gives an approximate upper bound on the extrapolation time equal to 0.11 s. However, equations (6.6) and (6.7) suggest to take 50% or even 10% of this value. The purpose of this section is therefore to establish the validity of these “rules of thumb” used to find the extrapolation time on a quite realistic example. In order to achieve this goal, channel as well as system metrics are studied, with different extrapolation times.

6.4.1 Channel metrics

The considered channel metrics are the delay, azimuth and elevation spreads, as well as the K-factor and the total received power. For each of these metrics, it is desired that the results given by DRT are close to the ones obtained with RT, for most of the time. Therefore, it is suggested to determine the percentage of simulation time during which the relative error on the channel metrics (between RT and DRT) is below a given level, say 20%. For example, regarding the delay spread, the percentage of the time where

$$\left| \frac{\tau_{RMS}^{RT}(t_j) - \tau_{RMS}^{DRT}(t_j)}{\tau_{RMS}^{RT}(t_j)} \right| \leq 0.2, \tag{6.8}$$

holds is computed, with $\tau_{RMS}^{RT}(t_j)$ the delay spread obtained using RT and $\tau_{RMS}^{DRT}(t_j)$ obtained using DRT. As stated previously, RT and DRT simulations have been performed every 0.01 second (t_j), therefore the time percentage results from counting the number of discrete time instants t_j where (6.8) is true.

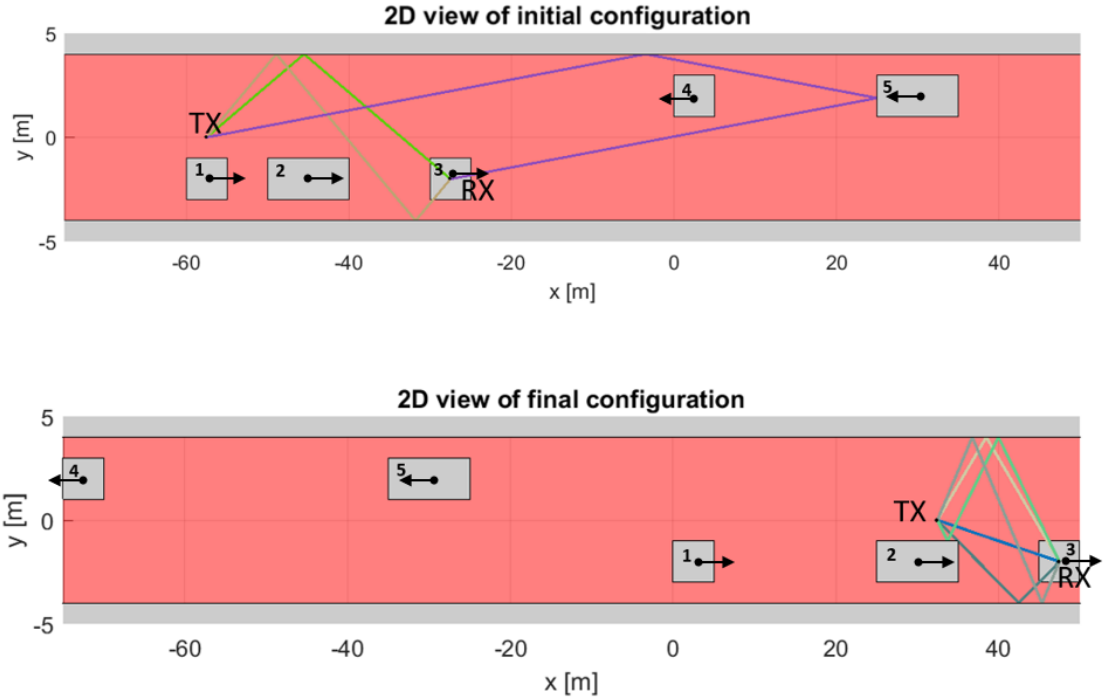

Figure 6.6: Upper view of initial and final configurations for the **street configuration**, with all reflection rays *(scales in x and y are different)*

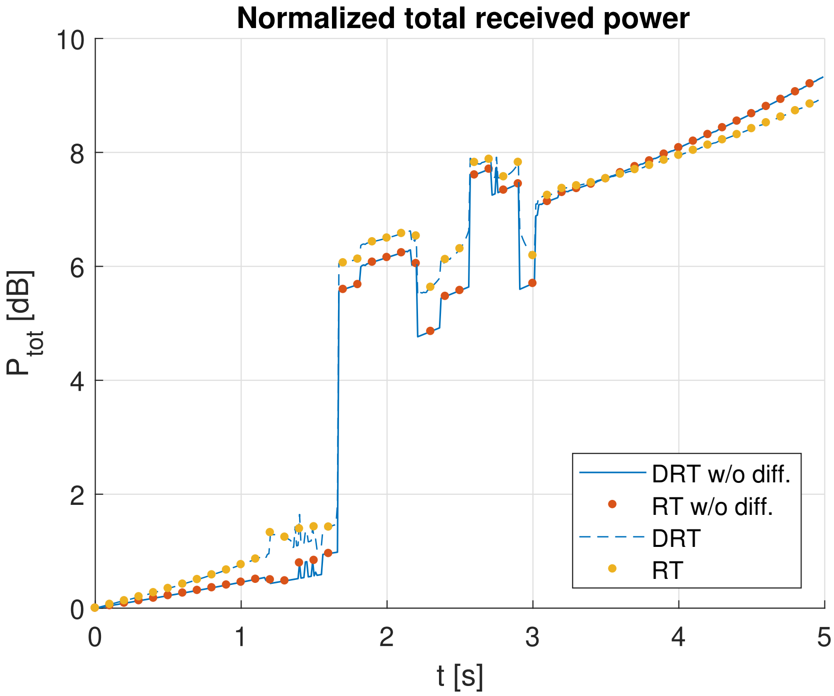

Figure 6.7: Evolution of normalized total received power for the **street configuration** *(with an extrapolation time of 0.01 second, meaning that each RT simulation is used as initialisation for DRT)*

On the one hand, the choice of using a relative error is motivated by the dependency of the values of the channel quantities with the carrier frequency (as it has been briefly studied in Section 6.2). On the other hand, fixing the acceptable relative error level at 20% is mostly based on observations of the variations of the channel metrics. Indeed, it has been observed that the creation of important rays, such as the LOS or main reflection rays, has a strong impact on the metrics (see Figure 6.7 for example, with the creation of the LOS ray close to 1.7 second), whereas the creation of diffraction rays or weak reflections has a lower impact, usually below 20%. Moreover, since RT is based on the GO assumption, it is in itself an approximation of the reality with some errors. Therefore, allowing an extra 20% variation seems acceptable.

This time percentage has been recorded in Table 6.2, for several extrapolation times. This leads to several comments:

- An extrapolation time of 0.01 s means that RT simulations (that are performed every 0.01 s) are always used to feed the DRT. Therefore, a perfect accuracy is reached, no rays are missed. Such a small value for the extrapolation time is actually what is given by taking 10% of the rule $\frac{d_{min}}{v_{max}}$.
- Taking 50% of $\frac{d_{min}}{v_{max}}$, one gets an extrapolation time of 0.05 s. In this case, the percentage of the time where relative errors are below 20% is larger than 90% for all channel metrics (see second row of the table). Doubling this extrapolation time leads to the same conclusion, except for the K-factor, which is slightly below 90%. It is indeed expected that the K-factor is quite sensitive to the loss of rays.
- Increasing the extrapolation time reduces the percentage of the time during which 20% of relative errors is ensured. This is directly linked to the fact that new rays are missed more often.
- However, with an extrapolation time of 2 seconds, one gets a time percentage of more than 70% on all metrics. This surprising results is explained by inspecting Figure 6.7: using $t_{ext} = 2$ seconds means that RT initialisation is performed at time 0 s, 2 s and 4 seconds. As it can be hinted from the smooth variations on the metric, no rays are created before 1 second and after 3 seconds of simulation time. Moreover, the rays found at time 2 seconds are actually the same as the ones that remain after 3 seconds. By chance, results from time 2 seconds are therefore extrapolated correctly between 3 and 4 seconds. This observation emphasizes the influence of the instants where the RT initialisation is performed, as well as the “dead times” in the simulation, i.e. times where no reflection rays are either created or suppressed. Indeed, before 1 second and between 3 and 5 seconds, no rays are created or suppressed, meaning that DRT results will always be perfect (provided they have been fed with the right rays). Such time intervals will thus always improve the time percentage where a good accuracy is reached and must ideally be avoided. Nonetheless, they can appear in practice, in a real environment.
- A final remark concerns the elevation angle spread when neglecting diffraction rays. In this case, the spread is actually zero for some simulation times, when there is no ground reflection, i.e. when all reflection rays are located in the same plane. Of course, defining a relative error w.r.t. zero is not well defined, explaining why the time percentages are

poorer. When considering diffraction rays, the elevation spread is never zero since there is always diffraction on the top of the canyon.

t_{ext}	Delay spread	Azimuth spread	Elevation spread	K-factor	Total received power
0.01 s	100.00	100.00	100.00	100.00	100.00
0.05 s	95.41 (95.81)	96.61 (96.61)	99.00 (56.89)	93.21 (92.01)	97.80 (97.40)
0.1 s	91.42 (94.21)	95.21 (95.21)	99.00 (54.29)	89.02 (88.62)	95.81 (95.41)
0.2 s	84.83 (89.42)	91.22 (91.22)	97.21 (47.90)	83.23 (81.44)	90.42 (90.02)
0.3 s	84.03 (85.03)	89.02 (89.02)	95.21 (49.10)	75.65 (71.46)	86.23 (85.23)
0.5 s	74.05 (70.66)	75.65 (75.65)	91.22 (43.31)	68.46 (66.28)	74.25 (71.36)
1 s	58.88 (56.89)	61.28 (61.28)	90.42 (43.51)	57.09 (55.09)	69.26 (64.87)
1.5 s	48.70 (44.51)	43.71 (43.71)	71.26 (30.94)	47.11 (45.31)	49.10 (43.71)
2 s	71.66 (69.06)	79.84 (79.84)	90.42 (58.68)	78.84 (74.05)	87.82 (83.83)
2.5 s	43.71 (36.73)	37.92 (37.92)	80.44 (24.15)	38.32 (35.33)	37.33 (37.13)

Table 6.2: Percentage of simulation time for street configuration where relative error on **channel metrics** is below 20%, depending on the chosen extrapolation time (*all results are in percent, figures in parenthesis neglect diffraction rays*)

6.4.2 Bandwidth dependency

Besides the channel metrics, it is relevant to determine if constraints on the extrapolation time can be relaxed by taking into account some system parameters. Considering the bandwidth first, the spectral divergence is used and one can determine the percentage of simulation time where the spectral divergence is below 0.1. Indeed, the spectral divergence already compares RT and DRT results, there is thus no need to define a relative error level. Furthermore, the choice of 0.1 as a limit is motivated by Figure 5.3, from Chapter 5. There, it has been observed that for bandwidths leading to a limited impact on the power delay profiles, the spectral divergence is below 0.1. On the contrary, when the impact is important, the spectral divergence is greater than 0.1.

Results are gathered in Table 6.3, again for several extrapolation times. One can notice that whatever the considered bandwidth, the time percentage is greater than 90% for all extrapolation times below 0.3 second. Hence, this is the case for all extrapolation times that have been suggested following the rule $\frac{d_{min}}{v_{max}}$ (since $\frac{d_{min}}{v_{max}} = 0.11$ s). This means that the time percentage on the channel metrics is more limiting than the one on the spectral divergence.

However, for longer extrapolation times, the decrease in time percentage is greater for the 100 MHz and 1 GHz. This is directly linked to the order of magnitude of the delay spread, that varies between 1 and 25 ns. As it has been discussed in Section 5.2.2, spectral divergence will be larger for bandwidths related to the inverse of these delays.

Finally, the “lucky case” of the extrapolation time of 2 seconds is also observed.

t_{ext}	Spectral divergence			
	1MHz	10 MHz	100 MHz	1 GHz
0.01 s	100.00	100.00	100.00	100.00
0.05 s	98.40 (98.60)	99.60 (99.60)	97.80 (96.61)	98.20 (96.01)
0.1 s	98.40 (98.60)	99.20 (98.80)	97.01 (96.21)	97.21 (94.61)
0.2 s	96.41 (96.61)	96.81 (96.21)	97.01 (94.01)	93.21 (89.22)
0.3 s	94.41 (94.42)	96.01 (95.61)	95.01 (89.02)	90.22 (85.03)
0.5 s	86.23 (83.23)	87.23 (86.83)	88.82 (79.04)	83.83 (71.26)
1 s	92.81 (89.82)	85.63 (85.23)	72.65 (62.87)	65.07 (58.08)
1.5 s	73.65 (73.25)	72.26 (65.47)	62.08 (46.91)	55.09 (43.71)
2 s	92.81 (89.82)	89.82 (92.01)	87.23 (77.25)	84.03 (77.04)
2.5 s	80.04 (59.08)	65.87 (50.90)	52.69 (41.52)	53.29 (37.13)

Table 6.3: Percentage of simulation time for street configuration where relative error on **spectral divergence** is below 0.1, depending on the chosen extrapolation time and the bandwidth (*all results are in percent, figures in parenthesis neglect diffraction rays*)

6.4.3 Antenna array dependency

The second system parameter studied in this work is the ratio $d/\lambda = h/\lambda$, with d and h being characteristic dimensions of the antenna array (Figure 5.6). In this case, this is the evolution of the absolute error on the matrix collinearity that is monitored, i.e.

$$\left| c^{RT}(t_j) \; - \; c^{DRT}(t_j) \right| \; \leq \; 0.05, \tag{6.9}$$

with $c^{RT}(t_j)$ the matrix collinearity computed with RT and $c^{DRT}(t_j)$ the one with DRT. Again, this is the time percentage where equation (6.9) is true that is monitored and given in Table 6.4. An absolute error has been chosen since the collinearity can only vary between 0 and 1, and the choice of the particular value of 0.05 enables to be quite sensitive to the modification of main reflection rays while disregarding the modification of diffraction rays.

Based on Table 6.4, choosing $t_{ext} = 0.2$ s still enables to have a time percentage above 90% for all ratio $d/\lambda = h/\lambda$. For the smallest ratio value (d/λ=0.1), the error on the matrix collinearity is always below 0.05, ensuring accurate results during 100% of the time. This is not surprising since with this ratio the matrix collinearity is varying slightly (see Figure 5.7 for example). What is more surprising are the good performances for $d/\lambda = 0.5$. In order to understand this results, the radiation patterns[11] of the considered antenna array are depicted in Figure 6.8. The shape of the pattern for $d/\lambda = 0.5$ is particularly interesting: there is nearly no power radiated (or received) in the azimuth plane. However, in the considered examples, most of the rays are coming in this plane, except for some diffraction rays. Therefore, the azimuth angles (and so the angular spread) is completely ignored by this array, on the contrary of the array for $d/\lambda = 1$, explaining why fewer variations are observed for $d/\lambda = 0.5$.

---

[11] Computed using the assumption of plane wave incidence and isotropic antennas.

t_{ext}	Matrix collinearity		
	d/λ=0.1	d/λ=0.5	d/λ=1
0.01 s	100.00	100.00	100.00
0.05 s	100.00	100.00 (99.20)	98.00 (97.41)
0.1 s	100.00	100.00 (98.20)	96.01 (95.41)
0.2 s	100.00	100.00 (96.81)	90.02 (89.42)
0.3 s	100.00	100.00 (96.81)	88.02 (87.23)
0.5 s	100.00	100.00 (96.81)	74.25 (73.65)
1 s	100.00	100.00 (96.61)	58.08 (58.08)
1.5 s	100.00	96.81 (98.40)	43.91 (43.71)
2 s	100.00	100.00 (96.61)	77.25 (77.05)
2.5 s	100.00	96.81 (70.06)	40.12 (39.52)

Table 6.4: Percentage of simulation time for street configuration where relative error on **matrix collinearity** is below 0.05, depending on the chosen extrapolation time and the d/λ ratio (*all results are in percent, figures in parenthesis neglect diffraction rays*)

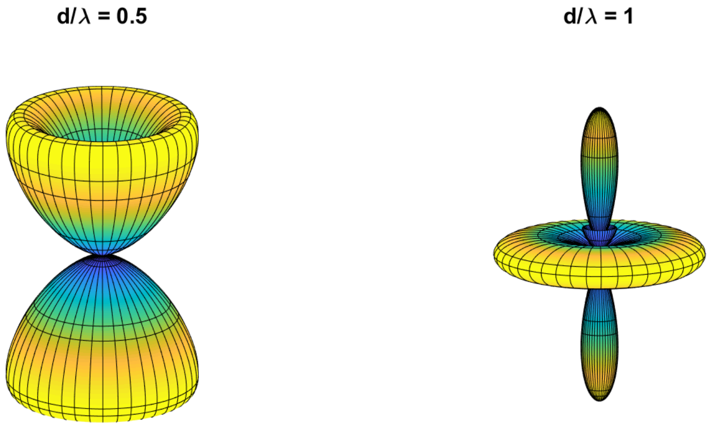

Figure 6.8: Radiation patterns of the considered array, depending on d/λ=h/λ

6.5 Summary of the study of canonical configurations

This chapter presented a comparison between RT and DRT on several canonical configurations. It enabled to get some physical insights about phenomena that could occur during RT simulations, namely the creation of rays. This latter sets constraints on the extrapolation time during which DRT can be performed accurately and a few rules have been derived to obtain beforehand an estimation of this time, in equations (6.5) to (6.7).

Comparisons between channel metrics were made in terms of percentage of simulation time where the relative error between RT and DRT results is below 20%. Regarding the system parameters, this relative error was substituted by an absolute level of 0.1 for the spectral divergence and an absolute error of 0.05 for the matrix collinearity. It was found on an example modeling a street that for small bandwidths and small d/λ ratios, constraints on the extrapolation time can be relaxed, taking for example twice the value given by (6.5) while still ensuring a time percentage of accurate results larger than 90%.

Furthermore, a first look at computational gains has been considered on the example presented in Section 4.3.3 (three-body configuration).

In conclusion, all tools are now ready to compare RT and DRT results on more complex configurations, in order to determine what is an acceptable time of extrapolation and what is the associated computational gain. These configurations must avoid "*dead times*" where no rays are created, so that more constraining conditions will be encountered.

Chapter 7

Statistical study and application to a real environment

The goal of this last chapter is to determine the validity of the dynamic ray tracing approach and the chosen rules for the extrapolation times. For this, the results of a statistical study on 60 ray tracing simulations are first presented. Then, the RT and DRT approaches are applied to a real environment in which measurements have been obtained.

7.1 Statistical study

One of the biggest remaining question at this point is related to the rules giving the extrapolation times to use for the DRT approach. Indeed, it is not clear whether taking 10%, 50% or 100% of the ratio $\frac{d_{min}}{v_{max}}$ given by equation (6.5) enables to have a sufficient accuracy on the DRT results, for a wanted percentage of the time and for most geometries. This is the reason why a statistical study has been conducted on much more configurations than the ones presented in the previous chapter.

7.1.1 Geometries and simulation parameters

In this study, three typical dynamic environments have been studied: a *city street*, a *city crossroad* and a *highway*. These environments are depicted in Figures 7.1 to 7.3. In each of these configurations, several parameters have been modified in order to perform 20 different RT simulations per configuration. This involves modifications in the transmitter, receiver, vehicles and walls initial positions and velocities.

The simulation parameters used in all configurations are given in Table 7.1. The chosen values of the effective permittivities, obtained from (6.1) are based on [31, 55] for the bricks, and on [48] for the ground (assuming a dry ground and using a linear interpolation to obtain the value of the conductivity at 1.8 GHz). Moreover, the vehicles have been modeled by rectangular cuboids (5 meters length, 2 meters width and 2 meters height for cars; 10 meters length, 2 meters width and 4 meters height for trucks/buses). They have been assumed to be made of metal, having an effective relative permittivity of $\epsilon_r^{eff} = 4.5 - j\,4 \times 10^8$ [5]. The receiver antenna is a dipole, whereas the transmitting antenna is assumed isotropic. The time interval of simulation ranges from 0 to 3.5 seconds for all configurations. RT and DRT simulations are performed and compared every 0.01 second. The following paragraphs give more details about the studied configurations.

Carrier frequency	1.8	[GHz]
Effective relative permittivity of bricks	4.44 - j 0.01	[/]
Effective relative permittivity of ground	3 - j 0.021	[/]
Maximal number of interactions	2	[/]

Table 7.1: Simulation parameters for statistical study

City street This configuration is similar to the *street configuration* presented in Chapter 6. However, more vehicles have been added in order to avoid the "dead times" where no rays are created or suppressed, as seen in Figure 7.1. Velocities of the vehicles have been varied in intensity between 5 and 18 m/s (keeping the same directions as shown in Figure 7.1). TX and RX have been considered fixed or moving and at different heights and positions.

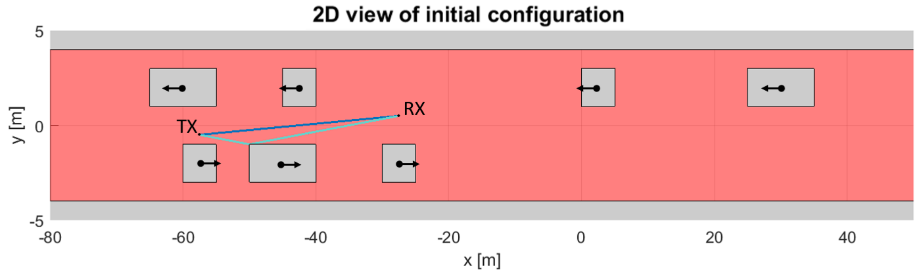

Figure 7.1: Upper view of one example of the **city street** configuration (with all reflection rays, diffraction rays not depicted) - *scales in x- and y-axis are different*

City crossroad A crossroad delimited by four buildings having a height of 10 meters is modeled, as in Figure 7.2. Again, TX, RX and vehicles velocities and positions are varied; the velocities ranging between 0 and 12 m/s. Mainly diffraction rays are linking the transmitter and the receiver in this configuration.

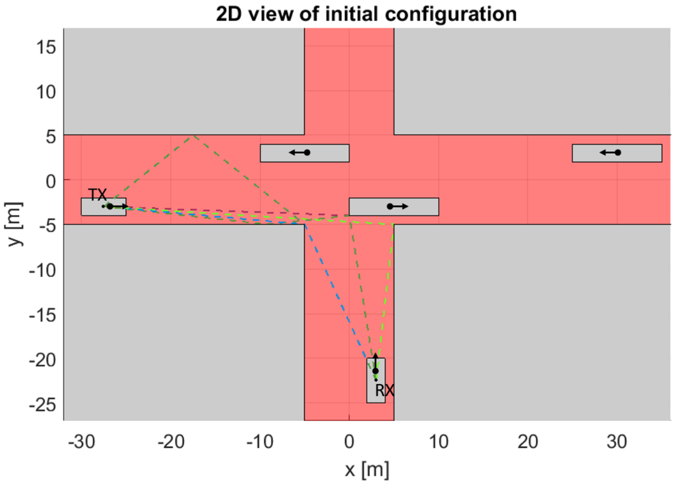

Figure 7.2: Upper view of one example of the **city crossroad** configuration (no reflection rays, diffraction rays depicted)

Highway This configuration is similar to the *city street* except that the two walls forming the canyon are removed (see Figure 7.3). Moreover, velocities are now varying between 20 and 25 m/s. TX or RX are sometimes considered to be linked to a vehicle or to be a fixed BS.

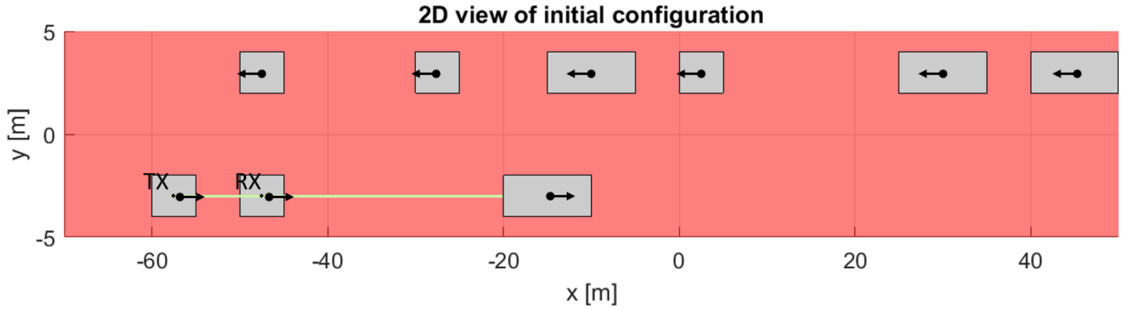

Figure 7.3: Upper view of one example of the **highway** configuration (with all reflection rays, diffraction rays not depicted) - *scales in x- and y-axis are different*

7.1.2 Conclusions from statistical study

For the sake of completeness, all results are presented in Tables 7.3 to 7.9. Depending on the configuration, three or four different "rules" giving the extrapolation time have been considered, based on equation (6.5), and are grouped in Table 7.2.

	Rule A	**Rule B**	**Rule C**	**Rule D**
t_{ext}	$\frac{1}{10}\frac{d_{min}}{v_{max}}$	$\frac{1}{2}\frac{d_{min}}{v_{max}}$	$\frac{d_{min}}{v_{max}}$	$\frac{1}{4}\frac{d_{min}}{v_{max}}$

Table 7.2: Considered "rules" for the extrapolation time - *"Rule D" is an extra rule added for the* city crossroad *configuration*

7.1.2.1 Channel metrics

Regarding the channel metrics, this is the percentage of time where the relative error is below 20% that has been recorded for the different configurations and with several rules for the extrapolation time (as in Section 6.4). The mean and the standard deviation of this time percentage have been computed, and are given in Tables 7.3 to 7.7. For all cases, *Rule A* led to extrapolation times less than or equal to 0.01 second, which is the timestep at which RT and DRT simulations are performed. This explains why this rule provides a perfect accuracy since each RT simulation was used to feed the DRT approach. However, reducing the timestep to study *Rule A* more accurately was not computationally affordable, i.e. this rule is too constraining.

Notwithstanding this observation, the general trend is the following: the longer the extrapolation time, the lower the mean percentage of time where the relative error is below 20%, and the larger the standard deviation (i.e. the larger the variations of this percentage depending on the configuration).

Moreover, regarding the *city street* and *highway* configurations, *Rule B* seems to achieve the best trade-off between having the longest possible extrapolation time while ensuring accurate results for more than 90% of the time. It also provides the lowest standard deviation (among the rules studied and excepting *Rule A*). However, for the *city crossroad* configuration, *Rule B* does not offer the 90% of time accuracy but this latter can be achieved by following *Rule D*. This means that the extrapolation time should be further reduced, probably owing to the prevalence of diffraction in this configuration. Indeed, there are mainly diffraction rays linking TX and RX in the *city crossroad* configuration, with rare LOS or reflection rays (see Figure 7.2). Since the presented rules have been deduced based on the lifetime of reflection rays, it is not surprising that in geometries dominated by diffraction they must be slightly adapted.

As a result, ***Rule B* seems to be the most promising rule, except in geometries dominated by diffraction** where it is suggested to further reduce the extrapolation time (using *Rule D* for example).

7.1.2.2 System parameters

Spectral divergence Results are presented in Table 7.8. Again, increasing the extrapolation time reduces the mean percentage of simulation time where the spectral divergence is below 0.1, also leading to larger standard deviations and larger variations between the considered bandwidths.

Furthermore, **there is no clue about a general or average rule stating how the extrapolation time can be relaxed depending on the system bandwidth**. This is a consequence of the averaging, over time for a given RT simulation, and over all configurations. Because of this averaging, the distances traveled by the rays and the associated delays between rays are varying, and so does the delay spread. Since it has been shown that the impact on the spectral divergence is greater for bandwidths inversely proportional to the delay spread (Section 5.2.2), variations of this delay spread means that the greatest impacting bandwidth is also varying. Therefore, one should always refer to the particular studied geometry in order to determine the bandwidths for which the spectral divergence is slightly impacted. Only with such a knowledge, the extrapolation time could be slightly increased (if one is only interested on the spectral divergence and disregards the channel metrics). Increasing this time by a factor greater than two is not recommended, as seen in Table 7.8 where going from *Rules D* to *C* or *B* (i.e. multiplying the extrapolation time by 2 to 4) leads to variations of the time percentage up to 10%.

Matrix collinearity Concerning the matrix collinearity and its dependency with the parameters of the antenna arrays, increasing the ratio $\frac{d}{\lambda}$ always reduces the mean percentage of time where the absolute error on the matrix collinearity is below 0.05, while increasing the standard deviation (and so for a given rule, see Table 7.9). **Relaxation on the extrapolation time is thus possible, especially for small $\frac{d}{\lambda}$ ratios**. For example, the ratio $\frac{d}{\lambda} = 0.1$ provides a mean percentage of time nearly always larger than 90% for all extrapolation time rules.

Finally, **following the same rule(s) as for the channel metrics always leads to accurate results for more than 90% of the time, whatever the system parameters used (bandwidth or antenna spacing)**.

t_{ext}	City street		City crossroad		Highway	
	Mean	Std	Mean	Std	Mean	Std
Rule A	100.00	0.00	100.00	0.00	100.00	0.00
Rule B	95.12	3.44	83.02	6.01	92.83	3.75
Rule C	91.79	5.18	70.14	9.16	86.72	6.29
Rule D	-		90.47	3.58	-	

Table 7.3: Percentage of simulation time where relative error on **delay spread** is below 20%, depending on the chosen extrapolation time rule (*all results are in percent*)

t_{ext}	City street		City crossroad		Highway	
	Mean	Std	Mean	Std	Mean	Std
Rule A	100.00	0.00	100.00	0.00	100.00	0.00
Rule B	93.89	5.04	83.45	7.15	91.26	3.63
Rule C	89.62	7.77	73.58	10.66	84.26	6.58
Rule D	-		91.17	3.84	-	

Table 7.4: Percentage of simulation time where relative error on **azimuth spread** is below 20%, depending on the chosen extrapolation time rule (*all results are in percent*)

t_{ext}	City street		City crossroad		Highway	
	Mean	Std	Mean	Std	Mean	Std
Rule A	100.00	0.00	100.00	0.00	100.00	0.00
Rule B	95.51	3.83	88.77	5.47	90.48	6.84
Rule C	91.71	6.40	80.67	8.81	85.11	8.65
Rule D	-		93.80	3.31	-	

Table 7.5: Percentage of simulation time where relative error on **elevation spread** is below 20%, depending on the chosen extrapolation time rule (*all results are in percent*)

t_{ext}	City street		City crossroad		Highway	
	Mean	Std	Mean	Std	Mean	Std
Rule A	100.00	0.00	100.00	0.00	100.00	0.00
Rule B	93.51	6.18	84.05	7.93	91.87	3.51
Rule C	90.17	7.63	75.13	11.49	84.68	6.60
Rule D	-		90.66	4.50	-	

Table 7.6: Percentage of simulation time where relative error on **K-factor** is below 20%, depending on the chosen extrapolation time rule (*all results are in percent*)

t_{ext}	City street		City crossroad		Highway	
	Mean	Std	Mean	Std	Mean	Std
Rule A	100.00	0.00	100.00	0.00	100.00	0.00
Rule B	95.51	2.88	85.47	4.82	92.29	3.05
Rule C	91.72	5.02	76.15	7.48	86.10	5.41
Rule D	-		92.39	3.53	-	

Table 7.7: Percentage of simulation time where relative error on **total received power** is below 20%, depending on the chosen extrapolation time rule (*all results are in percent*)

t_{ext}	Bandwidth	City street		City crossroad		Highway	
		Mean	Std	Mean	Std	Mean	Std
Rule A	any	100.00	0.00	100.00	0.00	100.00	0.00
Rule B	1 MHz	97.02	2.87	86.74	5.30	93.53	2.38
	10 MHz	98.47	1.91	84.37	5.87	94.83	2.46
	100 MHz	97.63	2.35	83.42	6.95	96.44	2.83
	1 GHz	98.95	1.64	88.66	5.66	98.39	2.07
Rule C	1 MHz	94.24	4.97	77.46	6.37	88.73	4.42
	10 MHz	97.13	2.58	71.58	9.99	89.96	5.2
	100 MHz	95.34	3.00	69.00	10.61	93.24	5.01
	1 GHz	97.98	2.55	77.81	9.56	96.57	3.30
Rule D	1 MHz	-		93.12	3.18	-	
	10 MHz			92.02	2.99		
	100 MHz			92.34	2.99		
	1 GHz			95.00	2.80		

Table 7.8: Percentage of simulation time where **spectral divergence** is below 0.1, depending on the chosen extrapolation time rule (*all results are in percent*)

t_{ext}	d/λ	City street		City crossroad		Highway	
		Mean	Std	Mean	Std	Mean	Std
Rule A	any	100.00	0.00	100.00	0.00	100.00	0.00
Rule B	0.1	99.64	0.66	94.37	3.41	96.72	2.12
	0.5	99.16	1.21	89.63	5.37	96.61	1.93
	1	96.09	3.15	89.07	5.76	95.70	2.68
Rule C	0.1	99.06	1.61	89.60	5.90	93.77	3.71
	0.5	97.96	2.57	82.31	7.35	93.83	2.80
	1	92.92	5.42	81.95	9.41	92.74	3.68
Rule D	0.1	-		97.35	1.69	-	
	0.5			94.57	3.58		
	1			94.43	4.15		

Table 7.9: Percentage of simulation time where absolute error on **matrix collinearity** is below 0.05, depending on the chosen extrapolation time rule (*all results are in percent*)

7.1.2.3 Computational gain

For all simulations, the execution times for RT and DRT have been recorded. They were found to vary from one simulation to another, depending on the current load of the shared computer used and the complexity of the geometry.

The geometric computational gain C_G is defined based on observations from Section 6.2. Indeed, the time necessary to compute the electric field of diffracted rays is removed from both RT and DRT execution times (with the hypothesis this is the same) and then their ratio is computed. Therefore, the gain C_G only compares execution times needed to obtain the geometry of the rays, hence its name of “geometric gain”. Table 7.10 gathers the mean and the standard deviation of the geometric computational gain depending on the studied configuration. It can be observed that this gain reaches on average three orders of magnitude and mainly comes from the saving of the computation of the polygons visibility and the reflection tree that is part of the RT. Regarding the *highway* configuration, the gain is even larger owing to the small number of rays. In this case, very few computations are performed by DRT (the number of computations in DRT is proportional to the number of rays), whereas whatever the number of rays, RT needs to construct the reflection tree and evaluate the visibility. Modifying slightly the initial configurations leads to the creation of new rays (e.g. apparition of a LOS), explaining why the standard deviation can be quite large.

	City street		City crossroad		Highway	
	Mean	Std	Mean	Std	Mean	Std
DRT gain	1405	510	1546	439	5401	2044

Table 7.10: Geometric computational gain C_G thanks to DRT

Nevertheless, the real, and effective, computational gain C_R also takes into account the computation time for the RT initialisations as part of the DRT execution time (with or without neglecting the computation time for the diffraction). This gain is expected to increase with the extrapolation time since a longer extrapolation time leads to fewer RT initialisations, reducing the overall time of the DRT simulations. In fact, assuming that the DRT computation time is negligible compared to the RT execution time, an upper bound for the real computational gain (denoted C_R^{th}) is given by:

$$C_R < C_R^{th} = \frac{t_{ext}}{0.01}, \tag{7.1}$$

since RT simulations are performed every 0.01 s in our case and, thanks to DRT, RT initialisations are only needed every t_{ext} seconds. As it can be seen in Table 7.11, the measured C_R is close to the theoretical upper bound if the computation time of diffracted fields is neglected. This is a direct consequence of the geometric computational gain C_G which is so large that it is reasonable to assume that the computation of the rays using DRT at time where no RT initialisation is performed is negligible. Taking into account the total time of DRT (with RT initialisations and diffraction), the theoretical C_R is far from being reached. Therefore, to fully benefit from the DRT computational gain, further improvements or modifications to the diffraction model in the current DRT approach must be carried out.

Finally, the denominator of equation (7.1) is quite arbitrary and is related to the timestep where one wants to obtain simulation results. In other words, if one is interested to have channel knowledge at every 0.001 second instead, then the computed theoretical gain will be 10 times larger. Therefore, one must remember that this gain is always relative, the main quantity that it involves being the extrapolation time t_{ext}.

	City street			City crossroad			Highway	
Th.	Mean	Std	Th.	Mean	Std	Th.	Mean	Std
5	2.25 (4.98)	0.49 (0.01)	5	2.08 (4.98)	0.26 (0.02)	4	2.56 (3.99)	0.34 (0.002)
10	2.97 (9.93)	0.92 (0.03)	10	2.63 (9.93)	0.408 (0.02)	8	3.80 (7.99)	0.72 (0.01)
20	3.56 (19.7)	1.44 (0.11)	20	3.04 (19.72)	0.54 (0.09)	16	5.06 (15.94)	1.23 (0.03)

Table 7.11: Real computational gain C_R *(theoretical value from equation (7.1) - mean and std based on simulation results - results in parenthesis neglect diffraction)*

7.2 Real environment

As a final step, measurements in a real environment have been compared to RT and DRT simulations. These measurements come from a V2V data collection campaign at 5.9 GHz, performed at the University of Southern California (Los Angeles) in 2017 [62]. Based on these, MPCs have been extracted using a high-resolution parameter estimation algorithm presented in [63], and compared to the rays obtained by RT and DRT.

Figure 7.4: *McClintock avenue*, with initial (front) and final (back) positions of receiver represented (Source: *Google Maps*)

The data used in this work are car-to-car data collected in *McClintock avenue*. The geometry is depicted in Figure 7.4, retrieved from *Google Maps*.

Two dimensional views of the constructed geometry model used for RT and DRT are given in Figures 7.5a and 7.5b. Both the transmitter and receiver are moving to the right. Because

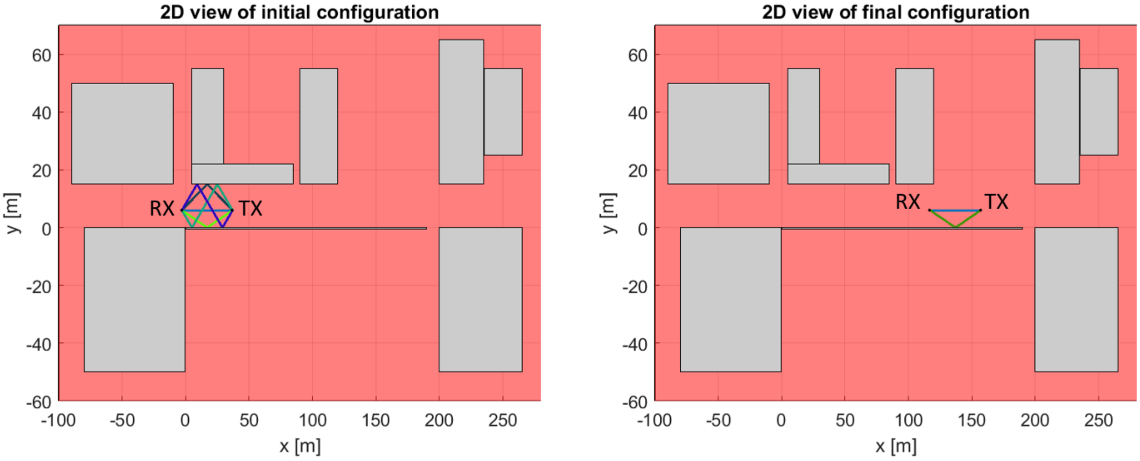

(a) Initial positions of TX-RX

(b) Final positions of TX-RX

Figure 7.5: RT model of the geometry for *McClintock avenue* (only reflection rays are represented)

Carrier frequency	5.9	[GHz]
Effective relative permittivity of bricks	4.44 - j 0.64	[/]
Effective relative permittivity of ground	3 - j 0.052	[/]
Effective relative permittivity of metallic barrier	4.5 - j 1.22×10^8	[/]
Maximal number of interactions	2	[/]

Table 7.12: Simulation parameters for *McClintock avenue*

the real-time positions and velocities of the vehicles have not been accurately recorded during the campaign, focus has only been given to a small part of the data where it has been assumed that both the TX and RX are moving with a constant velocity of 6 m/s, with a constant spacing of 40 meters between them. These estimated parameters have been deduced from the evolution of the measured mean delay τ_m. Indeed, assuming that the main MPC is the LOS, which is the case in a canyon, the mean delay is mostly related to the spacing between the vehicles, and provided this mean delay does not change drastically, the vehicles spacing can be assumed to be constant and computed. Regarding the velocity of both vehicles, it has been recovered based on a video recorded during the measurement campaign, enabling to relate some characteristics of the mean delay (e.g. decrease of the mean delay when both vehicles are close to each other because stopped at a crossroad) with the vehicles positions in the geometry. Knowing the vehicles positions in the geometry and the time of these positions, the velocity can be estimated.

All in all, 20 seconds of measurements' time have been exploited, during which the vehicles are moving in a canyon formed by brick walls on one side (left side of the road in Figure 7.4) and a metallic barrier separating the road and an American football field on the other side (right side of the road in Figure 7.4). The electromagnetic and simulation parameters for the RT and DRT models are grouped in Table 7.12. The effective relative permittivities have been computed based on [48], using linear interpolation to obtain the conductivity values at the considered carrier frequency and assuming a dry ground as well as brick walls with 5% of relative humidity.

7.2.1 Power delay profiles

The evolutions of the power delay profiles simulated and recovered from the measurements are given in Figures 7.6 and 7.7, each dot representing one MPC with a given power, delay and at a given time. In both cases, power has been normalized with the power of the LOS component and the relative intensity is given by the color of the dot. Moreover, in order to retrieve MPCs from RT simulations, rays with similar delay characteristics have been clustered.

In Figure 7.6, depicting the evolution of the power delay profile obtained by RT simulations, one can identify the LOS ray and the reflection rays as being the horizontal lines formed by the dots at the bottom of the figure. Indeed, they have large power and small delays, that are not varying with time since these rays are actually "sliding" with the vehicles along the canyon walls. Therefore, no change in distances traveled by the rays is observed.

On the contrary, oblique lines are related to diffraction rays since they occur on fixed edges that may be located closer to or further from the vehicles depending on their motion. For example, the oblique lines starting at a delay close to 0.2 μs and ending at a delay close to 1 μs can be related to diffraction rays occurring at edges that are located at the beginning of the canyon. Indeed, when the transmitter and receiver are moving away from these edges, the delay of these rays is expected to increase, whereas their power will decrease. With similar considerations, other diffraction rays related to the canyon's end or to buildings in the geometry can be identified.

Thanks to these conclusions, it is possible to interpret the evolution of the power delay profile obtained by extracing the MPCs from the measurements (Figure 7.7). At the bottom, the LOS and some reflections rays can be identified. Moreover, some diffraction rays are also clearly noticeable, especially the ones starting at delays close to 0.4 μs and 1 μs at time 0 second (see oblique lines in Figure 7.7), even though they do not fully agree in terms of delay or power with the diffraction rays identified by RT. This disagreement can have several explanations such as the simplicity of the geometry model used for RT (few buildings, represented by rectangular cuboids), some errors on the electromagnetic parameters used or errors on the positioning of the buildings and vehicles (since this latter has not been recorded). Moreover, ray tracing, being based on GO, only provides an approximation of waves propagation. Nevertheless, even if the agreement is far from perfect in our case, RT really enables to get some insights and explain what can be seen in the measurements.

A last trend observed in the measurements are the several horizontal lines, forming "waves", and spaced by a relatively constant delay. These have not been identified by RT and may therefore be related to multiple reflections in the canyon, that are sliding with the vehicles. Indeed, since the RT approach has been limited to a maximum number of two interactions, higher order reflections could not have been identified. Another possible explanation is to relate them to transmission rays, i.e. rays that have been transmitted inside a building and then reflected back, since this phenomenon is also not modeled in the current RT software.

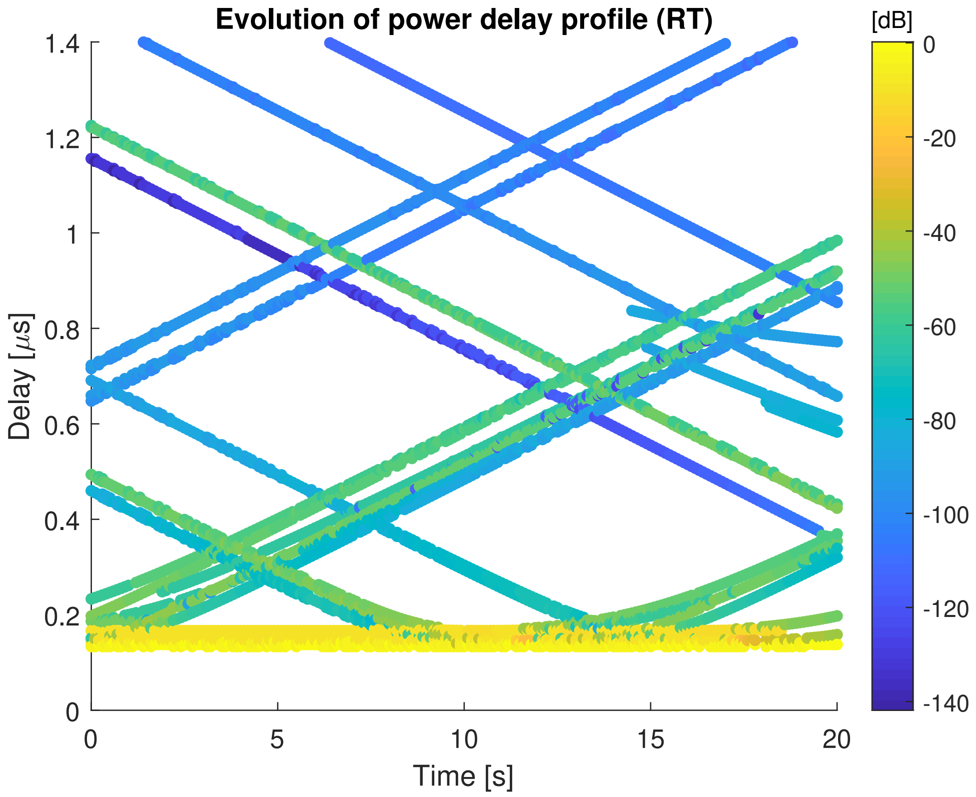

Figure 7.6: Evolution of power delay profile for *McClintock avenue*, based on RT simulations

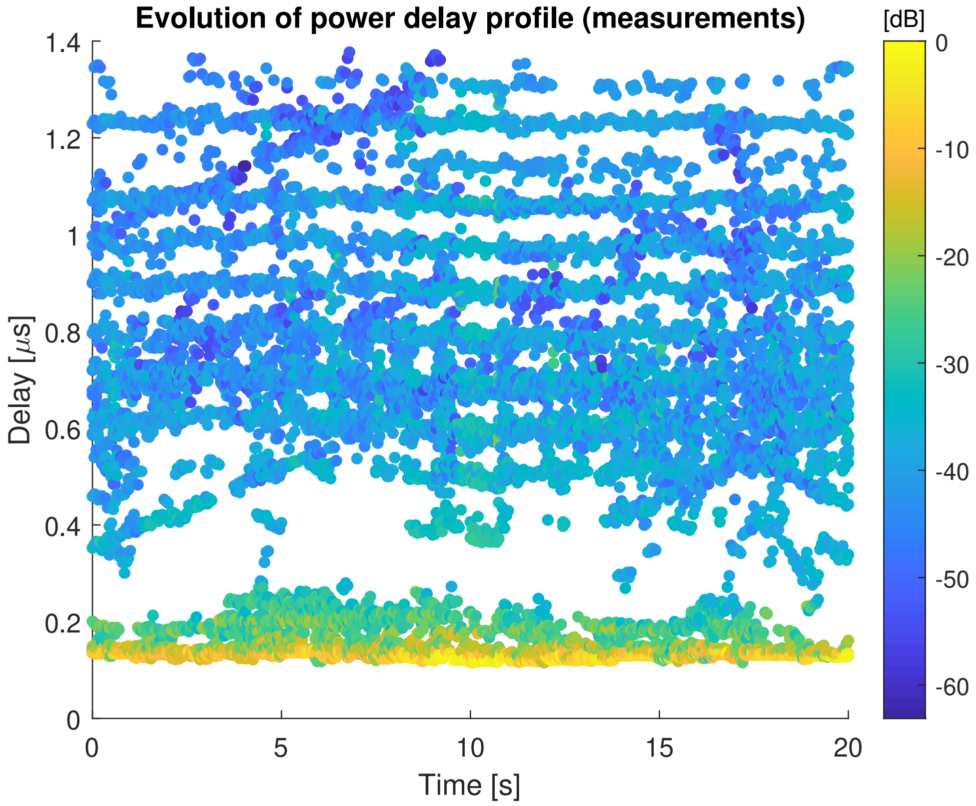

Figure 7.7: Evolution of power delay profile for *McClintock avenue*, based on the measurements and extracted MPCs

However, if these “waves” are multiple reflections or coming from transmission rays, one would expect their relative power to decrease with increasing delays, which is not observed. They may thus be related to artefacts arising from the MPCs extraction from the data.

7.2.2 Delay and angle spreads

The evolution of the mean delay and azimuth angle has been recorded, as well as the evolution of their spread. Measurements and RT or DRT results are given in Figures 7.8 and 7.9. The chosen extrapolation time for DRT is 2.5 seconds, as it corresponds to the time given by $\frac{1}{2}\frac{d_{min}}{v_{max}} = \frac{1}{2}\frac{30}{6} = 2.5$ s, with the 30 meters corresponding to the width of the second building forming the left edge of the canyon in Figure 7.4 (top edge in Figures 7.5a and 7.5b).

Delay The mean delay is on average quite close to 1.4 μs, which is related to the choice of working with constant velocities and a constant spacing between the vehicles. However, measurements show that this assumption is strong, especially at 5 and 10 seconds where mean delay variations are observed, hinting a relative motion between TX and RX. Furthermore, the variation of mean delay in RT and DRT comes from the suppression of some reflection rays, especially shortly before and at the end of the canyon (as expected from the initial and final positions observed in Figures 7.5a and 7.5b). The decrease of the mean delay at the end of the canyon is also observed in the measurements.

Concerning the delay spread, it is underestimated by the RT and DRT simulations. This is a direct consequence of limiting the maximum number of interactions to two in the RT software (for computational time reasons) as well as of the observed “waves” in the measurements.

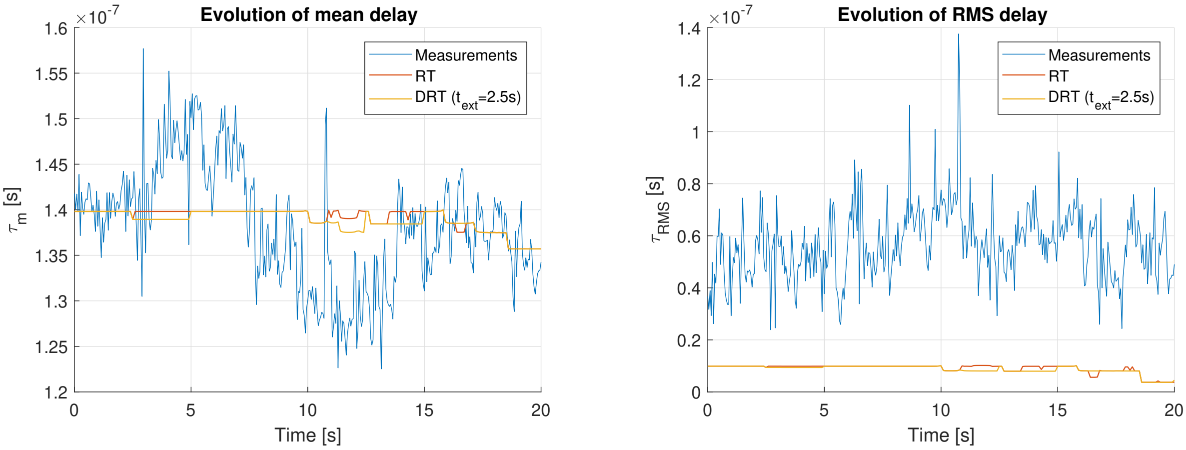

(a) Mean delay

(b) RMS delay spread

Figure 7.8: Evolution of mean delay and RMS delay spread for *McClintock avenue*

Azimuth angle The evolution of the mean azimuth angle (at RX) is given in Figure 7.9. On the one hand, the decrease of the mean angle coming at the end of the canyon is clearly noticeable in the measurements and in RT-DRT simulations. The same holds for the dip observed close to 12 seconds coming from the small gap in the canyon edge (that in reality corresponds to the crossing of a small pedestrian street), even though its impact is larger in the measurements. This may come from errors on the width and the building edges associated with the pedestrian street, which are certainly not as straight as in the RT model of the geometry.

Finally, the azimuth angle spread seems less impacted than the delay spread by the missing rays, owing to the angular symmetry of the canyon. Indeed, rays with multiple reflections come roughly with the same angles for increasing number of interactions, whereas their delays is always increasing.

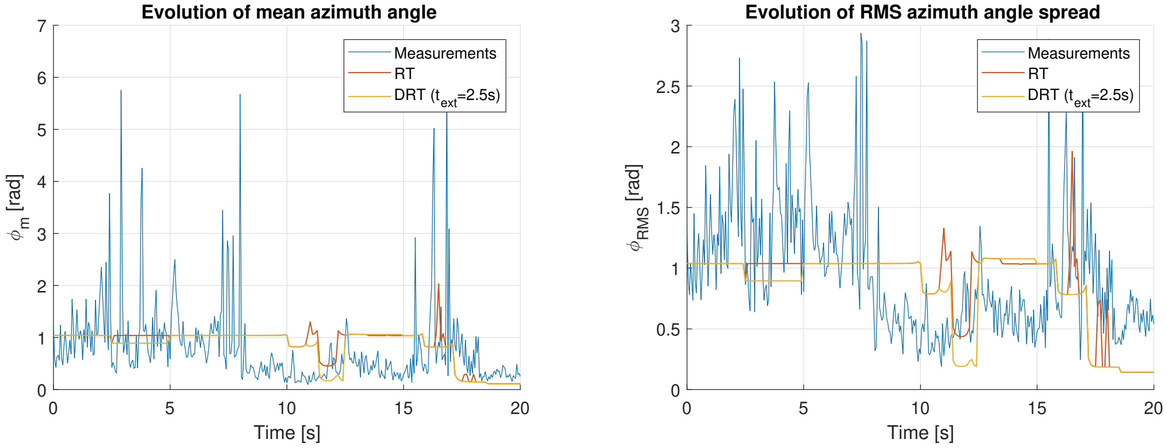

(a) Mean azimuth angle

(b) RMS azimuth angle spread

Figure 7.9: Evolution of mean azimuth angle and RMS azimuth angle spread for *McClintock avenue*

DRT approach Comparing the measurements with the DRT results gives similar conclusions as the ones obtained by comparing with RT simulations. On the one hand, this is because RT and DRT results are close, as also seen in Table 7.13 depicting the percentage of the time where the relative error between RT and DRT is below 20%. On the other hand, differences between measurements and simulations arise mainly from assumptions related to the RT model, which is used in both approaches (RT and DRT).

Table 7.13 also confirms previous results regarding the rule to use in order to get a good extrapolation time, such as 2.5 seconds for this example.

t_{ext}	Delay spread	Azimuth spread	Elevation spread	K-factor	Total received power
0.5 s	95.52 (94.09)	93.03 (93.03)	98.01 (98.01)	100 (100)	100 (100)
1 s	95.02 (94.52)	90.54 (90.54)	100 (100)	100 (100)	100 (100)
2.5 s	94.53 (90.55)	88.56 (88.56)	88.06 (88.06)	100 (100)	100 (100)
5 s	83.08 (78.11)	76.12 (76.12)	100 (100)	100 (100)	93.03 (92.53)

Table 7.13: Percentage of simulation time for *McClintock Avenue* configuration where relative error on **channel metrics** is below 20%, depending on the chosen extrapolation time (*all results are in percent, figures in parenthesis neglect diffraction rays*)

7.2.3 Conclusions from comparison between measurements and RT simulations

Based on this comparison with measurements, the following conclusions have been drawn:

- The results obtained by RT enabled to get physical insight about the MPCs extracted from the measurements and to relate them to the geometry. However, obtaining quantitative agreements between simulations and measurements has been proven to be difficult, especially because of:
    - the simplicity of the model of the geometry (rectangular cuboids only);
    - the estimation of the positions and velocities of the vehicles, that have not been recorded;
    - the limitations of the RT software, such as the maximum number of interactions set to two;
    - the RT approach itself, which is an approximation of wave propagation.
- When comparing with real measurements, performing DRT instead of RT has not been found to impact the comparison, the main differences between measurements and simulations arising from the RT model.
- The hypothesis of constant velocity is a strong assumption. As such, in geometries where velocities are time-varying, performing DRT with numerical integration can be preferred. Alternatively, the extrapolation time used when performing analytical DRT can be limited by the constant velocity assumption and not anymore by the rules $\frac{d_{min}}{v_{max}}$.
- Perfect knowledge of the dynamic evolution of the geometry, on which is based RT at each time iteration and DRT, is not always accessible.

Chapter 8

Conclusion

8.1 Summary of main contributions and results

The major contribution of this master thesis is certainly the new DRT approach, that has been motivated, detailed and validated thanks to comparisons with RT simulations and measurements.

This new approach, presented in Chapter 4, provides deterministic characterizations of communication channels in dynamic environments, relying on the assumption that the geometry and its evolution are known. It is based on an initial RT simulation and on the tracking of the identified reflection and diffraction points, for which fully analytical expressions have been derived. A generalization of the approach to several interactions has been presented. Numerical and analytical implementations are then possible, the latter method (analytic) requiring the assumption of constant velocities. Nevertheless, it offers a geometric accuracy in terms of the positions of the interaction points close to the nanometer, i.e. the tolerance level set in the RT software.

A major parameter of the presented DRT approach is the extrapolation time during which one can ensure similar results with RT simulations performed at every instant. It is related to the lifetime of the main rays in the geometry, namely the LOS and reflection rays. In order to characterize it, comparisons involving channel and system-based metrics have been conducted. Thanks to a statistical study involving 60 RT simulations in typical V2V configurations, some rules defining the extrapolation time beforehand (i.e. only based on the geometry and the knowledge of its evolution) were found. Depending on the system parameters (and some extra knowledge about the delay spread), relaxation of these rules is possible. On the contrary, in highly dynamic environments where the analytical DRT approach is used, stronger constraints on the extrapolation time can also arise from the constant velocity assumption.

Finally, the presented approach offers a computational gain of the rays geometry of three orders of magnitude, that is only depending on the number of rays in the geometry and not on its complexity. However, the overall gain, that involves the recomputation of the electric field quantities based on the known rays geometry, has been found to be strongly limited by the diffraction model used.

8.2 Further research directions

8.2.1 UCLouvain RT and DRT software

To improve the computational gain, the diffraction model can be adapted. However, avoiding the computation of Fresnel integrals is difficult since they are part of the UTD theory. Instead, using approximations of such integrals can be an option. Assuming the diffraction coefficients to remain constant to avoid computing them at each DRT iteration is also a possibility but one should monitor its impact on the results accuracy (as mentioned in Section 2.4). Moreover, further validations of UCLouvain RT software with measurements should also be conducted, especially in environments dominated by diffraction. This could help defining the diffraction model to use and the necessary accuracy.

8.2.2 Dynamic Ray Tracing

The main limitations of the presented DRT approach are listed below, as well as some possible improvements:

- Designed only for reflection and diffraction: however, new RT tools tend to add more propagation phenomena, such as tree diffusion [22, 23], scattering from rough surfaces [1, 28],... Evaluation of how such phenomena could be added in DRT remains to be carried out.
- Diffraction only at last interaction: the generalization to rays involving one diffraction (at any interaction) and multiple reflections has already been discussed in Section 4.1.2.3. However, generalization to multiple diffraction in a same ray remains an open question.
- Ray suppression mechanism: the current ray suppression mechanism only considers the interaction points independently and makes sure these points do not fall out of the surface they were belonging to. Nevertheless, in practice, rays will also disappear if a new body has moved in the path taken by the ray and this is not verified.
- Translation and constant velocities: the assumption of constant velocities during the extrapolation time should be further studied in real scenarios in order to assess its validity. The presented DRT approaches for time-varying velocities can also be applied to more complex scenarios. Finally, the motion of interaction points due to rotating bodies has not been explored.

8.2.3 Beyond the framework of this document

On the one hand, using DRT to perform channel estimation in real-time communications is a promising application, that may start appearing in the coming years and that appeals for more work in the DRT field. In this case, real-time constraints and the available computational power will also influence the smallest achievable extrapolation time.

On the other hand, a perfect knowledge of the environment and its dynamic evolution can be difficult to achieve in practice, namely for the dynamic part. Therefore, adding stochastic models on top of RT or DRT could be a possible approach [34–36], that has not been explored in this work. In order to develop such models, RT studies of real environments will be needed and one could benefit from DRT to speed up or interpolate the results.

Publications

The following paper has been written in the framework of this master thesis and presented at the 12th meeting of the COST action CA15104 (IRACON):

- Florian Quatresooz, Simon Demey and Claude Oestges, "Tracking of Reflection Points for Improved Dynamic Ray Tracing", Technical Document, *12th Meeting of the COST action CA15104 (IRACON)*, January 2020.

Bibliography

[1] Franco Fuschini, Enrico M Vitucci, Marina Barbiroli, Gabriele Falciasecca, and Vittorio Degli-Esposti. Ray tracing propagation modeling for future small-cell and indoor applications: A review of current techniques. *Radio Science*, 50(6):469–485, 2015.

[2] Zhengqing Yun and Magdy F Iskander. Ray tracing for radio propagation modeling: Principles and applications. *IEEE Access*, 3:1089–1100, 2015.

[3] EM Vitucci, J Chen, V Degli-Esposti, JS Lu, HL Bertoni, and X Yin. Analyzing radio scattering caused by various building elements using millimeter-wave scale model measurements and ray tracing. *IEEE Transactions on Antennas and Propagation*, 67(1):665–669, 2018.

[4] Tan Kim Geok, F Hossain, MN Kamaruddin, Noor Ziela Abd Rahman, Sharlene Thiagarajah, Alan Tan Wee Chiat, and CP Liew. A comprehensive review of efficient ray-tracing techniques for wireless communication. *Int. J. Commun. Antenna Propag*, 8:123–136, 2018.

[5] Leyre Azpilicueta, Cesar Vargas-Rosales, and Francisco Falcone. Intelligent vehicle communication: Deterministic propagation prediction in transportation systems. *IEEE Vehicular Technology Magazine*, 11(3):29–37, 2016.

[6] Andrew S Glassner. *An introduction to ray tracing.* Elsevier, 1989.

[7] John W McKown and R Lee Hamilton. Ray tracing as a design tool for radio networks. *IEEE Network*, 5(6):27–30, 1991.

[8] Scott Y Seidel and Theodore S Rappaport. A ray tracing technique to predict path loss and delay spread inside buildings. In *[Conference Record] GLOBECOM'92-Communications for Global Users: IEEE*, pages 649–653. IEEE, 1992.

[9] Yoshihisa Okumura. Field strength and its variability in vhf and uhf land-mobile radio service. *Rev. Electr. Commun. Lab.*, 16:825–873, 1968.

[10] Masaharu Hata. Empirical formula for propagation loss in land mobile radio services. *IEEE transactions on Vehicular Technology*, 29(3):317–325, 1980.

[11] Yvo de Jong Bultitude and Terhi Rautiainen. Ist-4-027756 winner ii d1. 1.2 v1. 2 winner ii channel models. *EBITG, TUI, UOULU, CU/CRC, NOKIA, Tech. Rep., Tech. Rep*, 2007.

[12] Lingfeng Liu, Claude Oestges, Juho Poutanen, Katsuyuki Haneda, Pertti Vainikainen, François Quitin, Fredrik Tufvesson, and Philippe De Doncker. The cost 2100 mimo channel model. *IEEE Wireless Communications*, 19(6):92–99, 2012.

[13] Jakob Thrane, Darko Zibar, and Henrik L Christiansen. Comparison of empirical and ray-tracing models for mobile communication systems at 2.6 ghz. In *2019 IEEE 90th Vehicular Technology Conference (VTC2019-Fall)*, pages 1–5. IEEE, 2019.

[14] Yoann Corre, Romain Charbonnier, Mohammed Zahid Aslam, and Yves Lostanlen. Assessing the performance of a 60-ghz dense small-cell network deployment from ray-based simulations. In *2016 IEEE 21st International Workshop on Computer Aided Modelling and Design of Communication Links and Networks (CAMAD)*, pages 213–218. IEEE, 2016.

[15] Romain Charbonnier, Mohammed Zahid Aslam, Yoann Corre, and Yves Lostanlen. Mixing deterministic and stochastic propagation for assessing mmwave small-cell networks. In *2017 11th European Conference on Antennas and Propagation (EUCAP)*, pages 136–140. IEEE, 2017.

[16] Simon Demey, Philippe De Doncker, and Claude Oestges. A comparison between stochastic geometry and ray-tracing in small cells. 2019.

[17] Chethan Kumar Anjinappa and Ismail Guvenc. Millimeter-wave v2x channels: Propagation statistics, beamforming, and blockage. In *2018 IEEE 88th Vehicular Technology Conference (VTC-Fall)*, pages 1–6. IEEE, 2018.

[18] Guangrong Yue, Daizhong Yu, Hao Qiu, Ke Guan, Lin Yang, and Qifu Lv. Measurements and ray tracing simulations for non-line-of-sight millimeter-wave channels in a confined corridor environment. *IEEE Access*, 7:85066–85081, 2019.

[19] Yoann Corre, Thierry Tenoux, Julien Stéphan, Florian Letourneux, and Yves Lostanlen. Analysis of outdoor propagation and multi-cell coverage from ray-based simulations in sub-6ghz and mmwave bands. In *2016 10th European Conference on Antennas and Propagation (EuCAP)*, pages 1–5. IEEE, 2016.

[20] Alberto Perez, Abdurrahman Fouda, and Ahmed S Ibrahim. Ray tracing analysis for uav-assisted integrated access and backhaul millimeter wave networks. In *2019 IEEE 20th International Symposium on" A World of Wireless, Mobile and Multimedia Networks"(WoWMoM)*, pages 1–5. IEEE, 2019.

[21] EM Vitucci, V Degli-Esposti, F Fuschini, JS Lu, M Barbiroli, JN Wu, M Zoli, JJ Zhu, and HL Bertoni. Ray tracing rf field prediction: An unforgiving validation. *International Journal of Antennas and Propagation*, 2015, 2015.

[22] Nuno R Leonor, Telmo R Fernandes, Manuel García Sánchez, and Rafael FS Caldeirinha. A 3-d model for millimeter-wave propagation through vegetation media using ray-tracing. *IEEE Transactions on Antennas and Propagation*, 67(6):4313–4318, 2019.

[23] Jung-Yong Lee, Jae-Hyun Lee, and Seong-Cheol Kim. Improving the accuracy of millimeter-wave ray-tracing simulations by modeling roadside trees. *IEEE Antennas and Wireless Propagation Letters*, 18(1):162–166, 2018.

[24] Mohammed Zahid Aslam, Yoann Corre, and Yves Lostanlen. Effect of human crowd obstruction on the performance of an urban small-cell millimeter-wave access network. In *2017 IEEE 86th Vehicular Technology Conference (VTC-Fall)*, pages 1–5. IEEE, 2017.

[25] Masahiro Umehira, Shigeki Takeda, Teruyuki Miyajima, and Kenichi Kagoshima. An extended calculation model for shadowing loss caused by a moving human body in 60ghz wlan. In *The 20th Asia-Pacific Conference on Communication (APCC2014)*, pages 113–116. IEEE, 2014.

[26] Ke Guan, Danping He, Bo Ai, David W Matolak, Qi Wang, Zhangdui Zhong, and Thomas Kürner. 5-ghz obstructed vehicle-to-vehicle channel characterization for internet of intelligent vehicles. *IEEE Internet of Things Journal*, 6(1):100–110, 2018.

[27] Francesco Mani. *Improved ray-tracing for advanced radio propagation channel modeling.* PhD thesis, PhD Thesis, ICTEAM, UCL Belgium, 2012.

[28] Minoru Inomata, Tetsuro Imai, Koshiro Kitao, Yukihiko Okumura, Sasaki Motoharu, and Yasushi Takatori. Radio propagation prediction for high frequency bands using hybrid method of ray-tracing and er model with point cloud of urban environments. 2018.

[29] Jörg Nuckelt, Dennis M Rose, Thomas Jansen, and Thomas Kürner. On the use of openstreetmap data for v2x channel modeling in urban scenarios. In *2013 7th European Conference on Antennas and Propagation (EuCAP)*, pages 3984–3988. IEEE, 2013.

[30] Khalid LA El-Ashmawy. Testing the positional accuracy of openstreetmap data for mapping applications. *Geodesy and Cartography*, 42(1):25–30, 2016.

[31] Georgia E Athanasiadou and Andrew R Nix. Investigation into the sensitivity of the power predictions of a microcellular ray tracing propagation model. *IEEE transactions on Vehicular Technology*, 49(4):1140–1151, 2000.

[32] Karim Rizk, J-F Wagen, and Fred Gardiol. Influence of database accuracy on two-dimensional ray-tracing-based predictions in urban microcells. *IEEE transactions on vehicular technology*, 49(2):631–642, 2000.

[33] Quentin Gueuning. *Inhomogeneous plane-wave spectrum based Physical Optics for the simulation of urban radio propagation.* PhD thesis, UCL-Université Catholique de Louvain, 2019.

[34] Jonathan Ledy, Hervé Boeglen, Anne-Marie Poussard, Benoît Hilt, and Rodolphe Vauzelle. A semi-deterministic channel model for vanets simulations. *International Journal of Vehicular Technology*, 2012, 2012.

[35] Li Tian, Vittorio Degli-Esposti, Enrico M Vitucci, and Xuefeng Yin. Semi-deterministic radio channel modeling based on graph theory and ray-tracing. *IEEE Transactions on Antennas and Propagation*, 64(6):2475–2486, 2016.

[36] Aliye Ozge Kaya, Larry J Greenstein, and Wade Trappe. Characterizing indoor wireless channels via ray tracing combined with stochastic modeling. *IEEE Transactions on Wireless Communications*, 8(8):4165–4175, 2009.

[37] Stefan O Wald and Frank Weinmann. Ray tracing for range-doppler simulation of 77 ghz automotive scenarios. In *2019 13th European Conference on Antennas and Propagation (EuCAP)*, pages 1–4. IEEE, 2019.

[38] Mate Boban, Rui Meireles, Joao Barros, Peter Steenkiste, and Ozan K Tonguz. Tvr—tall vehicle relaying in vehicular networks. *IEEE Transactions on Mobile Computing*, 13(5):1118–1131, 2013.

[39] Dimitrios Vlastaras, Taimoor Abbas, Mikael Nilsson, Russ Whiton, Magnus Olbäck, and Fredrik Tufvesson. Impact of a truck as an obstacle on vehicle-to-vehicle communications in rural and highway scenarios. In *2014 IEEE 6th International Symposium on Wireless Vehicular Communications (WiVeC 2014)*, pages 1–6. IEEE, 2014.

[40] Fred Wiffen, Lawrence Sayer, Mohammud Z Bocus, Angela Doufexi, and Andrew Nix. Comparison of otfs and ofdm in ray launched sub-6 ghz and mmwave line-of-sight mobility channels. In *2018 IEEE 29th Annual International Symposium on Personal, Indoor and Mobile Radio Communications (PIMRC)*, pages 73–79. IEEE, 2018.

[41] D. Bilibashi, E. M. Vitucci, and V. Degli-Esposti. Dynamic ray tracing: Introduction and concept. In *2020 14th European Conference on Antennas and Propagation (EuCAP)*, 2020.

[42] William C Jakes and Donald C Cox. *Microwave mobile communications*. Wiley-IEEE Press, 1994.

[43] Rubén Ibernón-Fernández, J-M Molina-Garcia-Pardo, J-V Rodriguez, and Leandro Juan-Llacer. Predicting coverage in an area from a single simulation. In *2005 IEEE Antennas and Propagation Society International Symposium*, volume 1, pages 727–730. IEEE, 2005.

[44] Juan Pascual-García, José-María Molina-Garcia-Pardo, María-Teresa Martínez-Inglés, José-Víctor Rodríguez, and Leandro Juan-Llácer. Fast and accurate electric field estimation from a single ray tracing simulation. *Applied Computational Electromagnetics Society Journal*, 30(6), 2015.

[45] Constantine A Balanis. *Advanced engineering electromagnetics*. John Wiley & Sons, 1999.

[46] DA McNamara, CWI Pistorius, and JAG Malherbe. The uniform geometrical theory of diffraction. *Artech House, London*, 1990.

[47] ALLENK Dominek, LEON Peters, and W Burnside. An additional physical interpretation in the luneburg-kline expansion. *IEEE transactions on antennas and propagation*, 35(4):406–411, 1987.

[48] Claude Oestges. *Propagation Modelling of Low Earth-Orbit Satellite Personal Communication Systems*. PhD thesis, PhD Thesis,UCL Belgium, 2000.

[49] J Keller. One hundred years of diffraction theory. *IEEE Transactions on Antennas and Propagation*, 33(2):123–126, 1985.

[50] Joseph B Keller. Geometrical theory of diffraction. *Josa*, 52(2):116–130, 1962.

[51] Robert G Kouyoumjian and Prabhakar H Pathak. A uniform geometrical theory of diffraction for an edge in a perfectly conducting surface. *Proceedings of the IEEE*, 62(11):1448–1461, 1974.

[52] R Luebbers. Finite conductivity uniform gtd versus knife edge diffraction in prediction of propagation path loss. *IEEE Transactions on Antennas and Propagation*, 32(1):70–76, 1984.

[53] Diego Tami, Cássio G Rego, Dinael Guevara, Andrés Navarro, Fernando JS Moreira, Jordi Giménez, and Hernan G Triana. Analysis of heuristic uniform theory of diffraction coefficients for electromagnetic scattering prediction. *International Journal of Antennas and Propagation*, 2018, 2018.

[54] Duncan Marsh. *Applied geometry for computer graphics and CAD.* Springer, 2006.

[55] F Saez De Adana, O Gutierrez Blanco, I Gonzalez Diego, J Perez Arriaga, and Manuel F Cátedra. Propagation model based on ray tracing for the design of personal communication systems in indoor environments. *IEEE transactions on vehicular technology*, 49(6):2105–2112, 2000.

[56] John Daniel Kraus and Ronald J Marhefka. *Antennas for all applications.* 2002.

[57] Dong Yan, Ke Guan, Danping He, Bo Ai, Zan Li, Junhyeong Kim, Heesang Chung, and Zhangdui Zhong. Channel characterization for vehicle-to-infrastructure communications in millimeter-wave band. *IEEE Access*, 8:42325–42341, 2020.

[58] David J Galas, Gregory Dewey, James Kunert-Graf, and Nikita A Sakhanenko. Expansion of the kullback-leibler divergence, and a new class of information metrics. *Axioms*, 6(2):8, 2017.

[59] Tryphon T Georgiou. Distances between power spectral densities. *arXiv preprint math/0607026*, 2006.

[60] Bruno Clerckx and Claude Oestges. *MIMO wireless networks: channels, techniques and standards for multi-antenna, multi-user and multi-cell systems.* Academic Press, 2013.

[61] G Ohman. The pseudo-brewster angle. *IEEE Transactions on Antennas and Propagation*, 25(6):903–904, 1977.

[62] Rui Wang, C Umit Bas, Olivier Renaudin, Seun Sangodoyin, Usman T Virk, and Andreas F Molisch. A real-time mimo channel sounder for vehicle-to-vehicle propagation channel at 5.9 ghz. In *2017 IEEE International Conference on Communications (ICC)*, pages 1–6. IEEE, 2017.

[63] Rui Wang, Olivier Renaudin, C Umit Bas, Seun Sangodoyin, and Andreas F Molisch. High-resolution parameter estimation for time-varying double directional v2v channel. *IEEE Transactions on Wireless Communications*, 16(11):7264–7275, 2017.

UNIVERSITÉ CATHOLIQUE DE LOUVAIN
École polytechnique de Louvain
Rue Archimède, 1 bte L6.11.01, 1348 Louvain-la-Neuve, Belgique | **www.uclouvain.be/epl**